Winter 2023

Modeling 21st Century Peak Flows in the Nooksack River Basin in Northwestern Washington State Using Dynamically-Downscaled Global Climate Model Projections

Evan A. Paul
Western Washington University, evan-paul@outlook.com

Modeling 21st Century Peak Flows in the Nooksack River Basin in Northwestern Washington State Using Dynamically-Downscaled Global Climate Model Projections

By

Evan A. Paul

Accepted in Partial Completion
of the Requirements for the Degree
Master of Science

ADVISORY COMMITTEE

Dr. Robert J. Mitchell, Chair

Dr. Allison M. Pfeiffer

Ryan D. Murphy, M.S.

GRADUATE SCHOOL

David L. Patrick, Dean

Master's Thesis

In presenting this thesis in partial fulfillment of the requirements for a master's degree at Western Washington University, I grant to Western Washington University the non-exclusive royalty-free right to archive, reproduce, distribute, and display the thesis in any and all forms, including electronic format, via any digital library mechanisms maintained by WWU.

I represent and warrant this is my original work, and does not infringe or violate any rights of others. I warrant that I have obtained written permissions from the owner of any third party copyrighted material included in these files.

I acknowledge that I retain ownership rights to the copyright of this work, including but not limited to the right to use all or part of this work in future works, such as articles or books.

Library users are granted permission for individual, research and non-commercial reproduction of this work for educational purposes only. Any further digital posting of this document requires specific permission from the author.

Any copying or publication of this thesis for commercial purposes, or for financial gain, is not allowed without my written permission.

Evan A. Paul

March 2023

Modeling 21st Century Peak Flows in the Nooksack River Basin in Northwestern Washington State Using Dynamically-Downscaled Global Climate Model Projections

A Thesis
Presented to
The Faculty of
Western Washington University

In Partial Fulfillment
Of the Requirements for the Degree
Master of Science

By
Evan A. Paul
March 2023

Abstract

The Nooksack River in northwest Washington State provides freshwater for agriculture, municipal, and industrial use and serves as a vital habitat for endangered salmon, a resource that is of cultural and economic importance to the Nooksack Indian Tribe and the surrounding region. Due to the complex topography in the basin and the mild maritime climate of the Puget Sound region, streamflow in the Nooksack River is highly sensitive to fluctuations in air temperature. Global climate models (GCMs) project an increase in air temperatures for the Puget Sound region, and previous modeling within the Nooksack basin projects a reduction in snowpack extent through the 21st century and an increase in winter streamflow magnitude. As more landscape becomes exposed to rain rather than snow and heavy winter precipitation events intensify, peak flows and sediment delivery to streams will likely increase due to rapid runoff, resulting in salmon habitat degradation and increased flood risk. Thus, anticipating the effect of climate change on peak flows is crucial for salmon habitat restoration efforts and flood mitigation planning. To quantify the timing and magnitude of future peak flows, I use a calibrated Distributed Hydrology Soil Vegetation Model (DHSVM) and meteorological forcings from an ensemble of high-emission GCMs dynamically-downscaled using the Weather Research and Forecasting (WRF) model.

Due to the variability of climate scenarios depicted by GCMs, a range of streamflow and snowpack magnitude changes in the Nooksack River basin are projected by the hydrology simulations. By the end of the 21st century, results indicate a decrease in annual peak snow-water equivalent (-72% to -82%), a shift in the timing of peak snow-water equivalent to approximately one month earlier, an increase in winter flows (+31% to +56%), a decrease in summer flows (-37% to -72%), and the disappearance of the snowmelt derived spring peak in the hydrograph as the basin transitions from transient to rain-dominant. These results are consistent with previous modeling in the Nooksack River basin and other regional climate change studies in the Pacific Northwest and Puget Sound region. Due to more precipitation falling as rain rather than snow and heavy rain events becoming more frequent and intense, future peak flows are projected to increase in magnitude by 34-60% across all flow durations and return periods that were analyzed, with the largest changes occurring in the high relief subbasins. The frequency of high magnitude, flood-inducing peak flows will also increase into the future, lengthening the flood season by approximately three months.

Acknowledgments

Funding for this project was provided by the Nooksack Indian Tribe and the Bureau of Indian Affairs Branch of Tribal Climate Resilience. Additional funding was provided through the Geological Society of America Graduate Student Research Grant and the Western Washington University Geology Department. Regional climate model simulations were provided by Ruby Leung at the Pacific Northwest National Laboratory and Cliff Mass at the University of Washington Department of Atmospheric Sciences.

First and foremost, I want to thank my advisor Dr. Robert Mitchell for his unparalleled support throughout this project. His teaching and guidance has allowed me to become the scientist I am today, which will be invaluable throughout my career. Thank you to my committee members, Dr. Allison Pfeiffer and Ryan Murphy, for their insight and feedback throughout the developmental and writing stages of this project. Thank you to Dr. Guillaume Mauger and Jason Won at the University of Washington Climate Impacts Group for providing their expertise on climate model downscaling and bias-correcting. Thank you to Oliver Grah and Jezra Beaulieu at the Water Resources Program of the Nooksack Indian Tribe for their long-term support of our lab's research within the Nooksack River basin. Thank you to the numerous former graduate students who contributed thousands of hours to improving and refining the methods used in this project, particularly James Robinson, who provided modeling insight and data analysis scripts that expedited the timeline of this project. Lastly, I want to thank my parents Amy and Clare, my sisters Amanda and Natalie, and my fiancé Steph for their unconditional support over the last few years.

Table of Contents

List of Tables

List of Figures

1.0 Introduction

The Nooksack River basin is a transient rain-snow basin in the North Cascades that drains into the Salish Sea (Figure 1) and provides fresh water to regional municipalities, tribes, agriculture, and industry and serves as a vital habitat to endangered salmon. Historically, streamflow in the basin is supplied by precipitation and snowmelt in the fall and winter months and snowmelt and glacier melt in the spring and summer months. Transient rain-snow basins in the Puget Sound region are particularly sensitive to changes in air temperature because slight shifts in temperature can determine whether precipitation falls as rain or snow at higher elevations (Hamlet et al., 2013; Mauger et al., 2015). Therefore, there is a growing concern regarding the impacts of climate change on streamflow and what the implications are for flooding and salmon habitat within the Nooksack River (Grah and Beaulieu, 2013). Previous hydrology modeling studies within the Nooksack basin have found that future winter streamflow will increase and snowpack will decrease as a result of projected climate change (Dickerson-Lange and Mitchell, 2013; Murphy, 2016). These changes to streamflow and snowpack will also affect the magnitude and frequency of peak flows in the Nooksack River and potential delivery of sediment to streams (Knapp, 2018).

Global climate models (GCMs; also known as general circulation models) under a high emissions scenario (i.e., Representative Concentration Pathway 8.5) project that the average annual air temperature in the western Cascades region will increase by 4.2°C near the end of the 21st century (Rogers and Mauger, 2021). As a result, more precipitation will fall as rain rather than snow, increasing the potential for rapid runoff as more steep landscape becomes exposed due to a declining snowpack (Mauger et al., 2015; Mote et al., 2018). Additionally, heavy rain events, such as atmospheric rivers, are projected to become more frequent and about 22% more intense by the end of the century (Warner et al., 2015). Studies in other western Washington watersheds have shown that the magnitude and frequency of peak flows will increase through the 21st century as a result of the projected changes to precipitation patterns and snowpack extent (Mauger and Won, 2020; Mauger et al., 2021; Robinson, 2022). Previous hydrology modeling in the Nooksack River basin under-simulated peak flows because the meteorological forcings used in the modeling were disaggregated from daily data, thus muting the intensity of heavy, short duration precipitation events that result in peak flows (Dickerson-Lange and Mitchell, 2013; Murphy, 2016).

The objective of this study is to assess how projected climate change will change peak flow magnitude and frequency in the upper Nooksack River basin. I use the Distributed Hydrology Soil Vegetation Model (DHSVM; Wigmosta et al., 1994, 2002) and an ensemble of projected climate data dynamically-downscaled using the Weather Research and Forecasting (WRF; Skamarock et al., 2005) model to simulate future hydrology within the upper Nooksack basin. By using dynamically-downscaled climate data with a one-hour time step, the storm events that cause peak flows are better resolved, thus allowing for an accurate analysis of how future peak flow magnitude and frequency will change through time. By understanding how projected climate change will impact future peak flows, scientists and stormwater managers will be able to make evidence-based decisions regarding future salmon habitat restoration and flood risk management in the basin.

2.0 Background

2.1 Physical Characteristics of the Nooksack River Basin

The Nooksack River basin is located primarily in Whatcom County in northwest Washington State and ranges in elevation from sea level to the peak of Mt. Baker at approximately 3280 meters (also referred to by the indigenous name of Koma Kulshan; Figure 1). Located east of Deming, WA, the upper Nooksack basin encompasses an area of approximately 1555 km^2 and is comprised of three main subbasins: the North, Middle, and South Forks. Each of the subbasins differ both in relief and the proportion of basin area in different elevation ranges (Table 1; Figure 2). The North and Middle Fork subbasins have high relief, ranging from approximately 87 meters (m) near their mouths to 3280 m at the peak of Mt. Baker. The South Fork basin has a lower relief, ranging from 66 to 2120 m at the peak of the South Twin Sister mountain. The three subbasins each converge into the main stem of the Nooksack River near Deming, WA (Figure 1).

The Puget Sound region experiences a maritime climate. In the winter, a low-pressure system, named the Aleutian Low, brings cool, moist air to the region from the north, resulting in cool, wet winters (Moore et al., 2008). In the summer, the Aleutian Low retreats to the north towards the Aleutian Islands of Alaska, resulting in dry, warm summers in the Puget Sound region. Additionally, climate in the region is influenced by annual and decadal climatic events such as the El Niño Southern Oscillation (ENSO) and Pacific Decadal Oscillation (PDO; Moore

et al., 2008). El Niño events typically bring warmer temperatures to the region due to warmer ocean temperatures in the Pacific, while La Niña events produce cooler temperatures. PDO events, which last on the order of decades, bring warmer temperatures to the region during positive oscillations and cooler temperatures during negative oscillations.

Due to the maritime climate and topographic relief of the North Cascades region, precipitation within the Nooksack basin is highly variable and sensitive to small changes in temperature. The North and Middle Forks are classified as snow-dominated basins because they receive more than 40% of their winter precipitation as snow, while the South Fork is classified as a transient rain-snow basin because approximately 10-40% of its winter precipitation falls as snow due to its relatively low relief compared to the North and Middle Forks (Figure 3; Dickerson-Lange and Mitchell, 2013; Hamlet et al., 2013). Most of the precipitation within the basin occurs from October-March and ranges from less than 1 meter/year in the lowlands to more than 4 meters/year in the mountains based on the 30-year (1981-2020) average of annual precipitation (PRISM Climate Group, 2020). Historically, at elevations above 2000 m, annual snow accumulation ranges from 8 to 10 m (Bach, 2002).

2.2 Climate Change in the Puget Sound Region

Average annual air temperature in the Puget Sound region has increased by approximately 0.7°C from 1895 to 2014 (Mote and Salathé, 2010; Abatzoglou et al., 2014; Mauger et al., 2015). During that same time span, spring (March through May) precipitation has increased by 27%, while the other seasons showed no statistically significant evidence that precipitation trends have changed (Mauger et al., 2015). Additionally, the frequency of heavy precipitation events has increased from 1950 to 2009, while few studies show statistically significant results that the intensity of heavy precipitation has increased during that same time period (Madsen and Figdor, 2007; Mass et al., 2011; Mauger et al., 2015).

Various studies have assessed future trends of temperature and precipitation in the Puget Sound region through the use of GCMs (e.g., Mote and Salathé, 2010; Rupp et al., 2017). Relative to the average from the years 1950-1999, annual air temperature is projected to increase by 1.3°C to 3.9°C by the 2050s (30-year average from 2040-2069) and 2.3°C to 5.9°C by the 2080s (30-year average from 2070-2099) based on an ensemble of GCMs under the high emissions scenario Representative Concentration Pathway 8.5 (RCP 8.5; Van Vuuren et al.,

2011; Rogers and Mauger, 2021). Precipitation is more difficult to project due to the complex topography of western Washington. Projections indicate that average precipitation magnitude will increase (10%) in the winter months and decrease (-16%) in the summer months by the 2080s based on RCP 8.5 (Rogers and Mauger, 2021). Additionally, the frequency and intensity of heavy precipitation events (e.g., atmospheric rivers) are projected to increase through the 21st century (Warner et al., 2015). Based on the RCP 8.5 scenario, the heaviest 24-hour precipitation events (i.e., the 99th percentile of annual 24-hour precipitation) will intensify by 22% and increase in frequency to 7-days per year by the 2080s compared to the historical 30-year average (1970-1999) occurrence of 2-days per year (Mauger et al., 2015).

Studies within the region have concluded that as temperatures increase through the 21st century, transient rain-snow basins will become rain-dominant due to more precipitation falling as rain rather than snow (Hamlet et al., 2013; Tohver et al., 2014; Mauger et al., 2015; Murphy, 2016). The hydrograph of a transient rain-snow basin is projected to shift from a two-peak hydrograph (i.e., a winter peak and spring peak) to a single-peak hydrograph due to a decrease in snowpack and earlier spring snowmelt (Mauger et al., 2015). These findings imply that climate change will affect streamflow within the transient upper Nooksack basin (Dickerson-Lange and Mitchell, 2013; Murphy, 2016).

2.3 Hydrology of the Nooksack River Basin

The timing and magnitude of streamflow in the Nooksack River is heavily influenced by temperature and precipitation. These factors control the amount of precipitation that falls as rain or snow, the extent of the snowpack, and the timing and rate of snowmelt in the basin. Historically, rainfall and rain-on-snow events are the largest contributors to streamflow in the Nooksack River during the fall and winter months, while snowmelt and glacial melt are the largest contributors during the spring and summer months (Dickerson-Lange and Mitchell, 2013; Grah and Beaulieu, 2013; Murphy, 2016).

Many studies have concluded that projected changes of temperature and precipitation in the Puget Sound region will affect streamflow in regional watersheds throughout the 21st century (Elsner et al., 2010; Hamlet et al., 2013; Tohver et al., 2014; Mauger et al., 2015; Vano et al., 2015; Truitt, 2018; Clarke, 2020; Robinson, 2022). Increasing temperatures and more precipitation falling as rain rather than snow will decrease basin snowpack and cause glaciers to

recede (Mauger et al., 2015; Frans et al., 2018; Mote et al., 2018). As a result, spring and summer streamflow will decrease. A greater proportion of precipitation falling as rain will increase streamflow in the winter months. Previous hydrology modeling within the upper Nooksack basin has shown similar results in snowpack, glacier, and streamflow changes (Dickerson-Lange and Mitchell, 2013; Murphy, 2016).

As winter streamflow increases due to changes of temperature and precipitation, the magnitude of peak flows will likely increase. Peak flows are high magnitude streamflow events that occur after heavy rainfall and usually last for hours or days depending on the duration of rainfall, the size of the source area, and rain-on-snow timing (Ryberg et al., 2017). Studies within the Puget Sound region suggest that future peak flows will increase in magnitude and frequency (Dickerson-Lange and Mitchell, 2013; Salathé et al., 2014; Lee et al., 2018; Mauger and Won, 2020; Mauger et al., 2021). Peak flow magnitudes are projected to increase through two primary mechanisms: more intense heavy rain events and a decreased snowpack caused by more precipitation falling as rain rather than snow at higher elevations. As mentioned earlier, heavy rain events, such as atmospheric rivers, are projected to increase in frequency and magnitude through the 21st century (Warner et al., 2015). A reduced snowpack will increase the overall area that is available for rapid runoff, thus transporting water to rivers and streams more quickly (Lee et al., 2018). In the higher elevations of a basin (1000-2500 m), where a thicker snowpack exists, rain-on-snow events will likely increase in frequency and intensity due to a transition in precipitation from snow to rain and more intense rainfall (Musselman et al., 2018). With these mechanisms acting together, peak flows in the Nooksack River will likely increase in frequency and magnitude. Paired with rising sea levels, increased sediment delivery to rivers via mass-wasting events, and more frequent wildfires, flood risk in the lowlands of the Nooksack basin will increase drastically (Mauger et al., 2015; Knapp, 2018; Touma et al., 2022).

2.4 Peak Flow Hazards

Possible increases to future peak flows are of concern to those who rely on the salmon that inhabit the Nooksack River, particularly the Nooksack Indian Tribe and the Lummi Nation. Salmon runs in the Nooksack River have declined by 92-98% since the late 1800s, mainly due to habitat degradation (Grah and Beaulieu, 2013). Peak flows can degrade salmon habitat through redd scour, stream sedimentation, and stream network alteration which can strand juveniles by

disconnecting side channels (Goode et al., 2013; Grah and Beaulieu, 2013). Additionally, peak flows can increase the mortality rate of rearing juveniles due to a lack of flood refugia (e.g., natural log jams; Beechie et al., 2013).

In addition to degrading salmon habitat, peak flows can also cause flooding to occur in the lowlands of the Nooksack basin if the water exceeds the banks of the river. From 2005 to 2020, the average discharge of the Nooksack River recorded at the North Cedarville USGS stream gauge (downstream of Deming in Figure 1) was approximately 104 cubic meters per second (cms), but heavy rainfall events, such as atmospheric rivers, can increase discharge by an order of magnitude (e.g., 1594 cms in November 2007; 1436 cms in January 2009; USGS, 2021). Flooding of the Nooksack River in the lowlands can lead to the destruction of property, such as crops and residential homes, the destruction of roads due to culvert failure, the degradation of salmon habitat restoration efforts (e.g., destroying engineered log jams), and in severe cases, lead to loss of life (Gillespie et al., 2014; Mauger et al., 2015; Han and Sharif, 2021). In November of 2021, the Nooksack River reached an estimated peak discharge of 1846 cms at the North Cedarville gauge, the highest discharge in the past 30 years. Downstream flooding resulted in an estimated $50 million in damages to public infrastructure, businesses, and private property within Whatcom County (Whatcom County, 2021).

Flooding of the Nooksack River also affects communities that are located outside of the topographic confines of the Nooksack basin. During the November 2021 flooding events, high flows exceeded the height of (i.e., overtopped) the north bank of the Nooksack River at Everson (Figure 1), resulting in substantial flooding of Everson, Sumas, and the Sumas Prairie in British Columbia. From 1945-2017, overtopping of the banks near Everson has been observed 13 times when streamflow measured at North Cedarville and estimated at Deming exceeds 850 cms (Floodplain Integrated Planning, 2019). Increases to future peak flow magnitudes, paired with aging infrastructure (e.g., roadways and culverts) that is not designed to withstand more intense flooding, will exacerbate the damaging and costly effects of flooding, both within and around the Nooksack River basin.

2.5 Hydrology Modeling

Hydrologic numerical models provide a way to assess future hydrologic conditions for water resource and stormwater management purposes. The DHSVM was co-developed by

researchers at the University of Washington and the Pacific Northwest National Laboratory (PNNL; Wigmosta et al., 1994). The DHSVM is a physically based, spatially distributed model that uses physical and empirical relationships to solve energy and mass balance equations at each grid cell to simulate basin hydrological response variables such as snow accumulation and melt, evapotranspiration, soil storage, and streamflow. It has been used extensively throughout Washington State to quantify the effects of climate and landcover change on hydrology (Elsner et al., 2010; Dickerson-Lange and Mitchell, 2013; Du et al., 2014; Frans et al., 2018; Lee et al., 2018; Sun et al., 2018; Freeman, 2019; Clarke, 2020; Mauger et al., 2021).

Previous hydrology modeling studies in the Nooksack basin have assessed the impacts of climate change on streamflow and snowpack (Dickerson-Lange and Mitchell, 2013), glaciers (Murphy, 2016), mass-wasting susceptibility (Knapp, 2018), and stream temperature (Truitt, 2018), but were unable to capture the effect of heavy rainfall events on peak flows due to the coarse temporal resolution of the climate data used to force the model (i.e., daily data disaggregated into 3-hour timesteps). Additionally, these studies used statistically-downscaled climate data (e.g., Abatzoglou and Brown, 2012; Livneh et al., 2013, 2015), which assume that the statistical relationships used to transform GCMs will stay consistent with climate change, though this may not be the case for extreme climate change (e.g., RCP 8.5; Fowler et al., 2007; Salathe et al., 2007). Recent research has stressed the importance of using dynamically-downscaled climate data from regional climate models in order to better quantify changes in extreme precipitation because dynamical downscaling uses physical principles and relationships (e.g., laws of thermodynamics and fluid mechanics) that are expected to hold true under climate change (Salathé et al., 2014). Additionally, the finer temporal resolution of climate data (i.e., hourly as opposed to daily) from regional climate models better resolve the atmospheric processes, such as atmospheric rivers, that are responsible for producing high magnitude peak flows. Lastly, the spatial variability of weather in complex terrain, such as the Nooksack basin, is better represented by regional climate models (Salathé et al., 2014).

3.0 Methods

3.1 Model Setup

To avoid agricultural and urban complexities (e.g., tile drains and impervious surface runoff) in the lowlands of the Nooksack River basin and the challenge of major overflows at

Everson, I focus on the upper portion of the Nooksack basin culminating at the North Cedarville USGS stream gauge west of Deming, WA (Figure 1). The subbasins within the upper Nooksack basin are modeled separately due to differences in their watershed classifications (Figure 3), which are characterized by the proportion of annual precipitation falling as rain or snow. The DHSVM requires digital grids that represent the spatial variability of topography, landcover, and soil characteristics within a basin. These spatial inputs include elevation, a watershed boundary, landcover, soil type and thickness, and a stream network. The grids were generated at a 150-meter resolution using publicly available digital data, spatial analyst tools within ArcGIS Pro, and Python scripts. The DHSVM version 3.2 is used for this study (Sun et al., 2018).

Digital elevation models (DEMs) for a large portion of Washington State were created from light detection and ranging (LiDAR) data, and were compiled and made accessible by the Washington Department of Natural Resources (WA DNR, 2017). The DEMs of the Nooksack basin have a 1-meter resolution that were mosaiced and resampled to a 150-meter resolution using tools within ArcGIS Pro. The watershed boundaries for each subbasin were defined using the mosaiced and resampled DEMs, ArcGIS Pro hydrology tools, and pourpoints that depict the grid cells to which the individual basins drain.

Soil type data are from the State Soil Geographic (STATSGO) database, which was produced for land management and planning purposes by a combination of agencies collectively known as the National Cooperative Soil Survey (USDA, 1998). The data were converted from vector to raster form at a 150-meter resolution and reclassified into seven DHSVM soil classes (Figure 4). These classes broadly consist of silt, bedrock, and loam, with the latter classifying the majority of the Nooksack basin. The DHSVM is run with three soil layers to simulate subsurface flow. Within the configuration file, soil parameters, such as porosity, field capacity, and vertical hydraulic conductivity, can be defined for each soil layer in each of the soil classes.

Landcover data is from the 2016 National Oceanic and Atmospheric Administration Coastal Change Analysis Program (NOAA C-CAP) gridded dataset which uses spectral reflectance data from Landsat imagery to classify different landcover types (NOAA, 2016). The native 30-meter gridded data were resampled and reclassified into ten DHSVM landcover and vegetation classes (Figure 5). The majority of landcover in the upper Nooksack basin is characterized by evergreen forest (65%) with less abundant deciduous forests, mixed forests, and shrubland (20%). The DHSVM configuration file allows for a monthly adjustment of select

vegetation parameters, such as leaf-area index and radiation attenuation, since some vegetation loses leaf coverage in the fall and winter. In the high elevations of the basin, barren land, snow, and ice make up the landcover (7%).

The soil thickness grid and stream network were generated through a Python script that was developed by researchers at the PNNL (Figures 6 and 7). The script requires a DEM and watershed boundary grid as inputs and uses ArcGIS hydrology tools to generate a soil thickness grid and stream network as a function of elevation, slope, and drainage area. Within a user-defined soil thickness range (between 1 and 5 meters for the Nooksack basin), the script essentially produces thick soils on gentle slopes and valley floors and thin soils on steep slopes and peaks. I used a minimum drainage area of 500,000 m^2 because it provided enough area to capture streams in smaller catchments and at high elevations without producing abundant broken stream segments. Stream segments within the network were assigned channel geometries (i.e., width and depth) and Manning's roughness coefficients based on stream segment slope and drainage area. A total of 36 stream channel classes (i.e., 36 different combinations of segment slope and drainage area producing 36 stream channel classes with unique channel geometries and roughness coefficients) were identified based on satellite imagery (Robinson, 2022).

3.2 Climate Data

The meteorological inputs (forcings) required by the DHSVM are temperature (°C), relative humidity (%), precipitation (m), wind speed (m/s), and incoming solar and longwave radiation (W/m^2) at a defined timestep. I use two sets of dynamically-downscaled gridded climate data: 1) an observationally-based historical dataset for model calibration, and 2) datasets derived from GCMs for projected simulations. Both datasets were dynamically-downscaled to a watershed-scale resolution using the regional Weather Research and Forecasting (WRF) model.

3.2.1 Historical Climate Dataset

Due to the lack of long-term historical meteorological data in the Nooksack basin, I used a gridded dataset of simulated historical meteorological forcings to calibrate the DHSVM. The historical dataset was created by researchers at the PNNL using the WRF model version 3.2 (Chen et al., 2018). The WRF model uses physical and empirical relationships to simulate regional atmospheric processes at a user-defined time step and a fine spatial resolution in order

to capture the orographic effects, land-water contrasts, and mesoscale circulations that characterize the Puget Sound's climate and weather (Mauger et al., 2021). The historical dataset (hereafter referred to as WRF-Obs) implemented in this study has a 1-hr timestep, a 6-km spatial resolution (73 grid points in total) and spans the years 1981-2015 (Figure 8). Boundary and initial conditions for the WRF model are created from the North American Regional Reanalysis (NARR; Mesinger et al., 2006), which uses substantial amounts of meteorological observations from various weather stations and remote sensing datasets to create a reanalysis dataset that provides the best estimate of atmospheric conditions for each timestep at a spatial resolution of 32-km. The WRF-Obs dataset is used for model calibration since it is based on meteorological observations representing a historical climate.

3.2.2 Projected Climate Datasets

Similar to the WRF-Obs dataset, the projected forcings dynamically derive from the WRF model, which uses GCMs as boundary conditions to simulate future regional climate (Mass et al., 2022). The GCMs were generated as part of the Climate Model Inter-comparison Project phase 5 (CMIP5, Taylor et al., 2012) in which international modeling groups created a set of future climate simulations that were driven by various greenhouse gas scenarios (e.g., RCP 4.5 and 8.5) quantified by the Intergovernmental Panel on Climate Change (IPCC) 5th assessment report (Pachauri et al., 2015). The GCMs used in this study were chosen based on how well they reproduced the climate of the PNW (Brewer and Mass, 2016). GCMs lack the resolution that is needed to capture the effect of mountainous topography on precipitation, and therefore regional climate models (e.g., the WRF model) are used to downscale the GCMs.

An ensemble of WRF projections were created through the collaboration of the University of Washington's Climate Impacts Group and Cliff Mass in the Department of Atmospheric Sciences (Mass et al., 2022). There are 12 projected datasets (hereafter referred to as WRF-GCM), with each dataset representing the conditions of a specific GCM (Table 2). WRF-GCM datasets are based on the RCP 8.5 scenario, which represents a worst-case emissions scenario based on the CMIP5 group of models (Van Vuuren et al., 2011). This high-end scenario is used for the projected simulations because it follows the current trend of greenhouse gas emissions (Schwalm et al., 2020). Additionally, previous studies have shown that RCP 8.5 projections in the mid-century correspond reasonably well with RCP 4.5 projections in the late-

century (Mauger et al., 2018). WRF-GCM datasets have a 1-hr timestep, a native 12-km spatial resolution that was bi-linearly interpolated to a 6-km resolution and span the years 1970-2099. WRF-GCM datasets are used to simulate future hydrological conditions and assess changes in peak flows.

3.2.3 Climate Data Bias-Correction

The WRF-Obs dataset required bias-corrections prior to model calibration. Bias-correcting is achieved by quantifying differences or biases between the WRF-Obs dataset and historical observations within the region. Corrections are applied to the WRF-Obs dataset in order to more closely match historical observations and minimize the effects of the biases on the hydrological simulations. Biases were evaluated through two methods: 1) comparing WRF-Obs with surface weather observations, and 2) by simulating snowpack using the WRF-Obs dataset and the DHSVM, then comparing simulation outputs with snow-water equivalent (SWE) observations at Snow Telemetry (SNOTEL) sites within the basin (Figure 1).

Surface weather observations from ten weather stations within and around the upper Nooksack basin were used to evaluate the biases in the historical WRF-Obs dataset (Table 3). The observations come from three sources: 1) Snow Telemetry Bias Correction and Quality Control (SNOTEL-BCQC; Sun et al., 2019), 2) Global Historical Climate Network – Daily (GHCN-D; Menne et al., 2012), and 3) AgWeatherNet (AWN; maintained by Washington State University). SNOTEL-BCQC and GHCN-D each include daily observations of precipitation, minimum temperature, and maximum temperature. AWN includes hourly observations of precipitation, temperature, humidity, and shortwave radiation.

Temperature and precipitation observations from the weather stations were compared to the nearest WRF grid point (Figures 8-10). Elevation differences between the WRF grid points and the weather stations were accounted for by adjusting the historical temperature observations with a lapse rate of 4.5°C/km (Minder et al., 2010). Annual and monthly average biases were calculated by comparing the WRF-Obs climate data from 1981-2015 with all valid observational data over that same time period for each weather station. Precipitation biases were calculated as ratios and temperature biases were calculated as differences. Due to the lack of wind and shortwave radiation measurements within the region of the upper Nooksack basin, statewide comparisons for these variables were made between the WRF-Obs dataset and observational data

(Figure 11; Mauger et al., 2021). Both wind and shortwave radiation biases were calculated as ratios. Statewide observations of longwave radiation are lacking, so no comparisons between the WRF-Obs dataset and observational data were made. Instead of using the WRF-generated longwave radiation, empirical formulations were used to estimate longwave radiation (Unsworth and Monteith, 1975; Dilley and O'Brien, 1998), which have been shown to better estimate longwave radiation compared to WRF estimates (Currier et al., 2017). Humidity was not bias-corrected because research has shown that humidity adjustments lead to over-saturated air and conditions that aren't physically plausible (Mauger et al., 2021).

Each of the 12 WRF-GCM datasets were bias-corrected based on comparisons with the bias-corrected WRF-Obs dataset. The historical average from 1981-2015 for each WRF-GCM dataset was compared to the average of the bias-corrected WRF-Obs dataset over the same time period. Bias-correction values were determined from this comparison and then applied to the entire time-series (1970-2099) for each WRF-GCM dataset. Longwave radiation was calculated using the same empirical formulations that were used to bias-correct the WRF-Obs dataset (Unsworth and Monteith, 1975; Dilley and O'Brien, 1998).

3.3 Model Calibration

The bias-corrected WRF-Obs dataset was used as meteorological inputs (forcings) for calibration of the DHSVM. Model calibration involves systematically changing temperature, precipitation, snow-physics, soil, and vegetation parameters until simulated streamflow and SWE are statistically similar to observed values measured at various streamflow gauges and SNOTEL sites throughout the upper Nooksack basin (Figure 1). Initial calibration involved comparing the timing and magnitude of simulated SWE outputs with observed SWE measured at three Natural Resources Conservation Services (NRCS) SNOTEL sites in each of the three subbasins: the Wells Creek SNOTEL (elevation 1228 m) in the North Fork, the Middle Fork SNOTEL (1515 m), and the Elbow Lake SNOTEL (927 m) in the South Fork. Daily SWE at all three SNOTEL sites were calibrated for water years 2011-2012 and validated for water years 2006-2015 to assess the model's accuracy in producing SWE for both wet and dry years. SWE maps, showing the SWE value for each pixel within the basin at a given timestep, were created to assess snow accumulation and melt. These initial model runs allowed for an assessment of the bias-correction methods used on the WRF-Obs dataset, as well as sensitive parameters that control snowpack

production like temperature lapse rates, snow and rain thresholds, and albedo accumulation and melt constants (Sun et al., 2019).

The timing and magnitude of streamflow was assessed by comparing simulated streamflow to observed data from three USGS streamflow gauges located in each of the subbasins: on the North Fork near Glacier (12205000), the Middle Fork (12208000), and the South Fork at Saxon Bridge (12210000; Figure 7). A fourth USGS streamflow gauge located at North Cedarville (12210700) on the mainstem of the Nooksack River below the confluence of the three forks was also used to assess the model's skill in reproducing streamflow, which was particularly important since this gauge allowed for the combined assessment of each of the subbasin models. The flow times series at Cedarville from my modeling results can also be routed to flow models used to quantify flooding impacts in the lowlands. Due to the three subbasins being modeled separately, streamflow at the North Cedarville gauge was simulated by adding streamflow outputs from the Middle and South Fork mouths to the North Fork streamflow output since the North Fork model domain encompassed the North Cedarville gauge. Daily and monthly streamflow for the North and Middle Forks were calibrated and validated over the same time periods as SWE, for water years 2011-2012 and 2006-2015, respectively. The South Fork was calibrated similarly but validated for the water years 2009-2015 since the stream gauge became operational in 2008.

Graphical comparisons and statistical tests were completed for each model simulation, with the results from the previous simulation informing decisions for the next, making calibration an iterative process. The model is deemed calibrated once the timing and magnitude of SWE and streamflow are consistent with historical observations. SWE results were visually compared using the statistical software package R (R Core Team, 2022). For streamflow and peak flow calibration, the objective is to maximize the Nash-Sutcliffe efficiency (NSE; Nash and Sutcliffe, 1970) and Kling-Gupta efficiency (KGE; Table 4; Gupta et al., 2009), respectively. Model performance is considered satisfactory once daily and monthly flow simulations at each of the four gauging stations achieve an NSE value of 0.5 or greater, a KGE value of 0.5 or greater, a percent bias (PBIAS) less than ±15%, and a coefficient of determination (R^2) of 0.6 or greater (Table 4; Moriasi et al., 2015).

3.4 Projected Simulations

The bias-corrected WRF-GCM datasets and calibrated DHSVM are used to simulate projected hydrologic responses in each of the three subbasins from 1970 to 2099. A single simulation is run using each of the 12 WRF-GCM climate datasets (Table 2) for each subbasin model, totaling to 36 simulations in all. Using an ensemble of WRF-GCM datasets better captures the variability of hydrologic response and reduces the uncertainties that are associated with assessing a single dynamically-downscaled GCM. Simulation time periods span the water years 1971-2099 so that relative changes in streamflow and snowpack can be assessed for a single simulation. Rather than assessing hydrologic changes by comparing simulated future hydrologic conditions to observationally derived historical conditions, such as those in the WRF-Obs dataset, I use 30-year normals centered on the year 1995 resulting from each long-term projected simulation. This apples-to-apples comparison leads to less uncertainty when assessing changes in streamflow and snowpack because model biases within a single WRF-GCM climate dataset are the same over the entire dataset time series. To assess relative changes in streamflow and snowpack and to capture the effect of short-term variability brought on by ENSO (El Nino Southern Oscillation) and PDO (Pacific Decadal Oscillation) events, statistics are calculated over 30-year normals centered on the years 1995 (1981-2010), 2055 (2040-2069), and 2085 (2070-2099). Projected changes in streamflow and SWE for each subbasin are assessed for each individual GCM simulation and as an ensemble of the 12 dynamically-downscaled GCMs. All calibration and projected simulations were performed on Kula, Western Washington University Department of Geology's 32-core server having an Intel® Xeon® Silver 4110 2.10 GHz Processor and 96 GB RAM. One projected run (1970 to 2099) in the North Fork basin would take about 36-48 hours to run and produce about 2.2 GB of output.

3.5 Peak Flow Analysis

3.5.1 Quantifying Changes in Peak Flow Magnitude

I conducted a flood frequency analysis on modeled discharge outputs at each subbasin mouth and at Cedarville to quantify peak flow changes for each subbasin and GCM simulation over 30-year normals for the 1990s, 2050s, and 2080s. A flood frequency analysis is a technique used to relate extreme streamflow events (e.g., the discharge of a 100-year event) to their frequency of occurrence (i.e., return period) through the use of cumulative distribution functions

and annual maximum peak flow (AMPF) data. A return period (or recurrence interval) describes the probability that a certain streamflow magnitude will occur within a given timeframe, usually within a year. For example, a streamflow magnitude with a 1% chance of being equaled or exceeded in any given year has a return period of 100 years (i.e., a 100-year event). The return period associated with a specific streamflow magnitude is determined from its non-exceedance probability, which represents the probability that an AMPF magnitude will be less than or equal to the specified streamflow magnitude of a return period in any given year. The non-exceedance probabilities of specific streamflow magnitudes occurring in a year are derived from fitting cumulative distribution functions, such as Extreme Value Type 1 (Gumbel), Log-Pearson Type 3 (LP3), and Generalized-Extreme Value (GEV) distributions, to AMPF data. Studies show that GEV distributions are better suited for flood frequency analyses compared to Gumbel and LP3 distributions (Millington et al., 2011; Rahman et al., 2015).

Following methods similar to other regional flood risk studies (Tohver et al., 2014; Salathé et al., 2014; Mauger et al., 2021; Robinson, 2022), I used L-moments (Hosking, 1990) to fit GEV distributions to simulated AMPFs of multiple flow durations (i.e., 3-hour, 1-day, 3-day, and 7-day) for each 30-year normal and WRF-GCM simulation. Peak flow magnitudes associated with 2-, 5-, 10-, 20-, 50-, and 100-year return periods were statistically extrapolated from the GEV distributions for each GCM and 30-year normal. For each WRF-GCM simulation, I calculated the percent change in streamflow magnitude associated with a select return period and flow duration (e.g., 10-year event, 24-hour duration flow) from the 1990s to 2050s and 1990s to 2080s. The flood frequency analysis was automated by Robinson (2022) using R software and the lmom package (Hosking, 2022) and follows the general steps below:

1) Average hourly flows across select durations (i.e., 3-hr, 1-day, 3-day, 7-day).
2) For each 30-year normal (i.e., 1990s, 2050s, and 2080s), determine annual max peak flows and rank them according to magnitude (highest has a rank of 1 and lowest has a rank of 30).
3) Compute L-moment parameters for GEV distribution using lmom functions.
4) Derive GEV distributions from L-moment parameters to determine non-exceedance probabilities of streamflow magnitudes.
5) Compute return periods (RP) from non-exceedance probabilities (P) using the equation:

$$\mathrm{RP} = \frac{1}{1 - \mathrm{P}}$$

6) Compute the percent change in peak flow magnitudes for each GCM, return period, and flow duration from the 1990s to the 2050s and 2080s 30-year normals.

3.5.2 Quantifying Changes in Peak Flow Frequency

To quantify changes in peak flow frequency, I counted the number of occurrences in which the streamflow magnitude associated with a historical 24-hour, 10-year event was equaled or exceeded in each 30-year climate normal and WRF-GCM simulation. The historical 10-year streamflow magnitude was calculated from the calibrated WRF-Obs simulation for water years 1986-2015 using the same methods described in the flood frequency analysis above (section 3.5.1). This time period differs slightly from the 1990s normal (water years 1981-2010) because the WRF-Obs dataset begins in water year 1982 and the DHSVM requires a model spin up of a couple years to establish initial conditions of snowpack, streamflow, soil saturation, etc. The number of exceedances of a historical 10-year event and the months in which they occurred were counted over the 1990s, 2050s, and 2080s 30-year climate normals for each WRF-GCM simulation. This approach to analyze changes in peak flow frequency also serves as a way to assess model biases within each GCM since I am counting exceedances within the 1990s normal of each GCM. For example, the number of exceedances of a 10-year event should only occur three times within a 30-year period. A WRF-GCM simulation with more than three exceedances within the 1990s normal may be considered biased high in simulating streamflow compared to the WRF-Obs simulation.

3.5.3 Assessing Peak Flow Generating Mechanisms

Following the methods of other flood-related studies (Berghuijs et al., 2016; Curry and Zwiers, 2018; Musselman et al., 2018; Chegwidden et al., 2020), I used an R-script generated by Robinson (2022) to assess how peak flow generating mechanisms will change through time in each of the Nooksack subbasins. Peak flow generating mechanisms were defined based on the average conditions of the watershed prior to an AMPF and assigned via a decision tree. The possible mechanisms responsible for generating peak flows include: 1) extreme precipitation, 2) rain-on-snow (ROS), 3) snowmelt, and 4) other. The peak flow generating mechanism was classified as extreme precipitation if an AMPF occurred within four days of a precipitation event with a magnitude in the 99th percentile for that year. The mechanism was classified as ROS if an

AMPF occurred within four days of a rain event of at least 0.1 m, basin-average SWE was greater than 0.1 m, and snowmelt accounted for at least 20% of the sum of basin-wide average precipitation and snowmelt. Lastly, the mechanism was classified as snowmelt if basin-average SWE was greater than 0.1 m and reduced by at least 10% within seven days of an AMPF. If none of these classification criteria were met, the peak flow generating mechanism for an AMPF was defined as "other", which is likely the result of low-intensity precipitation falling on saturated soils. If multiple classification criteria were met, the order of assignment for the decision tree was given as snowmelt, then ROS, then extreme precipitation. The reasoning for this order is to highlight changes in the less common peak flow generating mechanisms, such as ROS events and snowmelt. This ordering also accounts for scenarios in which the classification criteria for both extreme precipitation and ROS are met (i.e., 99th percentile precipitation falling on a snowpack and producing substantial melt) and correctly identifies ROS as the peak flow generating mechanism.

I also analyzed basin-average snowmelt and changes in subbasin area with steep slopes to provide additional support in assessing peak flow generating mechanisms. For each WRF-GCM simulation and subbasin model, I used an R-script to assess changes in monthly basin-average snowmelt from the 1990s to the 2050s and 2080s. To assess changes in the potential for rapid runoff and mass-wasting during extreme precipitation events, I quantified changes in subbasin area with steep slopes due to decreases in snowpack coverage. Slope angle was calculated using a 10-meter DEM within a GIS. Steep slopes were defined as slopes greater than 25° because slope stability theory states that shallow landslides are uncommon on slopes less than 25° (Doten et al., 2006). Changes to snowpack coverage was assessed using gridded outputs of April 15th SWE from the ensemble of WRF-GCM simulations. For each pixel within the model domain, outputs of April 15th SWE were averaged over the 30-year climate normals and the ensemble of WRF-GCMs. Snowpack within the snow maps is defined by pixels with a SWE value greater than or equal to 0.1 m. By overlaying the snow maps onto the steep slopes raster, I was able to quantify the area with steep slopes that would become exposed due to declines in snowpack from the 1990s to the 2050s and 2080s.

4.0 Results

4.1 Climate Data Bias-Corrections

Prior to calibrating the DHSVM, the model was forced with the unaltered WRF-Obs climate data to create baseline outputs of streamflow and SWE for examining potential biases within the climate data. Initial simulations with the unaltered WRF-Obs data indicated that daily streamflow was under-simulated by approximately 15-20% when compared to observations at streamflow gauges and slightly over-simulated SWE at SNOTEL sites. Even with the adjustment of sensitive calibration parameters such as soil porosity, lateral conductivity, and global temperature lapse rates and rain/snow thresholds, accurate outputs of both streamflow and SWE were not able to be achieved. As such, I proceeded to bias-correct the WRF-Obs climate data.

Based on long-term average annual comparisons between surface weather observations from weather stations and the nearest WRF grid cell to each respective weather station, precipitation was being underestimated by the WRF-Obs climate data, indicating a dry bias (Figure 9). Biases differ among stations, but on average indicate that the WRF-Obs climate data underestimates annual precipitation by 5-10%. Using an R-script, I applied a bias-correction as a uniform scaling factor to each timestep at each of the 73 grid locations in the WRF-Obs climate data, similar to the bias-correction approach in a similar study in the Snohomish and Stillaguamish watersheds (Table 5; Mauger at el., 2021). The application of the precipitation bias-correction greatly improved the accuracy of simulated streamflow, with a 10% increase in precipitation resulting in only a slight under-simulation of daily streamflow (0-7%) and improved NSE and KGE scores at all stream gauges.

I used a similar bias-correction approach for the temperature time series. On average, minimum and maximum temperature comparisons between weather stations and the WRF-Obs climate data indicated a slight cold bias (i.e., WRF produced temperatures that were too cold), with a range between 0.2-0.75°C (Figure 10). Simulations with the application of a warmer bias-correction value under-simulated SWE at all SNOTEL sites, even after adjusting temperature lapse rates and snow/rain thresholds. Therefore, a value of 0.2°C was added to each timestep at each grid location in the WRF-Obs climate data (Table 5). Monthly biases were determined for both precipitation and temperature, but outputs from simulations with monthly bias-correction values were not nearly as accurate as the simulations with an annual bias-correction, with both streamflow and SWE being under-simulated.

Due to the lack of wind and shortwave radiation observations within the upper Nooksack basin region, statewide comparisons were made to determine these biases. Comparisons from a recent flood modeling study indicated that the WRF-Obs climate data overestimated both wind and shortwave radiation at all valid weather stations around Washington state (Figure 11; Mauger et al., 2021). On average, the WRF-Obs climate data overestimated wind by 40% and shortwave radiation by 10% (Table 5). Similar to temperature and precipitation, wind and shortwave radiation bias-corrections were applied as a uniform scaling factor to each timestep at each grid location in the WRF-Obs climate data.

4.2 Model Calibration

4.2.1 Snow-Water Equivalent Calibration

Initial calibration of the DHSVM involved outputting simulated SWE at grid cells near SNOTEL sites within each subbasin, then comparing the timing and magnitude of simulated SWE to observations for water years 2006-2015 (Figure 1). Sensitive parameters that affect SWE production are temperature and precipitation lapse rates, rain/snow thresholds, and albedo constants (Table 6). I used snow-physics values consistent with Sun et al. (2019) as a starting basis. Initial simulations showed that adjustments to temperature lapse rates in one subbasin did not have the same effect to SWE production in another subbasin (e.g., increasing winter lapse rates increased SWE in the North and Middle Forks but decreased SWE in the South Fork). Therefore, monthly temperature lapse rates were adjusted independently for each subbasin, though the North and Middle Forks share the same final calibrated lapse rates (Table 7). Global precipitation lapse rates were not used because the WRF climate data already account for the spatial distribution of precipitation (Mauger et al., 2021).

For each of the subbasin models, the timing of snow accumulation and melt matched closely with observations from SNOTEL sites for most water years (Figure 12), which are conveniently located at three different elevations separated by approximately 300 m (1000 ft). For the North Fork model, simulated SWE magnitudes were nearly identical to observations at the Wells Creek SNOTEL site, with some years showing a slight over-production of SWE (Figure 12). The Middle and South Fork models under-simulated SWE magnitude for most years (Figure 12). It is important to note that pixel dumps at these SNOTEL sites only indicate simulated SWE for a single grid cell in the DHSVM and are not indicative of basin-wide SWE.

Additionally, measured SWE values at SNOTEL sites have a degree of uncertainty. To lessen the uncertainty associated with basin-wide snow accumulation and melt, I used the timing and magnitude of the spring freshet and early summer flows, when snowmelt is the primary contributor to streamflow, as a means to assess the accuracy of snowpack development.

In addition to examining SWE at SNOTEL sites, I used SWE maps outputted at different timesteps to assess basin-wide snow accumulation and melt. Early simulations indicated very large SWE values for a few pixels near the peak of Mt. Baker. SWE values for these pixels kept increasing over the calibration period, indicating a seasonal accumulation effect at high elevations. This resulted in an overall cumulative increase in basin-average SWE throughout the calibration period. This issue was improved by running simulations without the WRF node that was located at the peak of Mt. Baker (Figure 8). Additionally, the removal of this WRF node improved the accuracy of simulated SWE at SNOTEL sites and lessened the seasonal accumulation effect at high elevations.

4.2.2 Streamflow Calibration

The model's ability to accurately capture streamflow was assessed by statistically comparing simulated streamflow to observed streamflow at four USGS stream gauges within the upper Nooksack basin (Figure 7). When calibrating the model, only the parameters of the most abundant soil types were adjusted, which include silt loam, upland bedrock/loam, gravelly loam, and bedrock (Table 6). Soil porosity and lateral conductivity were the most sensitive parameters that affected streamflow simulation since these factors largely control the transport and storage of subsurface water.

Overall, the calibrated simulated streamflow matched closely to observed streamflow for each of the subbasin models and at the North Cedarville gauge. Each of the subbasin models produced daily and monthly simulated streamflows that achieved R^2 and NSE scores of greater than 0.6 at all four USGS stream gauges for the 10-year calibration period, which are satisfactory according to Moriasi et al. (2015; Table 8). For most water years, the North and South Fork models under-simulated the magnitude of the spring freshet and occurred slightly later in the year when compared to observations, leading to over-simulated summer flows (Figures 13 and 14). The Middle Fork model accurately simulated the timing and magnitude of the spring freshet, but still over-simulated summer flows (Figures 13 and 14). At the North Cedarville gauge, where

the flows from the three subbasin models are combined, simulated streamflow matched closely with observations. Note that streamflow results vary year-by-year, but results are consistent across basins (e.g., summer flows are under-simulated for all basins in the 2014 and 2015 water years and over-simulated in the 2013 water year), indicating that the variation in results comes from the WRF-Obs climate data and not necessarily from the calibration of the models.

Peak flows were also accurately simulated by each of the subbasin models by varying degrees, though all models achieved daily and monthly KGE scores of greater than 0.7 (Table 8). Daily peak flows in the North Fork and at the North Cedarville gauge matched closely with observations, achieving KGE scores of 0.81 and 0.82, respectively. Additionally, most individual peak flow events are well captured at these gauges (Figure 13). For the Middle and South Forks, daily peak flows achieved KGE scores of 0.75 and 0.71 when compared to observations, proving to be slightly less accurate than the simulated peak flows at the North Fork and North Cedarville gauges (Table 8). The result of the lower KGE scores in the Middle and South Forks are attributed to the under-simulation of individual peak flow events, which is especially true in the South Fork (Figure 13).

4.3 Projected Simulations

4.3.1 Projected Climate

Temperature and precipitation are projected to change in all subbasins within the upper Nooksack basin based on an analysis of the ensemble of WRF-GCM simulations. Results are shown only for the North Fork subbasin model because it encompasses the largest area and has the highest relief (Table 1), extending from Mt. Baker to the North Cedarville gauge. Nonetheless, relative changes to temperature and precipitation in the Middle and South Fork subbasins are similar to changes in the North Fork. Basin-average annual air temperature is projected to increase by 2.3°C to 4.0°C from the 1990s to the 2050s and 2080s, respectively, based on the 30-year average across the ensemble of WRF-GCMs (Figure 15), consistent with Rogers and Mauger (2021). By the 2080s, daily average air temperatures never falls below 0°C (Figure 15). Basin-average annual precipitation is projected to increase from 2.68 m in the 1990s to 2.80 m (+4.5%) and 2.88 m (+7.5%) by the 2050s and 2080s, respectively (Figure 16). The largest increases to precipitation will occur in November, December, and January, while the summer months (June-August) are projected to get less precipitation. My analysis also indicates

that extreme precipitation intensity will increase through time. Based on the 30-year average across the ensemble of WRF-GCMs, the magnitude of annual maximum 24-hour precipitation is projected to increase from approximately 0.1 m in the 1990s to 0.12 m (+20%) and 0.13 m (+30%) by the 2050s and 2080s, respectively (Figure 17). The largest increases to precipitation intensity occur from October through January, which historically see the highest magnitudes of precipitation (Figure 18).

4.3.2 Projected Snow-Water Equivalent

Results from all three subbasin models indicate a substantial decrease in peak SWE magnitude at all three SNOTEL sites, though projected magnitudes vary by GCM (Figures 19-24). At the Wells Creek SNOTEL site in the North Fork, peak SWE is projected to decrease by approximately 0.5 m (-60%) when compared to the 1990s normal based on the 30-year average from the ensemble of WRF-GCMs (Figures 19 and 20). By the 2080s, peak SWE is projected to decrease by approximately 0.7 m (-82%) compared to the 1990s normal (Figure 19). At the Middle Fork SNOTEL site, peak SWE is projected to decrease from the hindcast average of 1.25 m by approximately 0.6 m (-48%) and 0.9 m (-72%) for the 2050s and 2080s normals, respectively (Figures 21 and 22). At the Elbow Lake SNOTEL site in the South Fork, results indicate a decrease in peak SWE of approximately 0.35 m (-64%) and 0.45 m (-82%) for the 2050s and 2080s normals, respectively (Figure 23). Results from a few WRF-GCM simulations indicate that a snowpack will be nonexistent at the Elbow Lake SNOTEL site by the end of the century based on the 30-year average of SWE (Figure 24).

The timing of snow accumulation and melt are also projected to shift through time for each subbasin. At all three SNOTEL sites, snow accumulation is projected to occur later in the fall and melt out earlier in the spring by as much as a month by the 2080s, with the most significant changes occurring at the lower elevation Elbow Lake SNOTEL in the South Fork (Figure 23). Additionally, changes to the timing of snow accumulation and melt affect the timing of peak SWE for all subbasins. Based on the WRF-GCM ensemble-average for the 1990s normal, peak SWE occurs around mid-April at the SNOTEL sites in each subbasin, but projections indicate a shift to late March by the 2080s (Figures 19, 21, and 23). In the South Fork, peak SWE plateaus from February to early April in the 2080s (Figure 23).

To examine changes to snowpack coverage within each of the subbasins, I created snow maps using gridded outputs of April 15th SWE from the ensemble of WRF-GCM simulations. For each pixel within the model domain, outputs of April 15th SWE were averaged over the 30-year climate normals and the ensemble of WRF-GCMs. Snowpack within the snow maps is defined by pixels with a SWE value greater than or equal to 0.1 m. Results indicate that snowpack area within the upper Nooksack basin will decline through time (Figure 25). Based on the ensemble-average for the 1990s normal, April 15th snowpack within the 1555 km^2 upper Nooksack basin encompasses an area of 823 km^2 (53% of basin area; Table 9). By the 2080s normal, snowpack area decreases to 375 km^2 (24% of basin area), effectively decreasing snowpack area by 55% relative to the 1990s. The largest relative reduction in snowpack coverage occurs within the transient South Fork subbasin, where snowpack area decreases by 74% by the 2080s relative to the 1990s (Table 9). The elevation of the April 15th snowline will shift from approximately 800 m in the 1990s to 1200 m in the 2080s.

4.3.3 Projected Streamflow

Projected changes to monthly streamflow at the mouths of the three forks and on the mainstem of the Nooksack River at the North Cedarville gauge are consistent with other regional modeling studies (Figures 26-29). All three subbasin models show similar changes to monthly streamflow, with an overall increase to streamflow from October to April and a decrease in snowmelt-derived streamflow from May to September (Table 10). Additionally, the second peak in the hindcast (1990s) hydrograph that is associated with snowmelt (freshet) occurs earlier in the year in the Middle and North Forks and is completely diminished in the South Fork (Figures 27-29).

Modeling results at the North Cedarville gauge indicate an increase in winter flows and decrease in summer flows, with magnitude changes becoming more significant towards the end of the century (Figure 26). The largest changes to streamflow magnitude occur in December and July, where flows increase by 45% and decrease by 64%, respectively by the 2080s (Table 10). Historically, streamflow at the North Cedarville gauge shows a two-peak hydrograph, with the second peak occurring in May due to snowmelt derived flows. By the 2050s, snowmelt derived flows appear to occur earlier in the year, with a slight bump in the hydrograph occurring in April

(Figure 26). By the 2080s, there is no discernable peak in the hydrograph that is associated with snowmelt derived flows normally seen in a transient basin.

At the mouth of the North Fork, streamflow is projected to increase in the winter and decrease in the summer (Figure 27). Although similar to results at the North Cedarville gauge, the timing and magnitude of these projected changes differ. By the 2080s, winter flows are projected to increase by 55% in December and summer flows are projected to decrease by 68% in August (Table 10). Streamflow results at the mouth of the Middle Fork show similar changes to the timing and magnitude of streamflow changes in the North Fork, with an increase in December streamflow of 56% and a decrease in August streamflow of 72% by the 2080s (Table 10). The shape of the 1990s hydrographs at the mouths of the North and Middle Forks are indicative of warmer snow-dominated basins, where the spring peak is similar or larger in size than the winter peak (Figures 27 and 28). For both basins, the timing of the spring peak shifts to earlier in the year by the 2050s, from June to May, accompanied by a decrease in magnitude. By the 2080s, the spring peak in the North Fork diminishes to a slight bump in the hydrograph (Figure 27). For the Middle Fork, the hydrograph smooths out in the spring, showing no discernible spring peak, similar to the projected hydrograph at the North Cedarville gauge (Figure 28).

Projected changes to the timing and magnitude of streamflow at the mouth of the South Fork are similar to results at the North Cedarville gauge. By the 2080s, winter flows in December are projected to increase by 42% and summer flows in July are projected to decrease by 66% (Table 10). By the 2050s, spring peak snowmelt derived flows are projected to shift from May to April, showing only a slight bump in the hydrograph compared to the more discernible peak in the historical hydrograph (Figure 29). By the 2080s, the shape of the hydrograph shows similar characteristics to the projected hydrographs of the Middle Fork and North Cedarville gauge, showing only a single peak in December.

4.3.4 Projected Peak Flow Magnitude

The magnitude of peaks flows in all three subbasins and at the North Cedarville gauge are projected to increase based on the average change across all GCMs, return periods, and flow durations (Table 11). In general, average changes in peak flow magnitudes are relatively consistent among all flow durations and return periods. The largest projected magnitude changes

occur in the rare, short duration peak flows (e.g., 100-yr, 3-hr flows), which also have the largest range of magnitude changes among WRF-GCM simulations. Additionally, the range of magnitude changes across the ensemble of WRF-GCMs for the 2050s projections are greater than the 2080s projections (Figures 30-33).

At the North Cedarville gauge, the average magnitude change across all GCMs, flow durations, and return periods is 26% and 38% by the 2050s and 2080s, respectively (Table 11). The range of magnitude change is typically smaller for the shorter return periods for both the 2050s and 2080s projections (Figure 30). Peak flow magnitude changes at the mouth of the North Fork are more severe than those projected at the North Cedarville gauge. By the 2050s and 2080s, projections indicate an increase to peak flows magnitudes of 45% and 60% respectively, based on the average across all GCMs, flow durations, and return periods (Table 11, Figure 31). At the mouth of the Middle Fork, peak flows are projected to increase by an average of 33% by the 2050s and 47% for the 2080s, though magnitudes vary among GCMs (Table 11, Figure 32). Results at the mouth of the South Fork indicate less severe changes compared to the other locations, with peak flows increasing by an average of 23% and 34% by the 2050s and 2080s, respectively (Table 11). The range of magnitudes among GCMs follows the trend at the other locations, with shorter periods having a smaller range and magnitude changes in the 2050s having a wider range than changes in the 2080s (Figure 33).

4.3.5 Projected Peak Flow Frequency

Projected simulation results indicate that the magnitude of a simulated historic 10-year peak flow (i.e., a 24-hour, 10-year peak flow discharge from the WRF-Obs simulation for the water years 1986-2015) will be exceeded more frequently at the mouths of each subbasin and at the North Cedarville gauge (Figures 34-37). At the North Cedarville gauge, the discharge of a historical WRF-Obs 10-year peak flow is 1202 cms. The number of exceedances of that historical 10-year peak flow magnitude in a 30-year period increases from the GCM ensemble median of 4 exceedances in the 1990s to 13.5 and 15.5 by the 2050s and 2080s, respectively (Figure 34). At the mouth of the North Fork, the number of exceedances of a 10-year peak flow magnitude (562 cms) increases from an ensemble median of 3.5 in the 1990s to 18 and 24 by the 2050s and 2080s (Figure 35). At the mouth of the Middle Fork, a historical 10-year peak flow (231 cms) is exceeded 7 times in the 1990s based on the GCM ensemble median (Figure 36). By

the 2050s and 2080s, the exceedances of a 10-year event increases to 24 and 35 by the 2050s and 2080s. Lastly at the mouth of the South Fork, the number of exceedances of a historical 10-year peak flow (432 cms) increases from the ensemble median of 7 in the 1990s to 18.5 and 24.5 by the 2050s and 2080s (Figure 37). Note that a peak flow with a 10-year return period is expected to be equaled or exceeded 3 times within a 30-year period. At the mouths of the three subbasins and the North Cedarville gauge, the majority of WRF-GCM simulations exceeded the historic 10-year peak flow magnitude more than 3 times in the 1990s normal. Therefore, peak flows produced by the WRF-GCM simulations may be biased high compared to peak flows produced by the WRF-Obs simulation.

In addition to projected increases in peak flow frequency, the timing of peak flows (i.e., the months in which they occur) is also projected to change through time (Figures 38-41). In the 1990s normal, November-January is typically when historic 10-year peak flows are exceeded at the mouths of the subbasins and the North Cedarville gauge, with December having the greatest number of exceedances. By the 2050s, the range of months with 10-year peak flow exceedances increases by three months, spanning October-March. By the 2080s, the month with the most exceedances shifts one month earlier to November from December (Figures 38-41).

4.3.6 Projected Peak Flow Generating Mechanisms

The analysis of peak flow generating mechanisms indicates that the majority of AMPFs produced in the ensemble of WRF-GCM simulations in the South Fork subbasin are generated by extreme precipitation events (Figure 42). In the 1990s normal, the proportion of AMPFs generated by extreme precipitation and ROS events is approximately 76% and 21%, respectively. Although less frequent, AMPFs generated by ROS events in the 1990s normal are larger in magnitude than extreme precipitation generated peak flows (441 cms vs 330 cms; Figure 42). By the 2050s and 2080s, the proportion of AMPFs generated by extreme precipitation becomes even greater, accounting for approximately 86% and 95% of all AMPFs, respectively. From the 1990s to the 2080s, the average 24-hour magnitudes of AMPFs generated by extreme precipitation and ROS events increases to 472 cms (+43%) and 547 cms (+24%), respectively (Figure 42). As the snowpack in the South Fork subbasin shrinks (Figures 23-25, Table 9), less snowmelt is available to contribute to runoff during ROS events (Figure 43), resulting in a smaller proportion of AMPFs being classified as ROS generated.

AMPF generating mechanisms were also assessed in the North and Middle Fork subbasins using the methodology and classification scheme described in Chegwidden et al. (2020) and Robinson (2022), but results from those analyses are largely inconclusive due to large amounts of snow accumulation in pixels on Mt. Baker, which skews basin-average SWE high. For both the North and Middle Forks in the 1990s, the number of AMPFs generated by ROS and extreme precipitation events are relatively proportional (i.e., 50/50), with ROS generated AMPFs having larger discharge magnitudes. By the 2080s, ROS generated AMPFs become less common, accounting for approximately 40% of all AMPFs. Additionally, the discharge magnitudes of AMPFs generated by ROS and extreme precipitation increase through time. But due to the snow accumulation effect at high elevations (>2500 m) within these subbasins causing basin-average SWE to be skewed high, a large proportion of AMPFs are likely classified as ROS when they should be classified as extreme precipitation or snowmelt. Therefore, figures for AMPF generating mechanisms in the North and Middle Forks were excluded from this report. However, basin-average snowmelt in the winter months is projected to remain relatively constant from the 1990s to the 2050s and 2080s (Figures 44 and 45), indicating that ROS events may still be relatively frequent in the North and Middle Forks since there is still a significant amount of snowmelt occurring.

As snowpack coverage declines (Table 9; Figure 25), the proportion of subbasin area with exposed steep slopes increases (Table 12). Historically, 11-13% of subbasin area is comprised of exposed steep slopes (i.e., snow-free area with slopes greater than 25°). By the 2080s, the area with exposed steep slopes more than doubles in the North (+115%), Middle (+112%), and South Fork (+103%) subbasins (Table 12). These results indicate that the area available for direct runoff will increase as snowpack coverage declines, thus increasing the likelihood that peak flows will be generated by extreme precipitation.

5.0 Discussion

5.1 Projected Hydrology of the Nooksack River Basin

Projected simulations indicate substantial changes to the hydrology of the Nooksack River basin, including a significant reduction in snowpack as temperatures increase throughout the 21st century (Figures 19-25). Along with a decrease in annual peak SWE magnitude, the timing of peak SWE will shift to earlier in the season. The basin will remain snow-free for a

longer portion of the year as the development of a snowpack takes longer to accumulate and melts out earlier in the season. In addition, a greater percentage of the basin will be snow-free as warming temperatures reduce snowpack coverage in all subbasins (Table 9, Figure 25). These findings are consistent with previous hydrology modeling studies within the Nooksack basin (Dickerson-Lange and Mitchell, 2013; Murphy, 2016). Over the past decade, regional modeling studies in other Puget Sound basins also show significant reductions in snowpack throughout the 21st century (e.g., Elsner et al., 2010; Hamlet et al., 2013; Gergel et al., 2017; Mote et al., 2018; Clifton et al., 2018; Freeman, 2019; Clarke, 2020). Compared to the ensemble-average in the 1990s, modeling results indicate that peak SWE will reduce significantly (48-64%) at all three SNOTEL sites by mid-century, with an even larger decrease (72-82%) by the end of the century when projected temperature increases are highest (Figure 15). In the South Fork subbasin, where about 75% of basin area is below 1000 m and peak elevations reach just over 2000 m (Table 1; Figure 2), a mid-April snowpack decreases in area by 74% and is nonexistent below 1000 m in elevation by the 2080s (Table 9; Figure 25).

Projected warming, declines in snowpack, and changes to the timing of snowmelt and accumulation will alter the timing and magnitude of streamflow in all three forks of the Nooksack River, with each subbasin responding differently (Figures 26-29). Winter streamflow magnitudes are projected to increase in all subbasins as a greater proportion of winter precipitation falls as rain rather than snow (Table 10). Summer streamflow magnitudes are projected to decrease due to the decline in meltwater availability resulting from a reduction in basin snowpack and projected drier summers in the PNW (Table 10). Previous modeling in the Nooksack basin and other Puget Sound watersheds have indicated similar trends in streamflow changes (e.g., Dickerson-Lange and Mitchell, 2013; Hamlet et al., 2013; Vano et al., 2015; Murphy, 2016; Frans et al., 2018; Freeman, 2019; Clarke, 2020; Mauger et al., 2021). Changes to summer streamflow magnitudes are expressed with less confidence because a glacier model was not used in this study, as my emphasis focused on calibrating the DHSVM to high winter flows. Previous hydrology and glacier modeling in the Nooksack basin found that as glacier volume and melt magnitudes decrease by the end of the century, late-summer streamflow magnitudes will decrease by 55-72% at the North Cedarville gauge, comparable with summer streamflow results from this study (Table 10; Murphy, 2016).

In the high elevation, snow-dominated subbasins of the North and Middle Forks, the spring peak of streamflow associated with snowmelt (i.e., the spring freshet) will shift to earlier in the year by the 2050s due to a smaller snowpack that melts out more quickly (Figures 27 and 28; Figures 44 and 45). By the end of the 21st century, spring peaks are nearly nonexistent in the hydrographs for each of the subbasins and the North Cedarville gauge. These changes to the timing and magnitude of streamflow indicate that the entire upper Nooksack basin will shift from a transient rain-snow basin to a rain-dominant basin by the end of the 21st century (Figure 26). Other modeling studies indicate that nearly all basins within the Puget Sound region will be classified as rain-dominant by the end of the 21st century as snowpack decreases and rainfall becomes the dominant form of precipitation (Mauger et al., 2015). However, due to the presence of Mt. Baker, there is still a seasonal snowpack that exists at the higher elevations within the North and Middle Fork subbasins (Table 9; Figures 19-22). As such, the North Fork subbasin (and the upper portions of the Middle Fork subbasin) may still be classified as a transient rain-snow by the 2080s due to the small spring freshet that occurs in the hydrograph at the mouth of the North Fork (Figure 27).

5.2 Peak Flow Projections

Peak flows in the Nooksack River are projected to increase in both magnitude and frequency for all WRF-GCM simulations because of a declining snowpack (Figure 25) and higher intensity precipitation events (Figure 17). For the winter months in the 1990s relative to the 2050s and 2080s, peak flows are lower in magnitude because a greater area of the basin has a developed snowpack. A snowpack has the ability to store and attenuate rainfall runoff. As temperatures increase, a greater proportion of precipitation will fall as rain rather than snow, resulting in a decline in snowpack and an increase in the area available for direct runoff (Figure 25). This translates to a greater volume of water contributing more directly to streams and rivers during winter precipitation events. Additionally, heavy winter precipitation events, such as atmospheric rivers, are projected to become more frequent and intense, particularly in the second half of the century (Figures 17 and 18; Warner et al., 2015). More intense and frequent rainfall results in more direct runoff to streams causing higher streamflows.

Based on the average magnitude change across the ensemble of GCMs, return periods, and flow durations, peak flow magnitudes will increase by 34-60% by the end of the 21st century,

depending on the location of the river (Table 11). The magnitude and range of peak flow changes tend to be larger for the higher elevation, snowmelt dominant North and Middle Forks (Figures 31 and 32). One potential reason for larger peak flow magnitude changes in the North and Middle Forks is their higher reliefs compared to the South Fork (Table 1). As snowpack extent decreases through time, a greater proportion of basin area with steep slopes and thin soils will be exposed, resulting in a more significant contribution of rainfall runoff to rivers during rain events (Table 12; Tohver et al., 2014). Another reason is that ROS events are likely occurring at higher elevations with greater intensity in a future climate (Musselman et al., 2018). Historically, prime conditions for ROS (i.e., a snowpack that is thick enough to produce significant melt, but thin enough that water does not percolate through the snowpack and refreeze) occur between the elevations of 400-800 m (Brunengo et al., 1992; WA DNR, 2021). As temperatures increase, the prime conditions needed for ROS will transition to higher elevations. Thus, ROS events will still occur at higher elevations in the North and Middle Forks by the end of the 21st century (Figures 44 and 45), whereas they become obsolete in the South Fork subbasin (Figures 42 and 43). Paired with more intense precipitation (Figure 17), the magnitude of runoff generated from ROS events will increase, thus contributing more water to streams and producing higher stream discharge. Ultimately, the reason for larger peak flow changes in the North and Middle Forks compared to the South Fork could be a combination of the above factors (e.g., heavy rain falling on exposed, steep slopes in mid-to-low elevations combined with heavy rain falling on a prime ROS snowpack at high elevations). Other high elevation, snowmelt dominant basins within the Puget Sound region also show larger changes to peak flow magnitudes when compared to magnitude changes in mid-to-low elevation basins (Salathé et al., 2014; Mauger et al., 2015).

Peak flows are projected to occur earlier in the year and the length of the flood season will increase because of the effects of warmer winters on the basins described above (Figures 34-37). More frequent heavy rain events will likely be the main driver for more frequent peak flows (Figures 17 and 18; Warner et al., 2015). The month with the most exceedances of a historical 10-year peak flow event within a 30-year period is projected to shift from December (1990s) to November by the end of the century (2080s; Figures 38-41). Other watershed studies in the PNW also indicate an earlier shift in the timing of peak flows (Tohver et al., 2014; Salathé et al., 2014; Robinson, 2022). Historically, November, December, and January are the months with the only exceedances of a 10-year event, but by the end of the century, October and February show

exceedances as well. Therefore, the potential for flood-generating peak flows is projected to extend approximately three more months out of the year, effectively increasing the length of the flood season.

5.3 Implications for Salmon and Flooding

Projected changes to the hydrology of the Nooksack River basin will have negative consequences on people, infrastructure, and ecosystems, including salmon. Over the past century, salmon runs in the Nooksack River have declined significantly (Grah and Beaulieu, 2013). Salmon runs will likely continue to decline as the intensity and frequency of winter floods increase throughout the 21st century. The egg-to-fry survival rates of salmon will decline as higher magnitude peak flows increase the intensity and frequency of redd and egg scouring (Mantua et al., 2010). Increased peak flows will also reduce the availability of flood refugia (i.e., slow-water habitats) through the destruction of log jams, and displace rearing juveniles downstream of ideal habitats (Beechie et al., 2013).

Lower summer flows and increasing stream temperatures will also negatively affect salmon populations around the Puget Sound region as the frequency and duration of thermal tolerance exceedances increase (Mauger et al., 2015). Similar trends of increasing stream temperature are projected for the Nooksack River (Truitt, 2018). The South Fork of the Nooksack River, relative to the North and Middle Forks, is more susceptible to increasing stream temperatures due to its lower relief and a significant reduction in projected snowpack. The North and Middle Forks will see more significant increases in stream temperatures towards the end of the century as the buffering effect of meltwater diminishes due to declines in snowpack and glacier volume (Murphy, 2016).

As peak flows increase in magnitude and frequency due to a declining snowpack and intensifying rain events, flood risk will increase along the Nooksack River. Glacier loss and more frequent mass-wasting caused by a greater proportion of basin area exposed to steep terrain and heavier rain will likely increase sediment supply to rivers (Table 12; Murphy, 2016; Knapp, 2018). Sediment supply from those sources can exacerbate flooding by increasing river bed elevation (Pfeiffer et al., 2019). The combination of higher peak flows and increased sedimentation will likely flood a larger area, impacting more infrastructure and agriculture in areas around the Nooksack River. These changes to peak flows and sedimentation also have

negative implications for the Everson overflow, which will likely see more frequent overtopping and subsequent flooding of communities within the Sumas basin northeast of Everson. Additionally, these areas within the floodplain may be inundated more frequently due to increases in the frequency of flood-inducing peak flows (Figures 33-40), resulting in an increase to the cost of protecting, maintaining, and rebuilding infrastructure (Mauger et al., 2015). Nooksack River flooding near the coast will also become more severe as sea levels rise, making it more difficult for flood waters to drain into the Puget Sound. A study of the Skagit River floodplain found that the area flooded by a 100-year event is projected to increase by 74% by the end of the century as a result of higher peak flows and sea level rise (Hamman et al., 2016).

5.4 Uncertainty and Model Limitations

Projected changes to hydrology and peak flows within the Nooksack basin come with a degree of uncertainty due to multiple sources within the methodology and limitations of the DHSVM. One source of uncertainty comes from the variability in projections among GCMs. The ensemble of WRF-GCM simulations provide a range of predictions for future streamflow and SWE, with each GCM representing a possible future climate scenario. As such, the projections from each GCM simulation should be considered equally valid. This uncertainty was limited by averaging projected changes across the ensemble of WRF-GCMs. Our analysis of peak flow frequencies also indicates that the WRF-GCM simulations may be biased to produce higher peak flows since the magnitude of a historical 10-year peak flow from the WRF-Obs simulation was exceeded more than three times in the 1990s for many of the WRF-GCM simulations. Another source of uncertainty comes from the relatively coarse spatial resolution of the climate data. In this study, the WRF model produces climate data at a 12-km resolution, which may not be able to accurately resolve certain weather patterns within the complex topography of the North Cascades. Additionally, the use of 30-year normals constrains the ability to accurately quantify rarer peak flows associated with larger return periods, such as 50- and 100-year events. In order to estimate peak flows associated with these events, values must be extrapolated from the GEV distributions. To minimize this uncertainty, results were averaged across multiple flow durations and return periods to assess the overall magnitude change of future peak flows. Smaller return period estimates (i.e., 2-, 5-, and 10-year events) are projected with more confidence since they occur multiple times within a 30-year period.

Additional uncertainty comes from limitations within the DHSVM. In this study, a static landcover grid is used throughout the entirety of the simulation period. Deforestation, ecological growth, urbanization, and wildfires will likely occur within the Nooksack basin over the next century, which will affect hydrological processes and ultimately alter future flows. Additionally, road networks (i.e., paved roadways and logging roads) and culverts were not included in the model, which have the ability to route runoff more quickly to streams, resulting in higher average flows during storm events (Dymond et al., 2014). However, the effects of this infrastructure were implicitly captured by the hydraulic properties of the soils in the calibration of the streamflows. Future work could modify the landcover grid and include a road network in the DHSVM to more accurately assess how a changing basin landscape will affect future streamflow in the Nooksack River. Simplified flow processes in the DHSVM also provide another degree of uncertainty in regard to streamflow discharge magnitudes. Overbank flooding reduces downstream discharge by storing water in the floodplain of a river. In the DSHVM, overbank flooding isn't simulated because simulated streamflow remains within the stream channel unless it intercepts an unsaturated grid cell, which is unlikely during peak flows when soil saturation is very high. Therefore, simulated peak flows may be biased high compared to observed peak flows at streamflow gauging stations, resulting in higher peak flows in the WRF-GCM simulations.

One of the main purposes of this study was to provide projections for future peak flows for use in flood inundation mapping. However, since this study focused on the upper Nooksack basin beginning at the North Cedarville streamflow gauge, there is uncertainty in the accuracy of these peak flow projections at locations downstream of Everson. To accurately assess future flooding in the lowlands of the Nooksack basin, the overflows at Everson need to be quantified. Hypothetically, this could be achieved by correlating river stage at the North Cedarville gauge to flow rates and overflows at Everson. However, determining the flow conditions that initiate overflows is challenging due to constant changes in river channel morphology, such as changes to river bed elevation by sedimentation or scour. For example, over a mile of river channel at Everson showed a one to three foot increase in average bed elevation from 2006 to 2015 (Floodplain Integrated Planning, 2019). In contrast, at least 8 feet of bed scour occurred at the North Cedarville gauge during the November 2021 floods (John Thompson, personal communication). Some studies have concluded that overtopping at Everson occurs when flows

exceed 1300 cms at Deming, while other studies indicate a lower initiating flow at 700 cms (Floodplain Integrated Planning, 2019). Therefore, peak flows projections from this project should be used with caution when assessing flood risk in the lowlands of the Nooksack basin, particularly downstream of Everson.

A novel aspect of this project was the use of dynamically-downscaled climate forcings. Regional climate models, such as the WRF model, that are used to dynamically-downscale reanalysis datasets and GCM projections are computationally intensive, which limits the availability of dynamically-downscaled forcings to organizations that have the computational resources. In contrast, statistically-downscaling requires much less computational requirements to downscale climate forcings, which makes them widely available and allows for multiple climate scenarios to be assessed. Therefore, the choice of using dynamically-downscaled or statistically-downscaled forcings comes into question. In assessing the results from this study and previous studies in the Nooksack basin (Dickerson-Lange and Mitchell, 2013; Murphy, 2016), I found that end-of-century projections for streamflow and SWE were similar. Therefore, statistically-downscaled forcings may be more practical for assessing overall trends in streamflow and snowpack. However, dynamically-downscaled forcings should be used to assess changes to extreme events, such as heavy precipitation and peak flows. This is because dynamically-downscaled forcings provide a physically-based representation of future extreme storms (Salathé et al., 2007, 2014), thus giving more certainty to results for future peak flow changes. Additionally, work is being done to make dynamically-downscaled forcings for the Puget Sound region available to the public (Mauger and Won, 2021).

6.0 Conclusion

Throughout the remainder of the 21st century, the Nooksack River basin will experience hydrological changes similar to other studied transient basins in the PNW and Puget Sound region. Increasing temperatures will cause more precipitation to fall as rain rather than snow, resulting in a substantially smaller snowpack. As such, winter flows will increase and the spring peak in the hydrograph will completely disappear by the end of the century at the North Cedarville gauge, shifting from a two-peak hydrograph to a single peak representative of a rain-dominant basin. A declining snowpack and intensifying winter precipitation events will increase the volume and rate at which water enters streams and rivers. These changes will result in more

frequent peak flows of greater magnitude, with the greatest increases projected to occur in the snow-dominant North and Middle Forks. Though the exact magnitude of these future changes cannot be known, an ensemble of dynamically-downscaled GCMs representing different climate narratives indicates a general trend of more frequent and higher magnitude annual peak flows.

Projected increases in peak flows have negative implications for flood risk and salmon population within the Nooksack River. The Nooksack River and surrounding communities will likely experience flooding of greater extent, frequency, and duration due to the combined effects of higher peak flows and projected sea level rise. At-risk salmon populations may be further endangered as egg and juvenile survival rates decline due to redd scour and habitat loss from faster flowing water. The results of this study can aid Whatcom County flood managers and salmon habitat restoration efforts within the Nooksack River in planning future climate adaptation strategies to mitigate the damaging effects of climate change and protect our natural resources.

7.0 References

Abatzoglou, J.T., and Brown, T.J., 2012, A comparison of statistical downscaling methods suited for wildfire applications: Statistical downscaling for wildfire applications: International Journal of Climatology, v. 32, p. 772–780, doi:10.1002/joc.2312.

Abatzoglou, J.T., Rupp, D.E., and Mote, P.W., 2014, Seasonal Climate Variability and Change in the Pacific Northwest of the United States: Journal of Climate, v. 27, p. 2125–2142, doi:10.1175/JCLI-D-13-00218.1.

Bach, A., 2002, Snowshed Contributions to the Nooksack River Watershed, North Cascades Range, Washington*: Geographical Review, v. 92, p. 192–212, doi:https://doi.org/10.1111/j.1931-0846.2002.tb00004.x.

Beechie, T. et al., 2013, Restoring Salmon Habitat for a Changing Climate: River Research and Applications, v. 29, p. 939–960, doi:https://doi.org/10.1002/rra.2590.

Berghuijs, W.R., Woods, R.A., Hutton, C.J., and Sivapalan, M., 2016, Dominant flood generating mechanisms across the United States: Geophysical Research Letters, v. 43, p. 4382–4390, doi:10.1002/2016GL068070.

Brewer, M.C., and Mass, C.F., 2016, Projected Changes in Western U.S. Large-Scale Summer Synoptic Circulations and Variability in CMIP5 Models: Journal of Climate, v. 29, p. 5965–5978, doi:10.1175/JCLI-D-15-0598.1.

Brunengo, M., Smith, S., and Bernath, S., 1992, Screening for Watershed Analysis - A GIS-Based Method of Modeling the Water Input From Rain-On-Snow Storms, For Management and Regulation of Clearcut Forest Harvest: WA DNR Forest Practices Division, 23 p.

Chegwidden, O.S., Rupp, D.E., and Nijssen, B., 2020, Climate change alters flood magnitudes and mechanisms in climatically-diverse headwaters across the northwestern United States: Environmental Research Letters, v. 15, p. 094048, doi:10.1088/1748-9326/ab986f.

Chen, X., Leung, L.R., Gao, Y., Liu, Y., Wigmosta, M., and Richmond, M., 2018, Predictability of Extreme Precipitation in Western U.S. Watersheds Based on Atmospheric River Occurrence, Intensity, and Duration: Geophysical Research Letters, v. 45, p. 11,693-11,701, doi:https://doi.org/10.1029/2018GL079831.

Clarke, K., 2020, Modeling the effects of climate change on streamflow and stream temperature in the South Fork of the Stillaguamish River [M.S. Thesis]: Bellingham, Western Washington University, 75 p.

Clifton, C.F., Day, K.T., Luce, C.H., Grant, G.E., Safeeq, M., Halofsky, J.E., and Staab, B.P., 2018, Effects of climate change on hydrology and water resources in the Blue Mountains, Oregon, USA: Climate Services, v. 10, p. 9–19, doi:10.1016/j.cliser.2018.03.001.

Currier, W.R., Thorson, T., and Lundquist, J.D., 2017, Independent Evaluation of Frozen Precipitation from WRF and PRISM in the Olympic Mountains: Journal of Hydrometeorology, v. 18, p. 2681–2703, doi:10.1175/JHM-D-17-0026.1.

Curry, C.L., and Zwiers, F.W., 2018, Examining controls on peak annual streamflow and floods in the Fraser River Basin of British Columbia: Hydrology and Earth System Sciences, v. 22, p. 2285–2309, doi:10.5194/hess-22-2285-2018.

Dickerson-Lange, S.E., and Mitchell, R., 2013, Modeling the effects of climate change projections on streamflow in the Nooksack River basin, Northwest Washington: Hydrological Processes, v. 28, p. 5236–5250, doi:10.1002/hyp.10012.

Dilley, A.C., and O'Brien, D.M., 1998, Estimating downward clear sky long-wave irradiance at the surface from screen temperature and precipitable water: Quarterly Journal of the Royal Meteorological Society, v. 124, p. 1391–1401, doi:10.1002/qj.49712454903.

Doten, C.O., Bowling, L.C., Lanini, J.S., Maurer, E.P., and Lettenmaier, D.P., 2006, A spatially distributed model for the dynamic prediction of sediment erosion and transport in mountainous forested watersheds: Water Resources Research, v. 42, doi:10.1029/2004WR003829.

Du, E., Link, T.E., Gravelle, J.A., and Hubbart, J.A., 2014, Validation and sensitivity test of the distributed hydrology soil-vegetation model (DHSVM) in a forested mountain watershed: Hydrological Processes, v. 28, p. 6196–6210, doi:10.1002/hyp.10110.

Dymond, S.F., Aust, W.M., Prisley, S.P., Eisenbies, M.H., and Vose, J.M., 2014, Application of a Distributed Process-Based Hydrologic Model to Estimate the Effects of Forest Road Density on Stormflows in the Southern Appalachians: Forest Science, v. 60, p. 1213–1223, doi:10.5849/forsci.13-605.

Elsner, M.M., Cuo, L., Voisin, N., Deems, J.S., Hamlet, A.F., Vano, J.A., Mickelson, K.E.B., Lee, S.-Y., and Lettenmaier, D.P., 2010, Implications of 21st century climate change for the hydrology of Washington State: Climatic Change, v. 102, p. 225–260, doi:10.1007/s10584-010-9855-0.

Floodplain Integrated Planning, 2019, Lower Nooksack River Geomorphic Assessment Final Report, https://www.whatcomcounty.us/2971/FLIP-Reports.

Fowler, H.J., Blenkinsop, S., and Tebaldi, C., 2007, Linking climate change modelling to impacts studies: recent advances in downscaling techniques for hydrological modelling: International Journal of Climatology, v. 27, p. 1547–1578, doi:10.1002/joc.1556.

Frans, C., Istanbulluoglu, E., Lettenmaier, D.P., Fountain, A.G., and Riedel, J., 2018, Glacier Recession and the Response of Summer Streamflow in the Pacific Northwest United States, 1960–2099: Water Resources Research, v. 54, p. 6202–6225, doi:https://doi.org/10.1029/2017WR021764.

Freeman, K., 2019, Modeling the Effects of Climate Variability on Hydrology and Stream Temperatures in the North Fork of the Stillaguamish River [M.S. Thesis]: Bellingham, Western Washington University, 88 p.

Gergel, D.R., Nijssen, B., Abatzoglou, J.T., Lettenmaier, D.P., and Stumbaugh, M.R., 2017, Effects of climate change on snowpack and fire potential in the western USA: Climatic Change, v. 141, p. 287–299, doi:10.1007/s10584-017-1899-y.

Gillespie, N. et al., 2014, Flood Effects on Road–Stream Crossing Infrastructure: Economic and Ecological Benefits of Stream Simulation Designs: Fisheries, v. 39, p. 62–76, doi:10.1080/03632415.2013.874527.

Goode, J.R., Buffington, J.M., Tonina, D., Isaak, D.J., Thurow, R.F., Wenger, S., Nagel, D., Luce, C., Tetzlaff, D., and Soulsby, C., 2013, Potential effects of climate change on streambed scour and risks to salmonid survival in snow-dominated mountain basins: Hydrological Processes, v. 27, p. 750–765, doi:https://doi.org/10.1002/hyp.9728.

Grah, O., and Beaulieu, J., 2013, The effect of climate change on glacier ablation and baseflow support in the Nooksack River basin and implications on Pacific salmonid species protection and recovery: Climatic Change, v. 120, p. 657–670, doi:10.1007/s10584-013-0747-y.

Gupta, H.V., Kling, H., Yilmaz, K.K., and Martinez, G.F., 2009, Decomposition of the mean squared error and NSE performance criteria: Implications for improving hydrological modelling: Journal of Hydrology, v. 377, p. 80–91, doi:10.1016/j.jhydrol.2009.08.003.

Hamlet, A.F., Elsner, M.M., Mauger, G.S., Lee, S.-Y., Tohver, I., and Norheim, R.A., 2013, An Overview of the Columbia Basin Climate Change Scenarios Project: Approach, Methods, and Summary of Key Results: Atmosphere-Ocean, v. 51, p. 392–415, doi:10.1080/07055900.2013.819555.

Hamman, J.J., Hamlet, A.F., Lee, S.-Y., Fuller, R., and Grossman, E.E., 2016, Combined Effects of Projected Sea Level Rise, Storm Surge, and Peak River Flows on Water Levels in the Skagit Floodplain: Northwest Science, v. 90, p. 57–78, doi:10.3955/046.090.0106.

Han, Z., and Sharif, H.O., 2021, Analysis of Flood Fatalities in the United States, 1959–2019: Water, v. 13, p. 1871, doi:10.3390/w13131871.

Hosking, J.R.M., 2022, lmom: L-Moments, https://CRAN.R-project.org/package=lmom.

Hosking, J.R.M., 1990, L-Moments: Analysis and Estimation of Distributions Using Linear Combinations of Order Statistics: Journal of the Royal Statistical Society. Series B (Methodological), v. 52, p. 105–124.

Knapp, K., 2018, The Effects of Forecasted Climate Change on Mass Wasting Susceptibility in the Nooksack River Basin [M.S. Thesis]: Bellingham, Western Washington University, 93 p.

Lee, S.-Y., Mauger, G., and Won, J., 2018, Effect of Climate Change on Flooding in King County Rivers: Using New Regional Climate Model Simulations to Quantify Changes in Flood Risk, https://cig.uw.edu/publications/effect-of-climate-change-on-flooding-in-king-county-rivers-using-new-regional-climate-model-simulations-to-quantify-changes-in-flood-risk/.

Livneh, B., Bohn, T.J., Pierce, D.W., Munoz-Arriola, F., Nijssen, B., Vose, R., Cayan, D.R., and Brekke, L., 2015, A spatially comprehensive, hydrometeorological data set for Mexico, the U.S., and Southern Canada 1950–2013: Scientific Data, v. 2, p. 150042, doi:10.1038/sdata.2015.42.

Livneh, B., Rosenberg, E.A., Lin, C., Nijssen, B., Mishra, V., Andreadis, K.M., Maurer, E.P., and Lettenmaier, D.P., 2013, A Long-Term Hydrologically Based Dataset of Land Surface Fluxes and States for the Conterminous United States: Update and Extensions: Journal of Climate, v. 26, p. 9384–9392, doi:10.1175/JCLI-D-12-00508.1.

Madsen, T., and Figdor, E., 2007, When It Rains, It Pours: Global Warming and the Rising Frequency of Extreme Precipitation in the United States, https://policycommons.net/artifacts/1167217/when-it-rains-it-pours/1720348/ (accessed January 2023).

Mantua, N., Tohver, I., and Hamlet, A., 2010, Climate change impacts on streamflow extremes and summertime stream temperature and their possible consequences for freshwater salmon habitat in Washington State: Climatic Change, v. 102, p. 187–223, doi:10.1007/s10584-010-9845-2.

Mass, C.F., Salathé, E.P., Steed, R., and Baars, J., 2022, The Mesoscale Response to Global Warming over the Pacific Northwest Evaluated Using a Regional Climate Model Ensemble: Journal of Climate, v. 35, p. 2035–2053, doi:10.1175/JCLI-D-21-0061.1.

Mass, C., Skalenakis, A., and Warner, M., 2011, Extreme Precipitation over the West Coast of North America: Is There a Trend? Journal of Hydrometeorology, v. 12, p. 310–318, doi:10.1175/2010JHM1341.1.

Mauger, G.S., Casola, J.H., Morgan, H.A., Strauch, R.L., Jones, B., Curry, B., Busch Isaksen, T.M., Whitely Binder, L., Krosby, M.B., and Snover, A.K., 2015, State of Knowledge: Climate Change in Puget Sound: Climate Impacts Group, University of Washington, doi:10.7915/CIG93777D.

Mauger, G.S., Robinson, J., Mitchell, R.J., Won, J., and Cristea, N., 2021, Climate Change & Flooding in Snohomish County: New Dynamically-Downscaled Hydrologic Model Projections, https://digital.lib.washington.edu:443/researchworks/handle/1773/48591 (accessed August 2022).

Mauger, G., and Won, J., 2021, Bias-Corrected and Dynamically-Downscaled Hourly Temperature Projections for Sea-Tac: University of Washington Climate Impacts Group Technical Report, https://digital.lib.washington.edu:443/researchworks/handle/1773/48650 (accessed October 2022).

Mauger, G., and Won, J., 2020, Projecting Future High Flows on King County Rivers: Phase 2: Climate Impacts Group, University of Washington, 18 p.

Mauger, G., Won, J., Hegewische, K., Lynch, C., Lorete, R., Serra, Y., and Salathe, E., 2018, New Projections of Changing Heavy Precipitation in King County: Climate Impacts Group, 57 p.

Menne, M.J., Durre, I., Vose, R.S., Gleason, B.E., and Houston, T.G., 2012, An Overview of the Global Historical Climatology Network-Daily Database: Journal of Atmospheric and Oceanic Technology, v. 29, p. 897–910, doi:10.1175/JTECH-D-11-00103.1.

Mesinger, F. et al., 2006, North American Regional Reanalysis: Bulletin of the American Meteorological Society, v. 87, p. 343–360, doi:10.1175/BAMS-87-3-343.

Millington, N., Das, S., and Simonovic, S., 2011, The Comparison of GEV, Log-Pearson Type 3 and Gumbel Distributions in the Upper Thames River Watershed under Global Climate Models: Water Resources Research Report, https://ir.lib.uwo.ca/wrrr/40.

Minder, J.R., Mote, P.W., and Lundquist, J.D., 2010, Surface temperature lapse rates over complex terrain: Lessons from the Cascade Mountains: Journal of Geophysical Research: Atmospheres, v. 115, doi:10.1029/2009JD013493.

Moore, S.K., Mantua, N.J., Kellogg, J.P., and Newton, J.A., 2008, Local and large-scale climate forcing of Puget Sound oceanographic properties on seasonal to interdecadal timescales: Limnology and Oceanography, v. 53, p. 1746–1758, doi:https://doi.org/10.4319/lo.2008.53.5.1746.

Moriasi, D.N., Gitau, M.W., Daggupati, P., and Pai, N., 2015, Hydrologic and Water Quality Models: Performance Measures and Evaluation Criteria: Transactions of the ASABE, v. 58, p. 1763–1785, doi:10.13031/trans.58.10715.

Mote, P.W., Li, S., Lettenmaier, D.P., Xiao, M., and Engel, R., 2018, Dramatic declines in snowpack in the western US: npj Climate and Atmospheric Science, v. 1, p. 1–6, doi:10.1038/s41612-018-0012-1.

Mote, P.W., and Salathé, E.P., 2010, Future climate in the Pacific Northwest: Climatic Change, v. 102, p. 29–50, doi:10.1007/s10584-010-9848-z.

Murphy, R.D., 2016, Modeling the Effects of Forecasted Climate Change and Glacier Recession on Late Summer Streamflow in the Upper Nooksack River Basin [M.S. Thesis]: Bellingham, Western Washington University, 104 p.

Musselman, K.N., Lehner, F., Ikeda, K., Clark, M.P., Prein, A.F., Liu, C., Barlage, M., and Rasmussen, R., 2018, Projected increases and shifts in rain-on-snow flood risk over western North America: Nature Climate Change, v. 8, p. 808–812, doi:10.1038/s41558-018-0236-4.

Nash, J.E., and Sutcliffe, J.V., 1970, River flow forecasting through conceptual models part I — A discussion of principles: Journal of Hydrology, v. 10, p. 282–290, doi:10.1016/0022-1694(70)90255-6.

NOAA, 2016, C-CAP Regional Land Cover, Coastal Change Analysis Program (C-CAP). Charleston, SC: NOAA Office for Coastal Management, https://coast.noaa.gov/digitalcoast/data/.

Pachauri, R.K., Mayer, L., and Intergovernmental Panel on Climate Change (Eds.), 2015, Climate change 2014: synthesis report: Geneva, Switzerland, Intergovernmental Panel on Climate Change, 151 p.

Pfeiffer, A.M., Collins, B.D., Anderson, S.W., Montgomery, D.R., and Istanbulluoglu, E., 2019, River Bed Elevation Variability Reflects Sediment Supply, Rather Than Peak Flows, in the Uplands of Washington State: Water Resources Research, v. 55, p. 6795–6810, doi:10.1029/2019WR025394.

PRISM Climate Group, 2020, Average Annual Precipitation (1991-2020), Washington: Oregon State University, http://prism.oregonstate.edu/projects/gallery_view.php?state=WA.

R Core Team, 2022, R: A language and environment for statistical computing, https://www.R-project.org/.

Rahman, A.S., Karim, F., and Rahman, A., 2015, Sampling variability in flood frequency analysis : how important is it? Partnering with Industry and the Community for Innovation and Impact through Modelling: Proceedings of the 21st International Congress on Modelling and Simulation (MODSIM2015), 29 November - 4 December 2015, Gold Coast, Queensland, p. 2200–2206.

Robinson, J., 2022, Modeling 21st century peak streamflows in the Stillaguamish Watershed using dynamically downscaled general circulation model projections [M.S. Thesis]: Western Washington University, 86 p.

Rogers, M., and Mauger, G.S., 2021, Pacific Northwest Climate Projection Tool: Climate Impacts Group, https://cig.uw.edu/resources/analysis-tools/pacific-northwest-climate-projection-tool/.

Rupp, D.E., Abatzoglou, J.T., and Mote, P.W., 2017, Projections of 21st century climate of the Columbia River Basin: Climate Dynamics, v. 49, p. 1783–1799, doi:10.1007/s00382-016-3418-7.

Ryberg, K., Goree, B., Williams-Sether, T., and Mason, R., 2017, The U.S. Geological Survey Peak-Flow File Data Verification Project, 2008-16: USGS Scientific Investigations Report Scientific Investigations Report 2017–5119, 76 p.

Salathé, E.P., Hamlet, A.F., Mass, C.F., Lee, S.-Y., Stumbaugh, M., and Steed, R., 2014, Estimates of Twenty-First-Century Flood Risk in the Pacific Northwest Based on Regional Climate Model Simulations: Journal of Hydrometeorology, v. 15, p. 1881–1899, doi:10.1175/JHM-D-13-0137.1.

Salathé, E.P., Mote, P.W., and Wiley, M.W., 2007, Review of scenario selection and downscaling methods for the assessment of climate change impacts on hydrology in the United States pacific northwest: International Journal of Climatology, v. 27, p. 1611–1621, doi:10.1002/joc.1540.

Schwalm, C.R., Glendon, S., and Duffy, P.B., 2020, RCP8.5 tracks cumulative CO2 emissions: Proceedings of the National Academy of Sciences, v. 117, p. 19656–19657, doi:10.1073/pnas.2007117117.

Skamarock, C., Klemp, B., Dudhia, J., Gill, O., Barker, M., Wang, W., and Powers, G., 2005, A Description of the Advanced Research WRF Version 2, doi:10.5065/D6DZ069T.

Sun, N., Wigmosta, M., Zhou, T., Lundquist, J., Dickerson-Lange, S., and Cristea, N., 2018, Evaluating the functionality and streamflow impacts of explicitly modelling forest–snow interactions and canopy gaps in a distributed hydrologic model: Hydrological Processes, v. 32, p. 2128–2140, doi:10.1002/hyp.13150.

Sun, N., Yan, H., Wigmosta, M.S., Leung, L.R., Skaggs, R., and Hou, Z., 2019, Regional Snow Parameters Estimation for Large-Domain Hydrological Applications in the Western United States: Journal of Geophysical Research: Atmospheres, v. 124, p. 5296–5313, doi:10.1029/2018JD030140.

Taylor, K.E., Stouffer, R.J., and Meehl, G.A., 2012, An Overview of CMIP5 and the Experiment Design: Bulletin of the American Meteorological Society, v. 93, p. 485–498, doi:10.1175/BAMS-D-11-00094.1.

Tohver, I.M., Hamlet, A.F., and Lee, S.-Y., 2014, Impacts of 21st-Century Climate Change on Hydrologic Extremes in the Pacific Northwest Region of North America: JAWRA Journal of the American Water Resources Association, v. 50, p. 1461–1476, doi:https://doi.org/10.1111/jawr.12199.

Touma, D., Stevenson, S., Swain, D., Singh, D., Kalashnikov, D., and Haung, X., 2022, Climate change increases risk of extreme rainfall following wildfire in the western United States, doi:10.1126/sciadv.abm0320.

Truitt, S., 2018, Modeling the Effects of Climate Change on Stream Temperature in the Nooksack River Basin [M.S. Thesis]: Belllingham, Western Washington University, 67 p.

Unsworth, M.H., and Monteith, J.L., 1975, Long-wave radiation at the ground I. Angular distribution of incoming radiation: Quarterly Journal of the Royal Meteorological Society, v. 101, p. 13–24, doi:10.1002/qj.49710142703.

USDA, 1998, State Soil Geographic Dataset for Washington State, National Cooperative Soil Survey, http://www.soilinfo.psu.edu/index.cgi?soil_data&statsgo.

USGS, 2021, Discharge at USGS 12210700 Nooksack River at North Cedarville, WA, https://waterdata.usgs.gov/wa/nwis/uv/?site_no=12210700&PARAmeter_cd=00060,00065.

Van Vuuren, D.P., Edmonds, D., Kainuma, M., Riahi, K., Thomson, A., Hibbard, K., Hurtt, G.C., Kram, T., Krey, V., Lamarque, J.F., Masui, T., Meinshausen, M., Nakicenovic, N., Smith, S.J., Rose, S.K., 2011, The representative concentration pathways: an overview: Climatic Change, v. 109, p. 5, doi:10.1007/s10584-011-0148-z.

Vano, J.A., Nijssen, B., and Lettenmaier, D.P., 2015, Seasonal hydrologic responses to climate change in the Pacific Northwest: Water Resources Research, v. 51, p. 1959–1976, doi:https://doi.org/10.1002/2014WR015909.

WA DNR, 2021, Rain On Snow, https://data-wadnr.opendata.arcgis.com/datasets/4a8339bfe8ca46b8a0a674195827e6d3_6/about.

WA DNR, 2017, Washington Lidar Portal, https://lidarportal.dnr.wa.gov/.

Warner, M.D., Mass, C.F., and Salathé, E.P., 2015, Changes in Winter Atmospheric Rivers along the North American West Coast in CMIP5 Climate Models: Journal of Hydrometeorology, v. 16, p. 118–128, doi:10.1175/JHM-D-14-0080.1.

Whatcom County, 2021, News - 2021 Flood | Whatcom County, WA - Official Website, https://www.whatcomcounty.us/3841/News---2021-Flood.

Wigmosta, M.S., Nijssen, B., and Storck, P., 2002, The Distributed Hydrology Soil Vegetation Model, *in* Mathematical Models of Small Watershed Hydrology and Applications, Littleton, Colorado, Water Resource Publications, p. 7–42.

Wigmosta, M.S., Vail, L.W., and Lettenmaier, D.P., 1994, A distributed hydrology-vegetation model for complex terrain: Water Resources Research, v. 30, p. 1665–1679, doi:10.1029/94WR00436.

8.0 Tables

Table 1: Elevation ranges and areas above 1000, 1500, and 2000 meters in each of the three subbasins. Percentages represent the proportion of basin area above an elevation threshold versus the total basin area. Basin areas were calculated based on their extent (50-meter pixel resolution) shown in Figure 1.

Basin	Elevation Range (m)	Area (km^2)						
		Basin Area	Area above 1000 m	% of Basin Area	Area above 1500 m	% of Basin Area	Area above 2000 m	% of Basin Area
North Fork	87 – 3280	746.2	367.5	49%	129.2	17%	19.1	2%
Middle Fork	87 – 3280	260.2	127.8	49%	28.9	11%	7.5	3%
South Fork	66 – 2120	477.7	119.3	25%	9.5	2%	0.1	~0%

Table 2: List of the 12 GCMs that were dynamically-downscaled by the WRF model to create the projected climate datasets. All simulations are based on the high-end RCP 8.5 greenhouse gas scenario.

Global Climate Model	Research Center	Representative Concentration Pathway (RCP)
ACCESS1.0	Commonwealth Scientific and Industrial Research Organization (CSIRO), Australia/ Bureau of Meteorology, Australia	8.5
ACCESS1.3	Commonwealth Scientific and Industrial Research Organization (CSIRO), Australia/ Bureau of Meteorology, Australia	8.5
BCC-CSM1.1	Beijing Climate Center (BCC), China Meteorological Administration	8.5
CanESM2	Canadian Centre for Climate Modeling and Analysis	8.5
CCSM4	National Center of Atmospheric Research (NCAR), USA	8.5
CSIRO-Mk3.6.0	Commonwealth Scientific and Industrial Research Organization (CSIRO) / Queensland Climate Change Centre of Excellence, Australia	8.5
FGOALS-g2	LASG, Institute of Atmospheric Physics, Chinese Academy of Sciences	8.5
GFDL-CM3	NOAA Geophysical Fluid Dynamics Laboratory, USA	8.5
GISS-E2-H	NASA Goddard Institute for Space Studies, USA	8.5
MIROC5	Atmosphere and Ocean Research Institute (The University of Tokyo), National Institute for Environmental Studies, and Japan Agency for Marine-Earth Science and Technology	8.5
MRI-CGCM3	Meteorological Research Institute, Japan	8.5
NorESM1-M	Norwegian Climate Center, Norway	8.5

Table 3: The ten weather stations within and around the upper Nooksack basin that were used to evaluate biases in the historical WRF-Obs climate data. Weather station sources include the National Resources Conservation Services snow telemetry (SNOTEL) network, the Global Historical Climate Network daily (GHCND), and Washington State University's AgWeatherNet (AWN).

Source	Name	Latitude	Longitude	Elevation (m)	Years
SNOTEL	Easy Pass	48.86	-121.44	1606	2008-2022
SNOTEL	Elbow Lake	48.69	-121.91	927	1995-2022
SNOTEL	Marten Ridge	48.76	-121.7	1073	2006-2022
SNOTEL	MF Nooksack	48.82	-121.93	1515	2002-2022
SNOTEL	Wells Creek	48.87	-121.79	1228	1995-2022
GHCND	Clearbrook HCN	48.9672	-122.3291	20	1903-2022
GHCND	Concrete PPL Fish Station	48.5397	-121.7422	59	1905-2022
GHCND	Upper Baker Dam	48.6525	-121.6931	210	1965-2022
AWN	Nooksack	48.9668	-122.3706	25	2002-2022
AWN	Lawrence	48.8837	-122.3214	45	2008-2022

Table 4: Statistical tests used to evaluate model performance during calibration. Satisfactory values are based on performance evaluation criteria (PEC) thresholds from Moriasi et al. (2015).

Statistical Test	Description	Equation	Value Range	Optimal Value	Satisfactory Value
Percent Bias (PBIAS)	Describes the average tendency of simulated data to be smaller or larger than observed data.	$\frac{\sum_{i=1}^{n} O_i - S_i}{\sum_{i=1}^{n} O_i} \times 100$	-∞ to ∞	0%	< ±15%
Coefficient of Determination (R^2)	Describes the proportion of variance in observed data explained by simulated data in a linear regression model.	$\left[\frac{\sum_{i=1}^{n}(O_i - \mu_O)(S_i - \mu_S)}{\sqrt{\sum_{i=1}^{n}(O_i - \mu_O)^2}\sqrt{\sum_{i=1}^{n}(S_i - \mu_S)^2}}\right]^2$	0 to 1	1	> 0.6
Nash-Sutcliffe Efficiency (NSE)	Describes the relative magnitude of the residual variance to observed data variance.	$1 - \frac{\sum_{i=1}^{n}(O_i - S_i)^2}{\sum_{i=1}^{n}(O_i - \mu_O)^2}$	-∞ to 1	1	> 0.5
Kling-Gupta Efficiency (KGE)	Decomposition of NSE into its components of correlation, variability bias, and mean bias.	$1 - \sqrt{(r-1)^2 + \left(\frac{\sigma_S}{\sigma_O} - 1\right)^2 + \left(\frac{\mu_S}{\mu_O} - 1\right)^2}$	-∞ to 1	1	> 0.5

n = total number of observations
i = data index (i.e., 1 to n)
O = observed data
S = simulated data
μ_o = mean of observed data
μ_s = mean of simulated data
r = linear correlation coefficient (i.e., square root of R^2)
σ_o = standard deviation of observed data
σ_s = standard deviation of simulated data

Table 5: The bias-correction values that were applied uniformly to every timestep for each of the 73 historical WRF nodes.

Climate Variable	Scaling Value
Temperature	+0.2°C
Precipitation	+10%
Wind	-40%
Shortwave Radiation	-10%

Table 6: Final calibrated values of sensitive parameters used for each of the subbasin models.

Parameter	Value		
	North Fork	**Middle Fork**	**South Fork**
Precipitation Lapse Rate (m/km)	0	0	0
Rain Threshold (°C)	1	1	1
Snow Threshold (°C)	2	1	1.5
Albedo Accumulation Lambda	0.9	0.95	0.9
Albedo Melting Lambda	0.75	0.8	0.75
Albedo Accumulation Min	0.75	0.8	0.75
Albedo Melting Min	0.45	0.5	0.45
Gap Wind Adjustment Factor	0.9	0.9	0.9
Max Surface Snow Layer Depth (m)	0.075	0.075	0.075
Silt Loam (#5)			
Lateral Conductivity (m/s)	0.004	0.004	0.004
Exponential Decrease	1.5	1.5	1
Porosity	0.25 / 0.23 / 0.2	0.25 / 0.23 / 0.2	0.25 / 0.23 / 0.2
Field Capacity	0.16 / 0.14 / 0.14	0.16 / 0.14 / 0.14	0.13 / 0.13 / 0.13
Upland Bedrock/Loam (#6)			
Lateral Conductivity (m/s)	0.001	0.0003	0.0003
Exponential Decrease	1.6	1.6	1.6
Porosity	0.4 / 0.35 / 0.3	0.3 / 0.28 / 0.25	0.3 / 0.28 / 0.25
Field Capacity	0.13 / 0.13 / 0.13	0.13 / 0.13 / 0.13	0.13 / 0.13 / 0.13
Gravelly Loam (#7)			
Lateral Conductivity (m/s)	0.008	0.008	0.008
Exponential Decrease	2	0.6	0.6
Porosity	0.4 / 0.35 / 0.3	0.4 / 0.35 / 0.3	0.4 / 0.35 / 0.3
Field Capacity	0.13 / 0.13 / 0.13	0.13 / 0.13 / 0.13	0.16 / 0.16 / 0.16
Bedrock (#15)			
Lateral Conductivity (m/s)	0.001	0.001	0.001
Exponential Decrease	2	2	2
Porosity	0.1 / 0.08 / 0.08	0.1 / 0.08 / 0.08	0.1 / 0.08 / 0.08
Field Capacity	0.05 / 0.05 / 0.05	0.05 / 0.05 / 0.05	0.05 / 0.05 / 0.05

Table 7: Monthly temperature lapse rates used for each of the subbasin models.

Month	Temperature Lapse Rates (°C/km)		
	North Fork	Middle Fork	South Fork
January	-6	-6	-4
February	-6	-6	-4
March	-5	-5	-4
April	-4	-4	-4
May	-4	-4	-4
June	-4	-4	-4
July	-5	-5	-4
August	-5	-5	-4
September	-5	-5	-4
October	-5	-5	-4
November	-6	-6	-4
December	-6	-6	-4

Table 8: Daily and monthly simulated streamflow evaluation scores for percent bias (PBIAS), coefficient of determination (R^2), Nash-Sutcliffe Efficiency (NSE), and Kling-Gupta Efficiency (KGE) at stream gauges within each subbasin and on the mainstem of the Nooksack River. Performance evaluation criteria (PEC) from Moriasi et al. (2015) are shown in the bottom rows. PEC thresholds do not exist for KGE, thus NSE PCE thresholds are used as a reference.

Site Name (USGS ID)	Water Years	Daily / Monthly			
		PBIAS	R^2	NSE	KGE
Nooksack River at North Cedarville (12210700)	2006-2015	4.4 / 4.5	0.69 / 0.77	0.65 / 0.73	0.82 / 0.86
NF Nooksack River near Glacier (12205000)	2006-2015	-9.2 / -9.3	0.7 / 0.72	0.66 / 0.69	0.81 / 0.81
MF Nooksack River near Deming (12208000)	2006-2015	0.8 / -0.1	0.61 / 0.66	0.6 / 0.64	0.75 / 0.8
SF Nooksack River at Saxon Bridge (12210000)	2009-2015	-8.1 / -8.4	0.67 / 0.73	0.66 / 0.71	0.71 / 0.77
	Very Good	% < ±5	$R^2 > 0.85$	NSE > 0.8	KGE > 0.8
	Good	±5 ≤ % < ±10	$0.75 < R^2 \leq 0.85$	0.7 < NSE ≤ 0.8	0.7 < KGE ≤ 0.8
	Satisfactory	±10 ≤ % < ±15	$0.6 < R^2 \leq 0.75$	0.5 < NSE ≤ 0.7	0.5 < KGE ≤ 0.7
	Not Satisfactory	% ≥ ±15	$R^2 \leq 0.6$	NSE ≤ 0.5	KGE ≤ 0.5

Table 9: Projected changes to snowpack coverage for each subbasin. Snowpack area is based on the GCM ensemble 30-year average SWE for pixel values greater than or equal to 0.1 m in depth on April 15th. Basin areas were calculated from DHSVM subbasin masks with a 150-meter pixel resolution.

Basin	1990s		2050s		2080s	
	Snowpack Area (km^2)	% of Basin Area	Snowpack Area (km^2)	% of Basin Area	Snowpack Area (km^2)	% of Basin Area
North Fork	470.7	56%	343.2	41%	252.8	30%
Middle Fork	150.1	61%	106.2	43%	68.6	28%
South Fork	202.6	44%	120.8	26%	53.3	11%
Total	823.4	53%	570.2	37%	374.7	24%

Table 10: Average projected changes to monthly streamflow across all GCMs at the mouths of the three forks and the North Cedarville gauge. Percentages show changes for the 2050s and 2080s 30-year normals relative to the 1990s normal.

Month	North Cedarville		North Fork		Middle Fork		South Fork	
	2050s	2080s	2050s	2080s	2050s	2080s	2050s	2080s
January	25%	43%	29%	52%	31%	55%	24%	40%
February	16%	33%	20%	43%	22%	46%	15%	31%
March	14%	26%	19%	37%	21%	38%	13%	23%
April	13%	12%	21%	27%	21%	26%	11%	8%
May	-14%	-26%	0%	-8%	-4%	-13%	-19%	-32%
June	-33%	-50%	-17%	-37%	-20%	-39%	-41%	-58%
July	-45%	-64%	-39%	-62%	-39%	-63%	-53%	-66%
August	-46%	-62%	-51%	-68%	-54%	-72%	-40%	-54%
September	-14%	-12%	-24%	-31%	-27%	-30%	-8%	-4%
October	13%	18%	12%	14%	12%	15%	13%	18%
November	25%	34%	29%	43%	29%	42%	23%	31%
December	28%	45%	33%	55%	34%	56%	26%	42%

Table 11: Average projected changes to peak flow magnitudes across all GCMs for multiple return periods and flow durations. Percentages show changes for the 2050s and 2080s 30-year normals relative to the 1990s normal.

Return Period	Duration	North Cedarville		North Fork		Middle Fork		South Fork	
		2050s	2080s	2050s	2080s	2050s	2080s	2050s	2080s
2-yr	3-hr	26%	42%	42%	66%	37%	57%	24%	38%
	24-hr	25%	39%	43%	65%	35%	54%	22%	35%
	72-hr	24%	34%	39%	54%	33%	45%	21%	31%
	168-hr	25%	34%	34%	47%	32%	44%	23%	31%
5-yr	3-hr	25%	35%	44%	61%	32%	44%	22%	31%
	24-hr	25%	37%	46%	63%	34%	49%	22%	33%
	72-hr	25%	34%	43%	55%	33%	45%	22%	31%
	168-hr	26%	34%	36%	48%	33%	42%	24%	31%
10-yr	3-hr	24%	36%	45%	62%	29%	41%	20%	32%
	24-hr	26%	38%	48%	63%	34%	48%	22%	33%
	72-hr	25%	35%	45%	57%	33%	45%	22%	32%
	168-hr	27%	34%	38%	50%	33%	43%	25%	31%
20-yr	3-hr	24%	38%	46%	65%	27%	40%	19%	34%
	24-hr	26%	39%	49%	64%	34%	48%	22%	35%
	72-hr	25%	37%	46%	59%	33%	47%	22%	33%
	168-hr	28%	35%	40%	51%	34%	44%	25%	32%
50-yr	3-hr	24%	44%	48%	72%	25%	42%	19%	39%
	24-hr	27%	41%	51%	66%	35%	49%	23%	37%
	72-hr	26%	40%	47%	62%	32%	49%	23%	36%
	168-hr	30%	37%	43%	53%	35%	46%	27%	34%
100-yr	3-hr	24%	49%	49%	79%	24%	44%	18%	44%
	24-hr	29%	44%	53%	69%	37%	51%	24%	39%
	72-hr	27%	43%	48%	65%	32%	52%	23%	39%
	168-hr	32%	39%	46%	55%	37%	47%	29%	35%
Average		**26%**	**38%**	**45%**	**60%**	**33%**	**47%**	**23%**	**34%**

Table 12: Projected changes to the area of exposed steep slopes (i.e., slopes > 25° with no snowpack) due to changes in April 15th snowpack coverage. The area column represents the area of slopes greater than 25° within the snowpack-free portion of a subbasin (Figure 24). Percentages represent the proportion of exposed steep slope area to subbasin area. This analysis uses a 10-meter pixel resolution to determine slope angle.

Basin	1990s		2050s		2080s	
	Area w/ Exposed Steep Slopes (km^2)	**% of Basin Area**	**Area w/ Exposed Steep Slopes (km^2)**	**% of Basin Area (% Change)**	**Area w/ Exposed Steep Slopes (km^2)**	**% of Basin Area (% Change)**
North Fork	91.7	11%	148	18% (+61%)	196.9	23% (+115%)
Middle Fork	33.2	13%	52.6	21% (+58%)	70.5	28% (+112%)
South Fork	48.8	11%	69.8	15% (+43%)	98.9	21% (+103%)

9.0 Figures

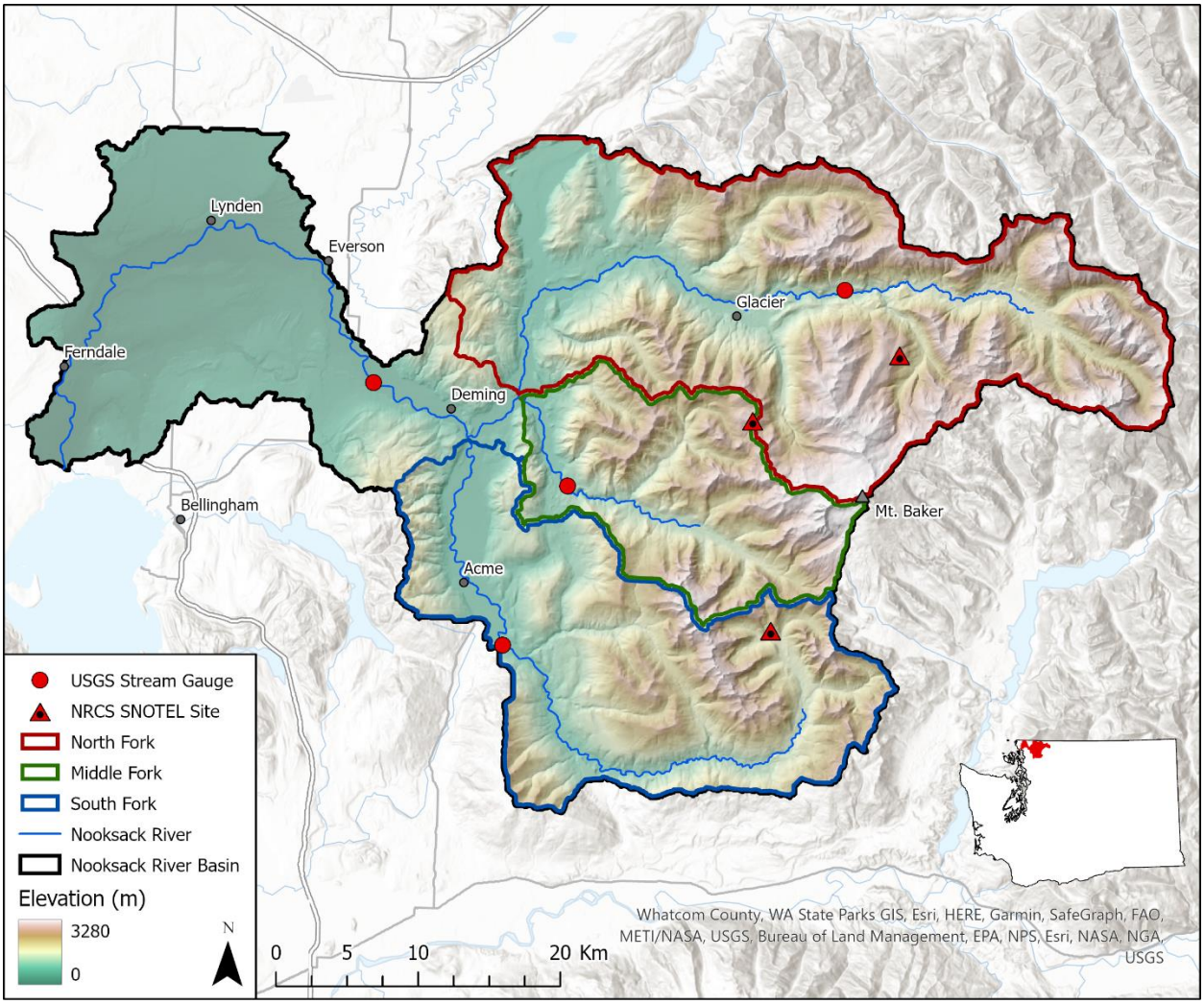

Figure 1: The Nooksack River basin is located in the North Cascades, Washington State. The upper Nooksack basin is the focus of this study and comprises of three main subbasins: North Fork, Middle Fork, and South Fork.

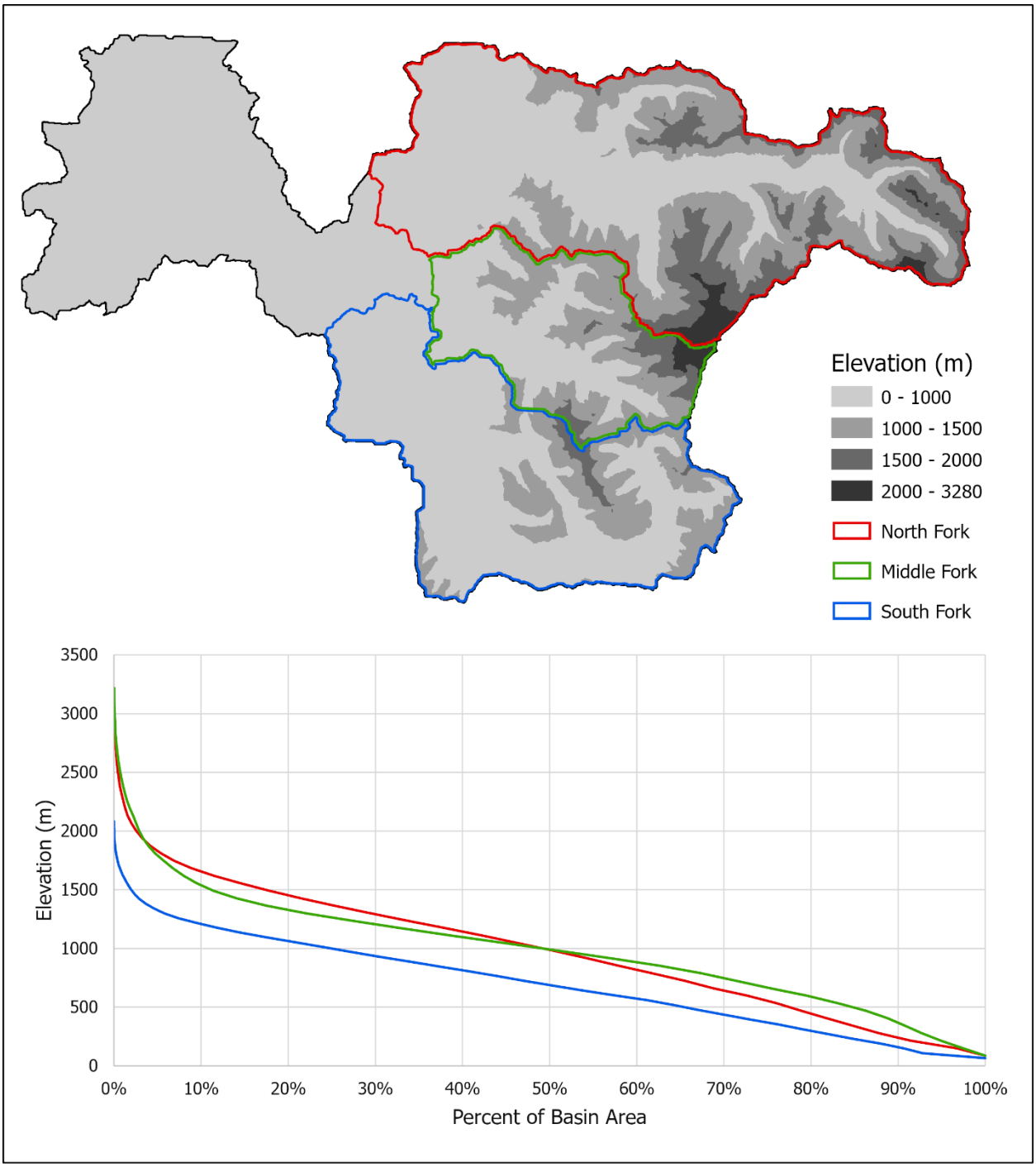

Figure 2: (Top) Elevation bands for the Nooksack River basin. (Bottom) Hypsometric curves for the North, Middle, and South Fork Nooksack subbasins. The curves indicate the percentage of basin area that is below a specific elevation.

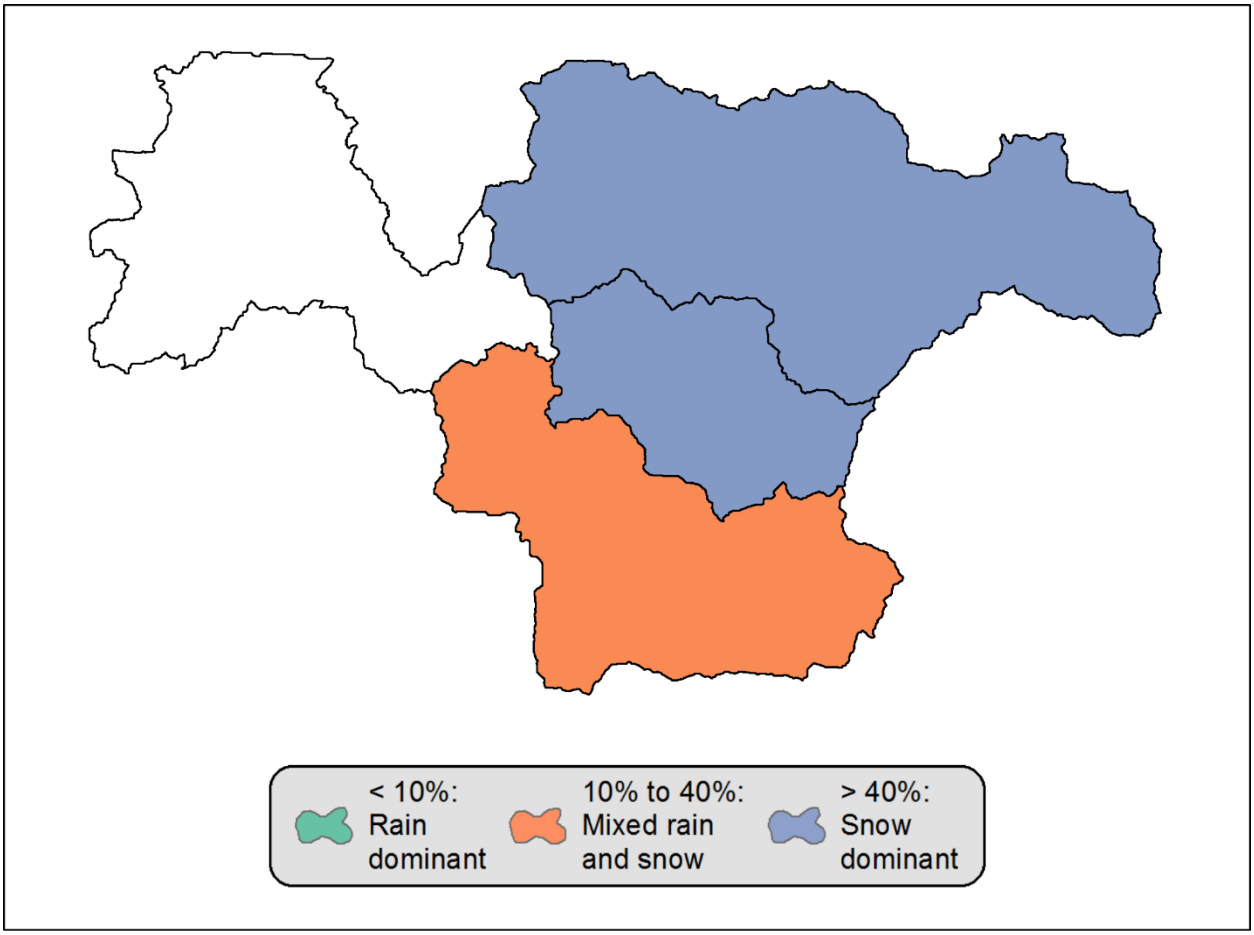

Figure 3: Watershed classifications for the North, Middle, and South Fork subbasins. The North and Middle Forks are classified as snow-dominant (> 40% of winter precipitation falling as snow) and the South Fork is classified as mixed snow and rain (between 10-40% of winter precipitation falling as snow), also referred to as transient or transitional (modified from Hamlet et al., 2013).

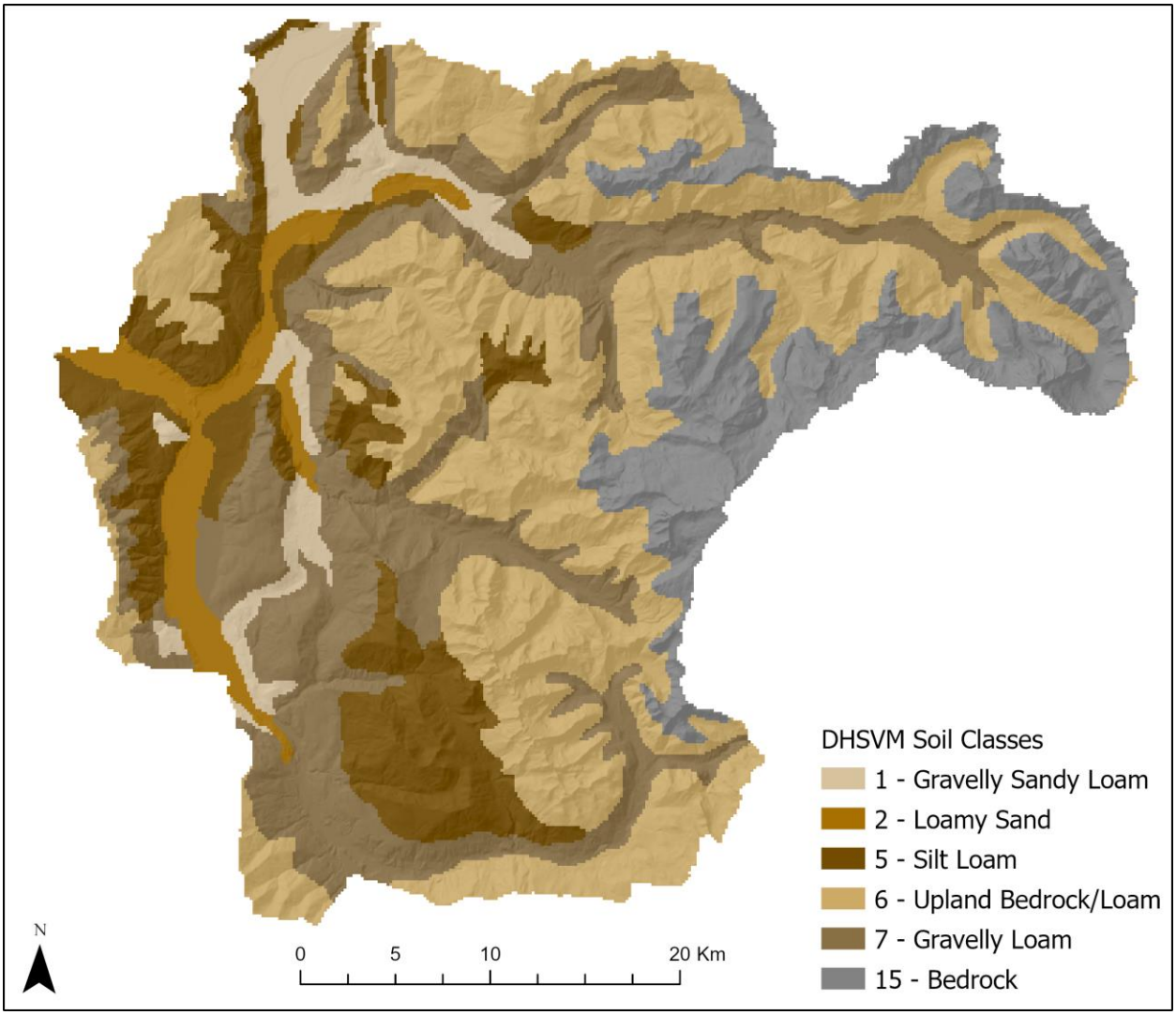

Figure 4: Soil classes within the upper Nooksack basin. The data derives from the STATSGO dataset and was converted from polygons to gridded data at a 150-meter resolution. The data was reclassified to correspond with soil classes within the DHSVM configuration.

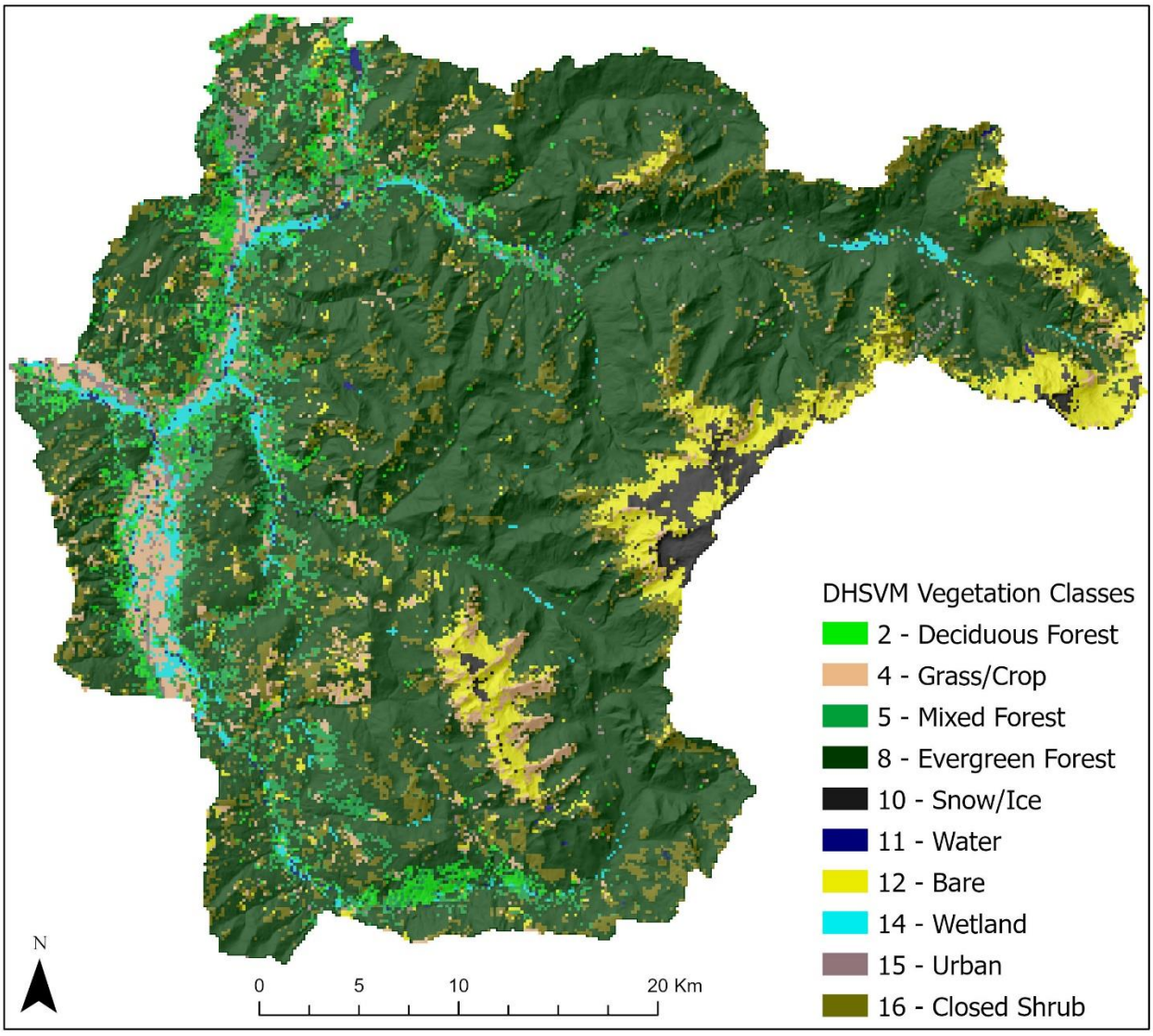

Figure 5: Landcover classes within the upper Nooksack basin. The data derives from the NOAA C-CAP 2016 gridded dataset and was resampled from a 30-meter resolution to a 150-meter resolution. The data was reclassified to correspond with landcover and vegetation classes within the DHSVM configuration file.

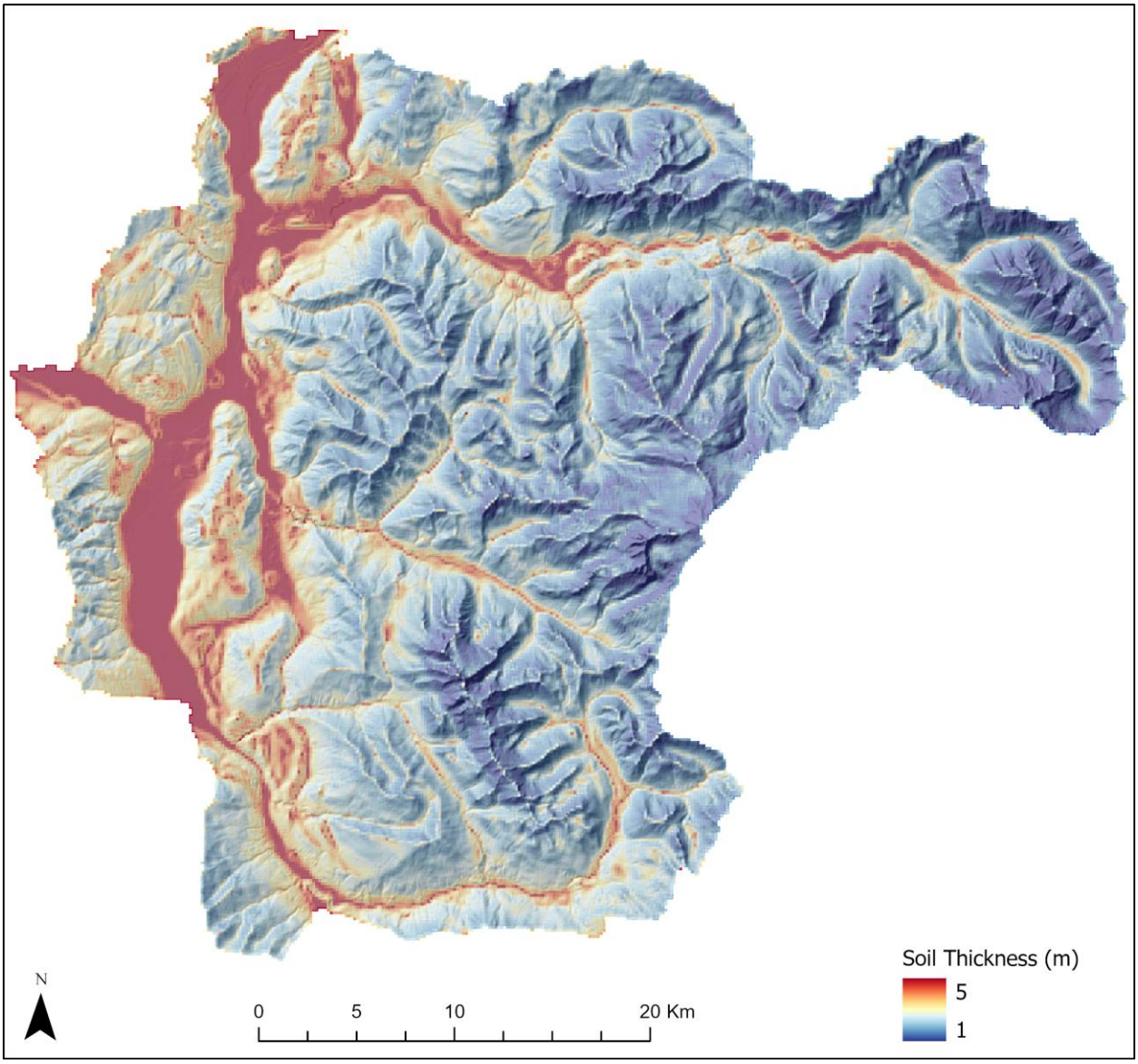

Figure 6: Soil thickness within the upper Nooksack basin. A python script executes an ArcGIS workflow that generates a soil thickness grid using a DEM, a watershed boundary shapefile, and a user-defined soil thickness range.

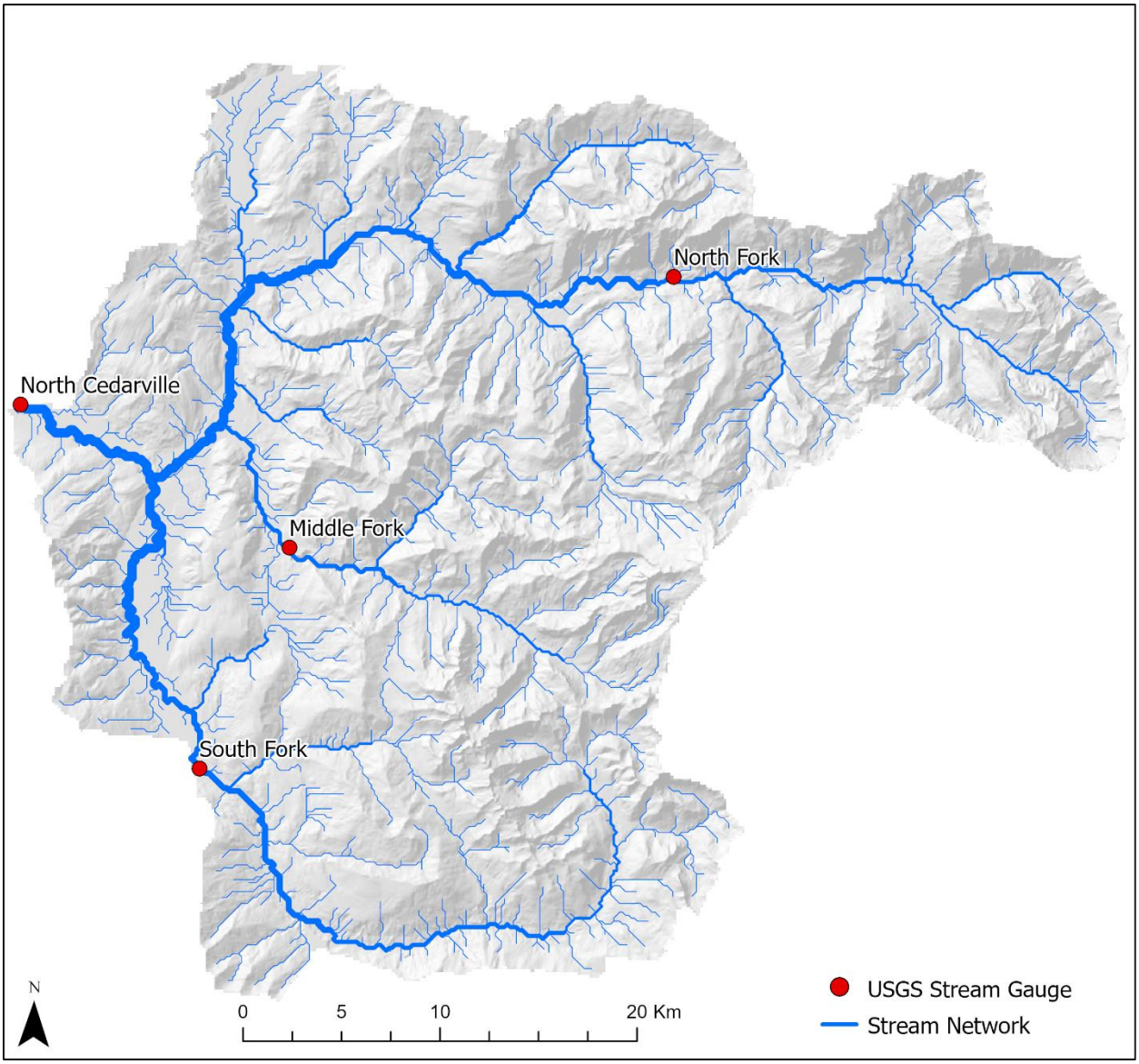

Figure 7: Stream network within the upper Nooksack basin. A python script executes an ArcGIS workflow of hydrology tools that generates a stream network consisting of line segments using a DEM, a watershed boundary shapefile, and a user-defined source area (e.g., 500,000 m^2).

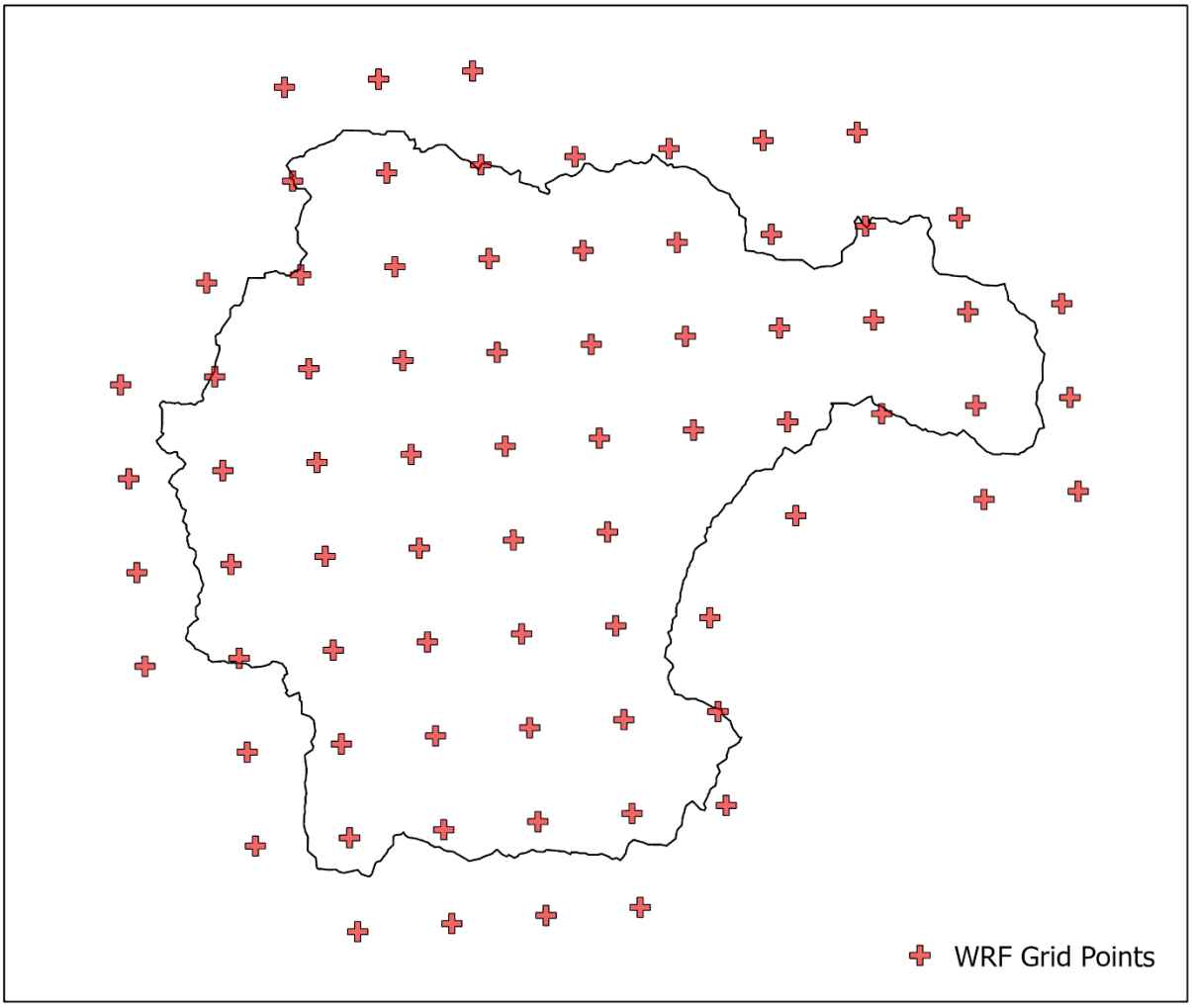

Figure 8: Location of the 73 WRF grid points within and around the upper Nooksack basin. The grid points are separated by 6 kilometers and have an hourly timestep. The WRF grid point located near the peak of Mt. Baker was not included in this study.

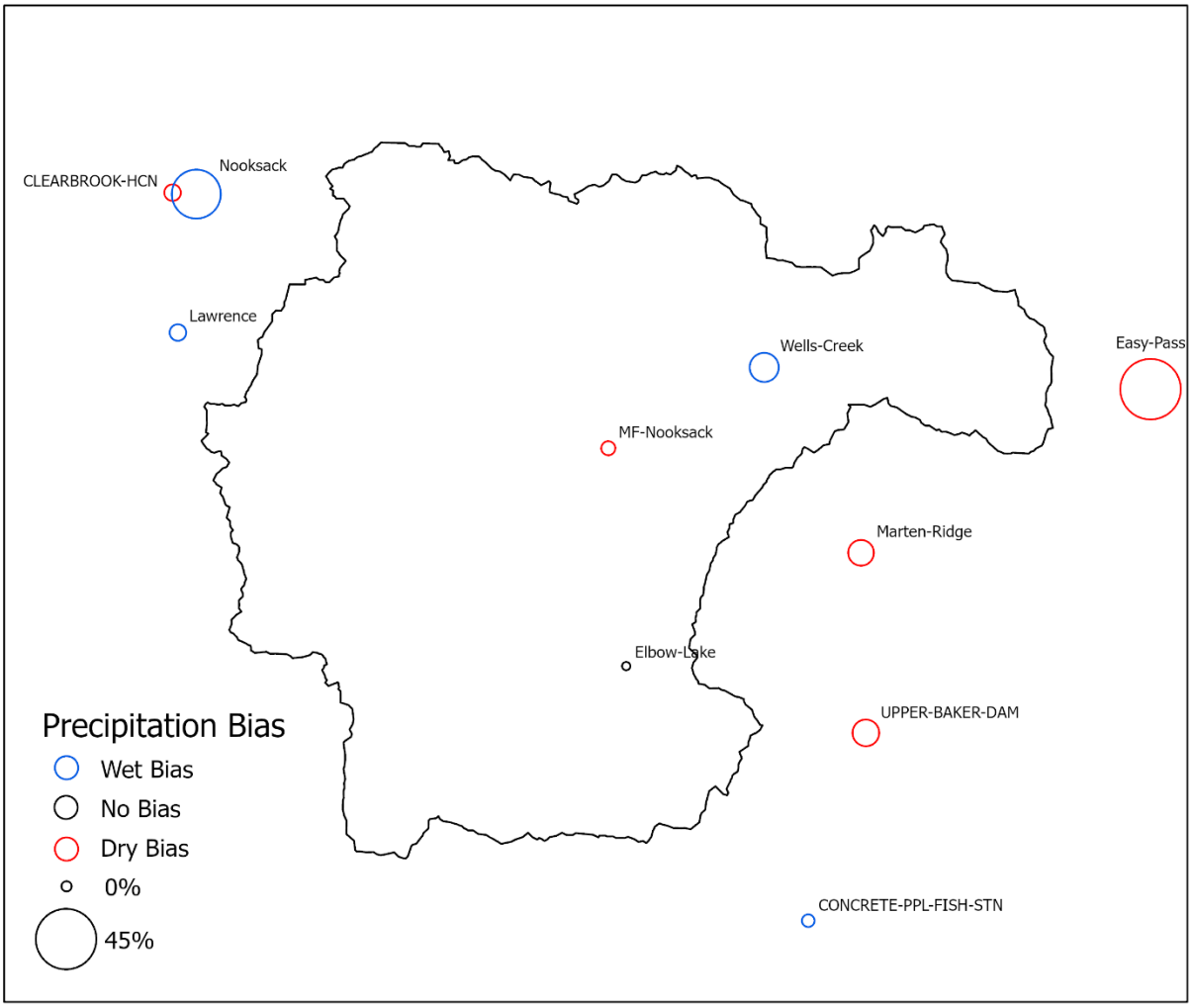

Figure 9: Map of the annual average precipitation biases for the historical WRF climate dataset. The color of the circle denotes the type of bias, while the size denotes the magnitude of the bias relative to observed climate data. A wet bias indicates that the historical WRF climate data produced more precipitation than observed precipitation measured at weather stations.

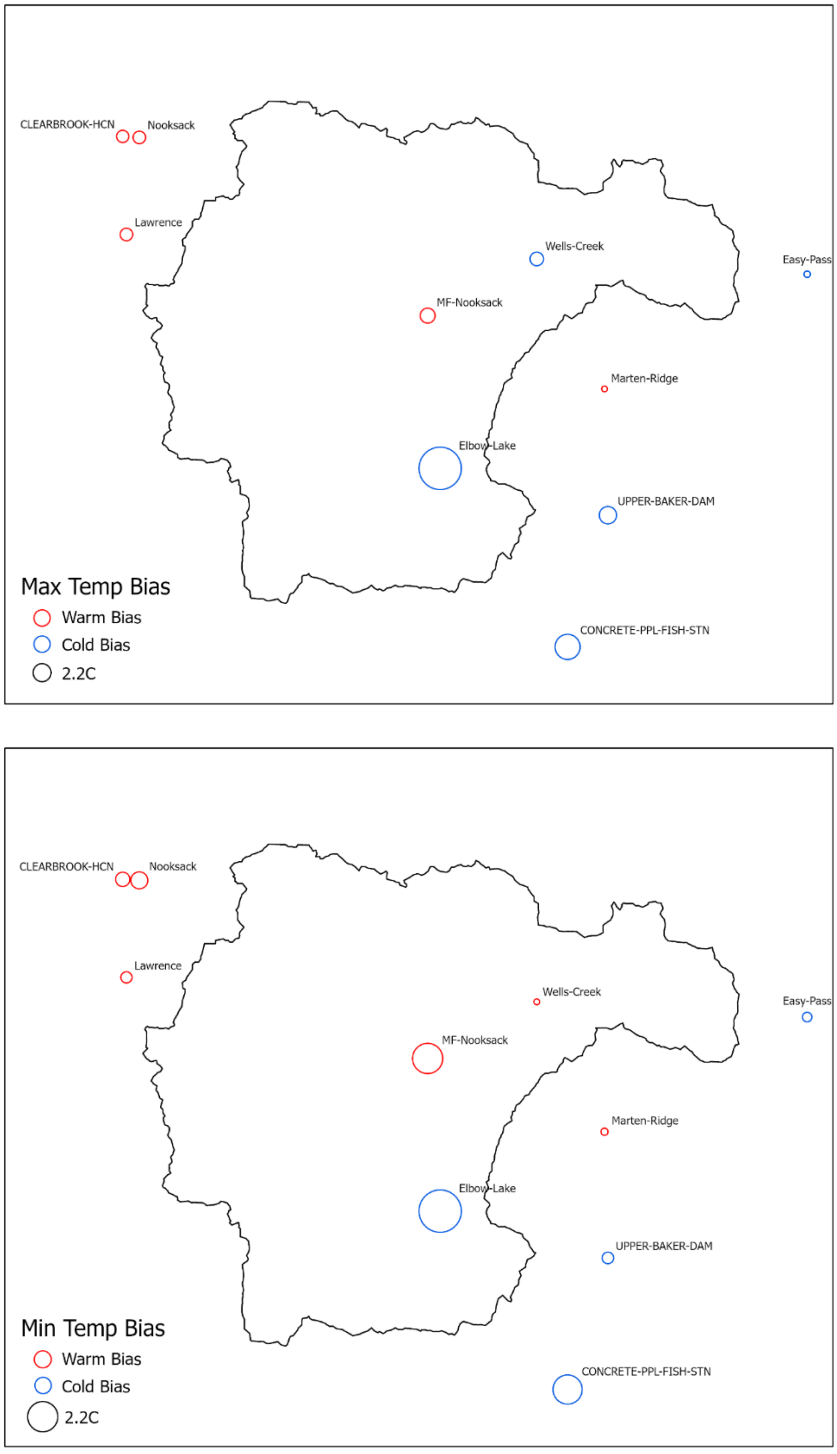

Figure 10: Map of the annual average of maximum (top) and minimum (bottom) temperature biases for the historical WRF climate dataset. The color of the circle denotes the type of bias, while the size denotes the magnitude of the bias relative to observed climate data. A warm bias indicates that the historical WRF climate data produced warmer temperatures than observed temperature measured at weather stations.

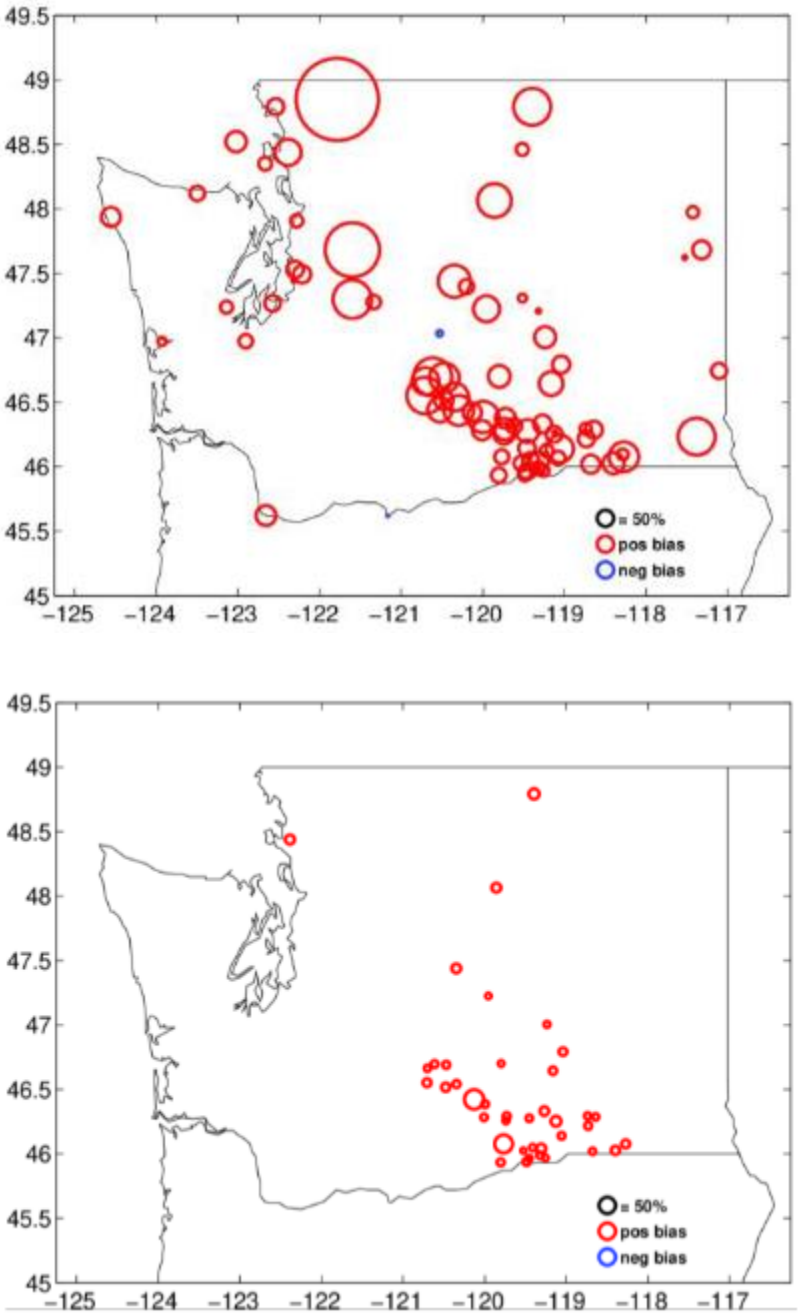

Figure 11: Map of the annual average wind speed (top) and shortwave radiation (bottom) biases for the historical WRF climate dataset. A positive bias indicates that the historical WRF climate values were larger than observations measured at weather stations (modified from Mauger et al., 2021).

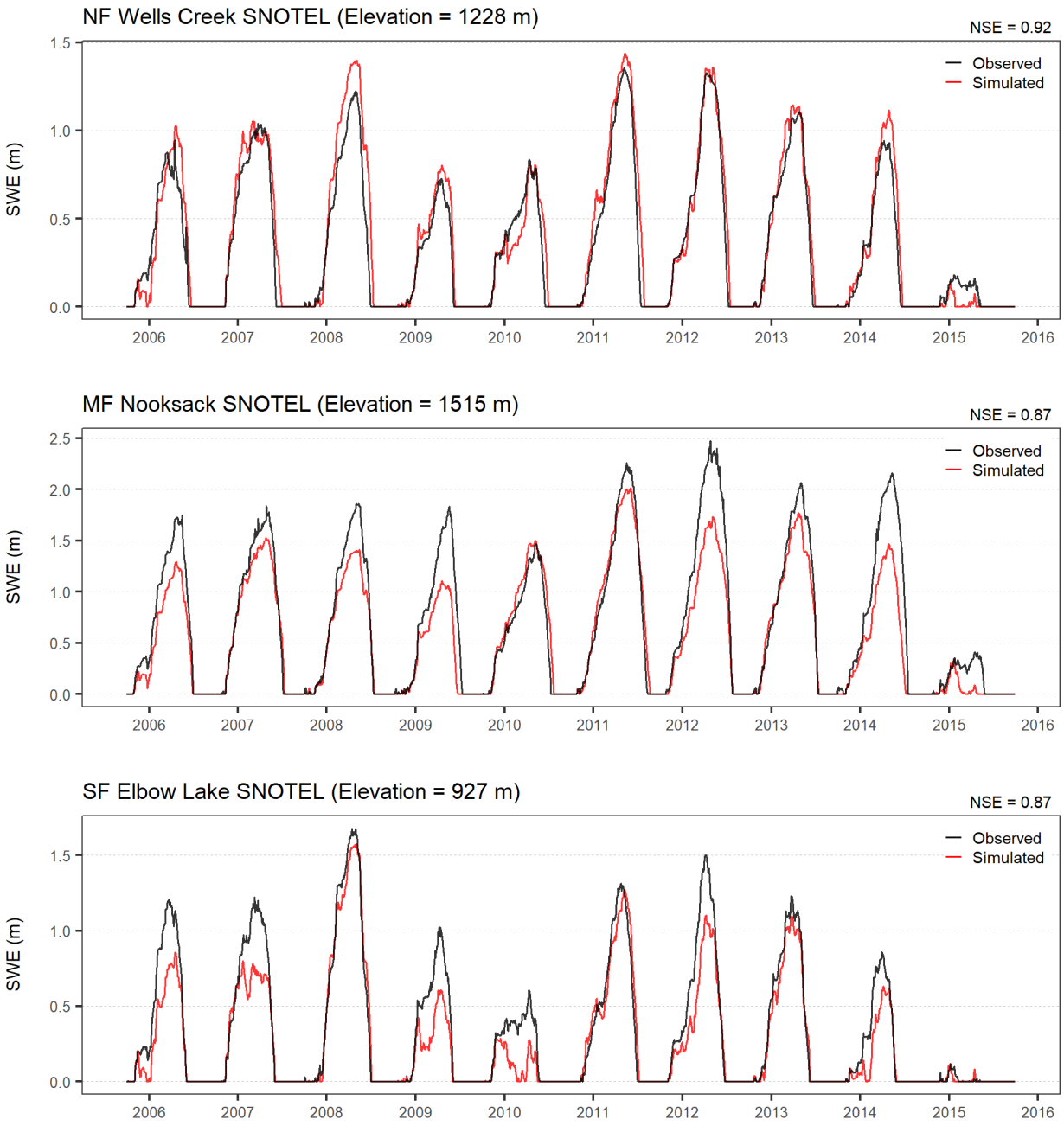

Figure 12: Daily average snow-water equivalent (SWE) calibration results for the North, Middle, and South Fork subbasins. Red lines represent simulated SWE and black lines represent observed SWE measured at SNOTEL sites.

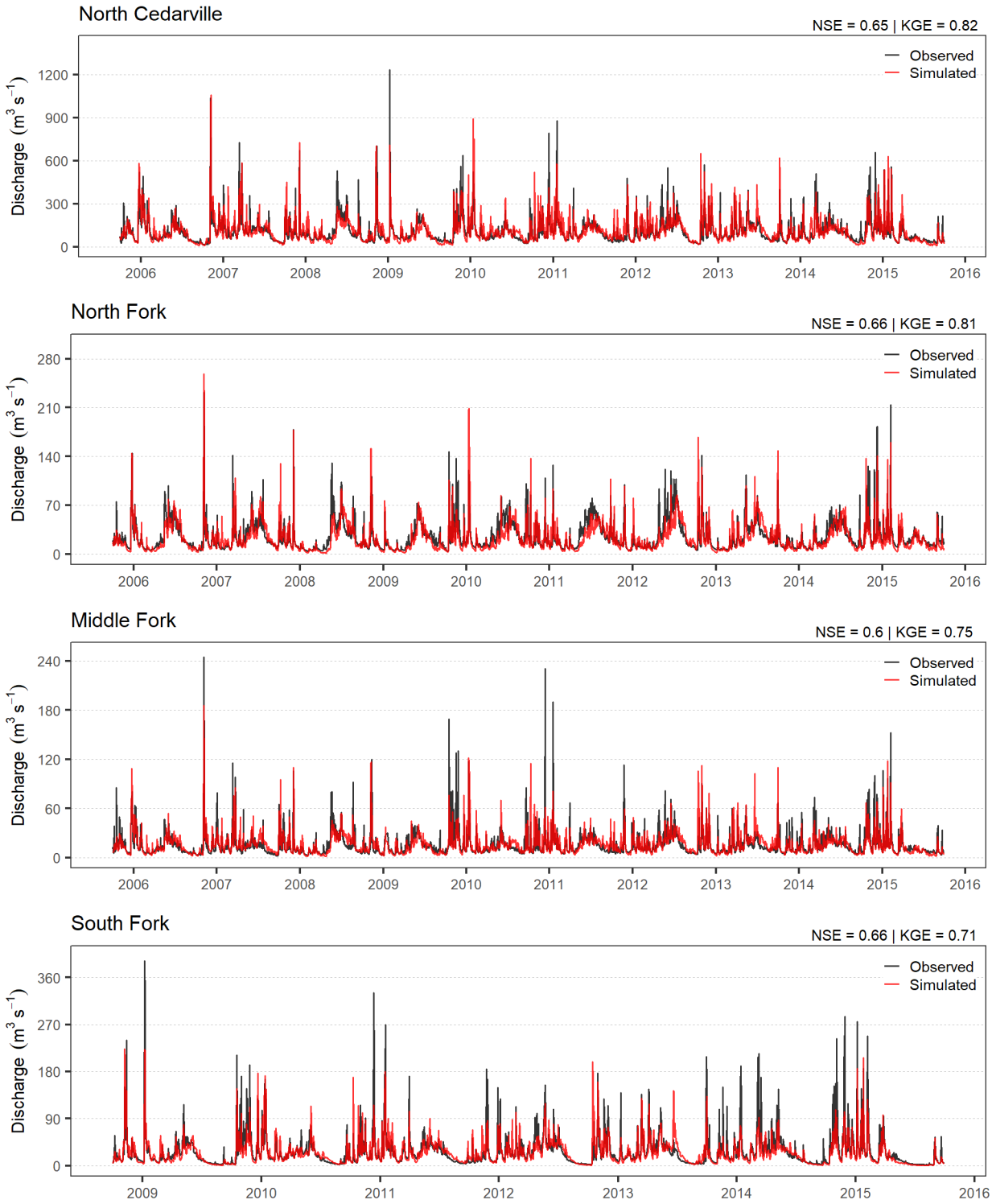

Figure 13: Daily average streamflow calibration results at stream gauges located at North Cedarville and on the North, Middle, and South Forks of the Nooksack River. Red lines represent simulated streamflow and black lines represent observed streamflow measured at USGS stream gauges.

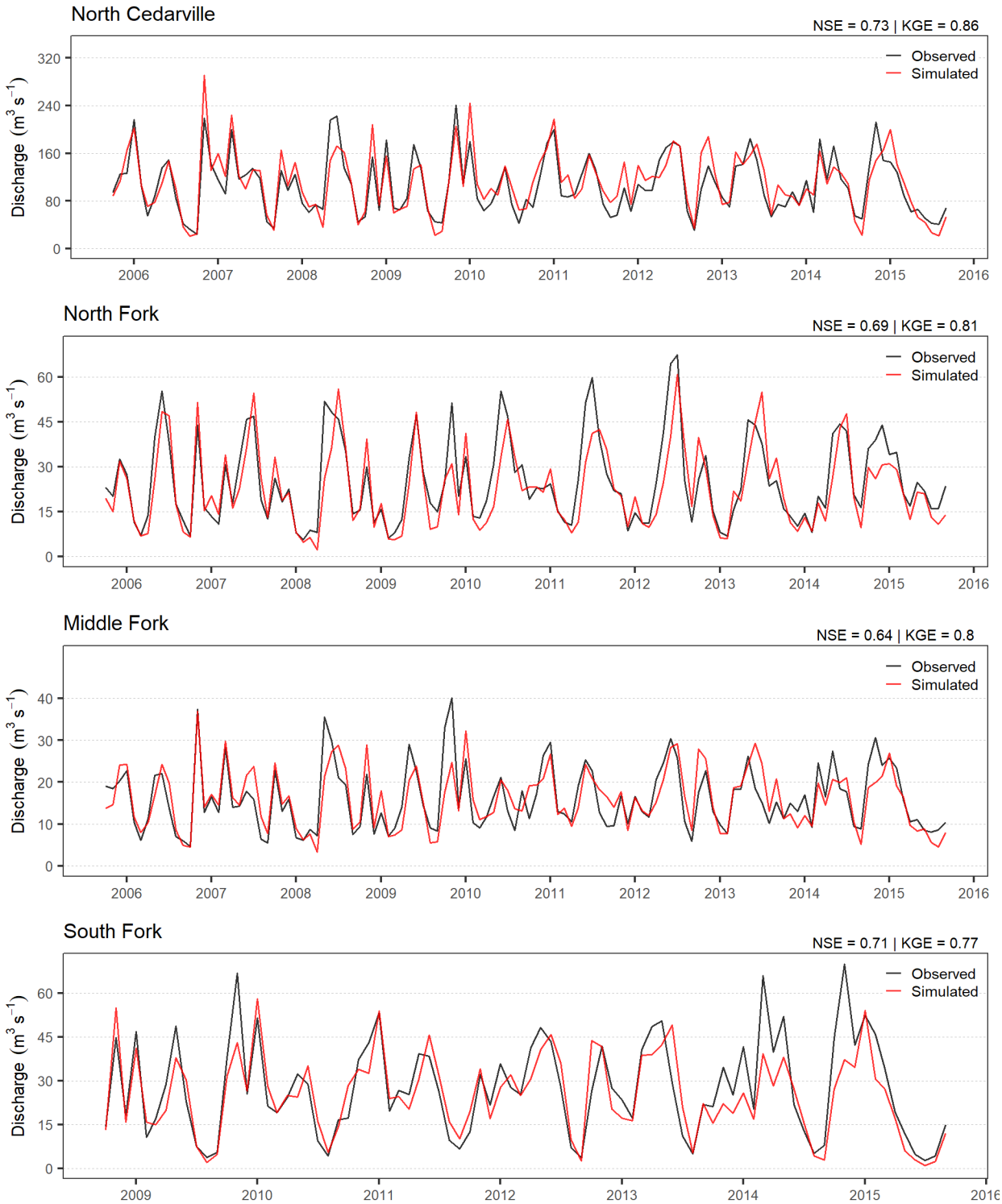

Figure 14: Monthly average streamflow calibration results at stream gauges located at North Cedarville and on the North, Middle, and South Forks of the Nooksack River. Red lines represent simulated streamflow and black lines represent observed streamflow measured at USGS stream gauges.

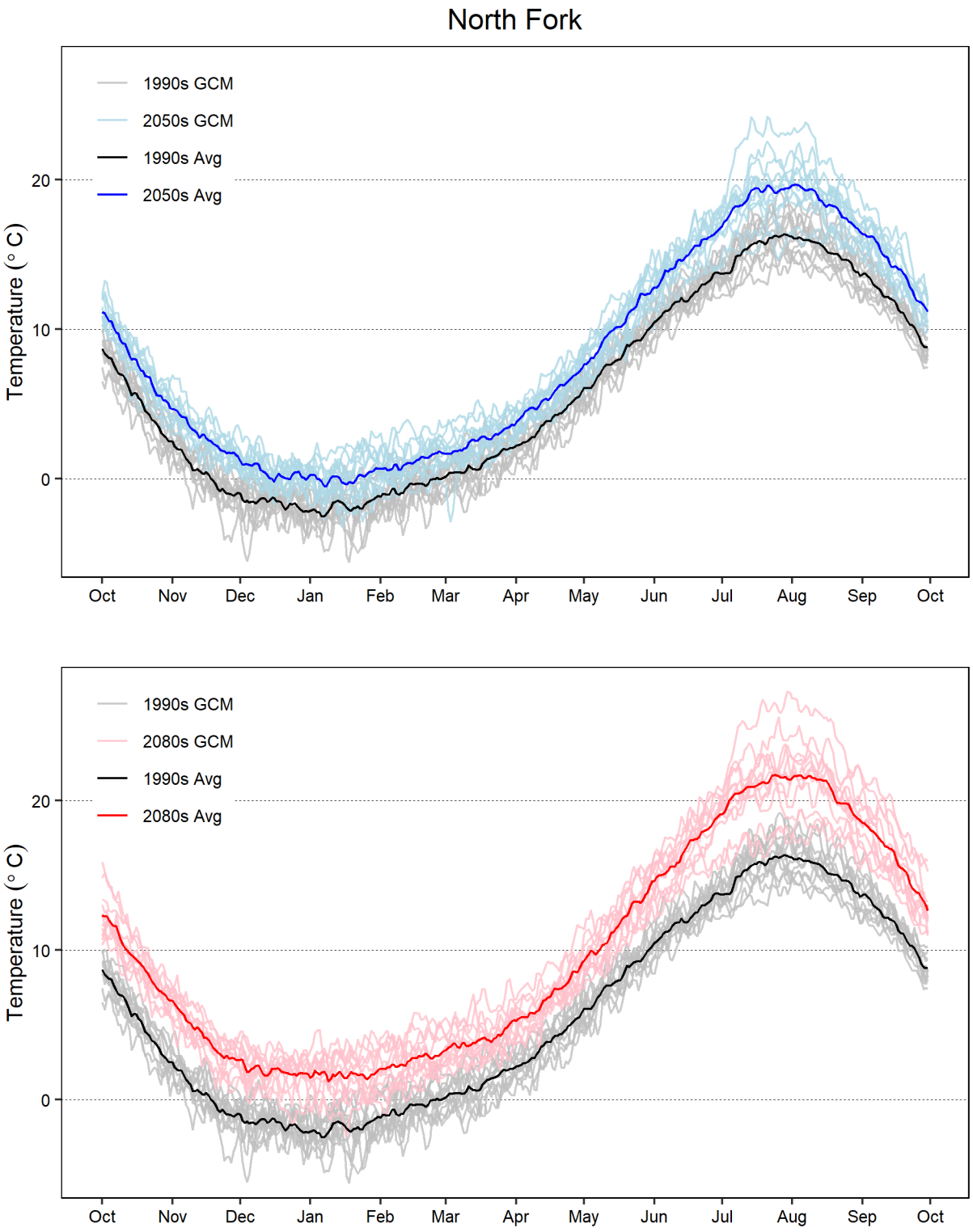

Figure 15: Simulated daily average air temperature in the North Fork subbasin for the 2050s (top) and 2080s (bottom) 30-year normals. Gray, light blue, and light red lines represent 30-year averages for individual GCMs. Black, blue, and red lines represent the ensemble average across all 12 GCMs.

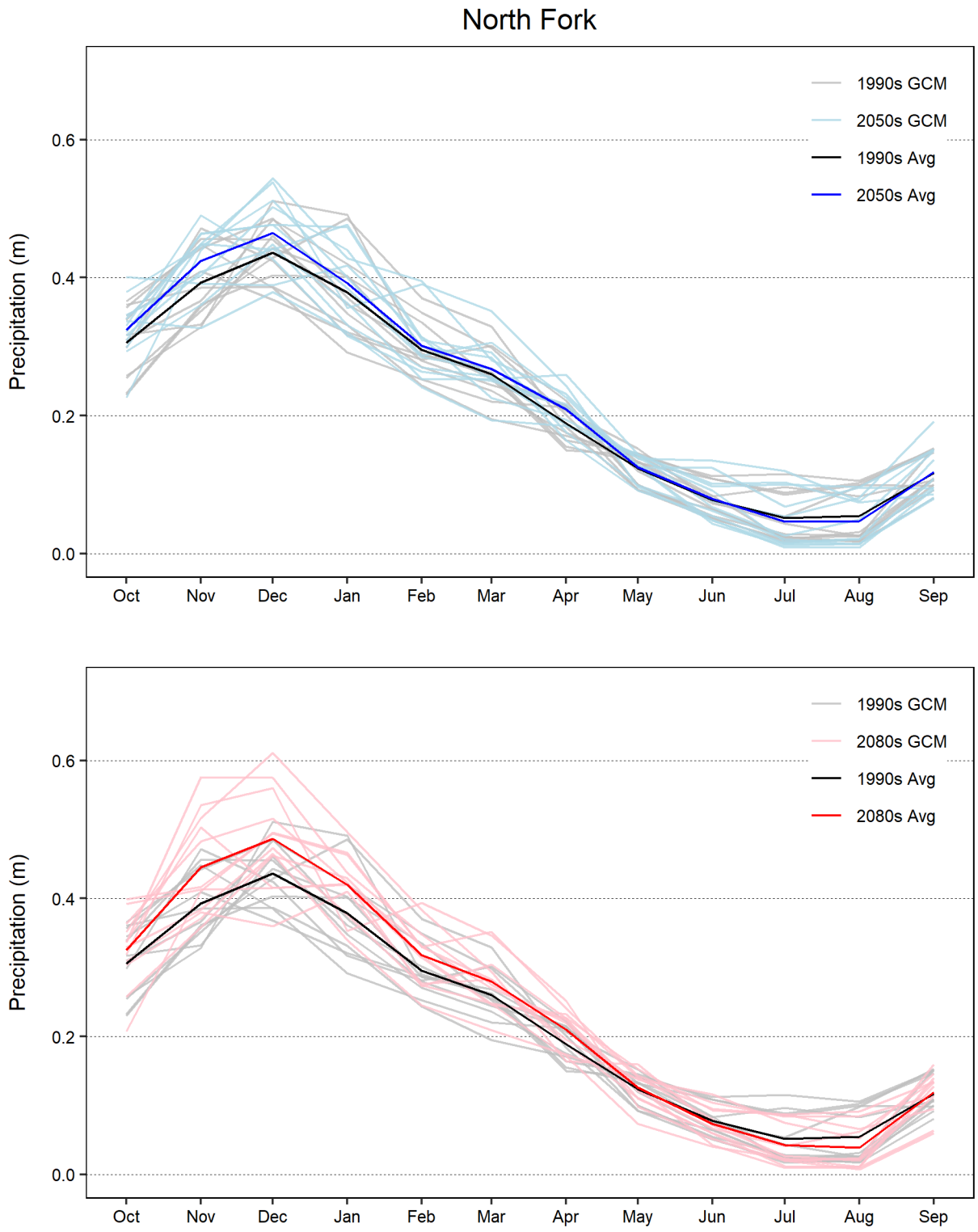

Figure 16: Simulated monthly precipitation in the North Fork subbasin for the 2050s (top) and 2080s (bottom) 30-year normals. Gray, light blue, and light red lines represent 30-year averages for individual GCMs. Black, blue, and red lines represent the ensemble average across all 12 GCMs.

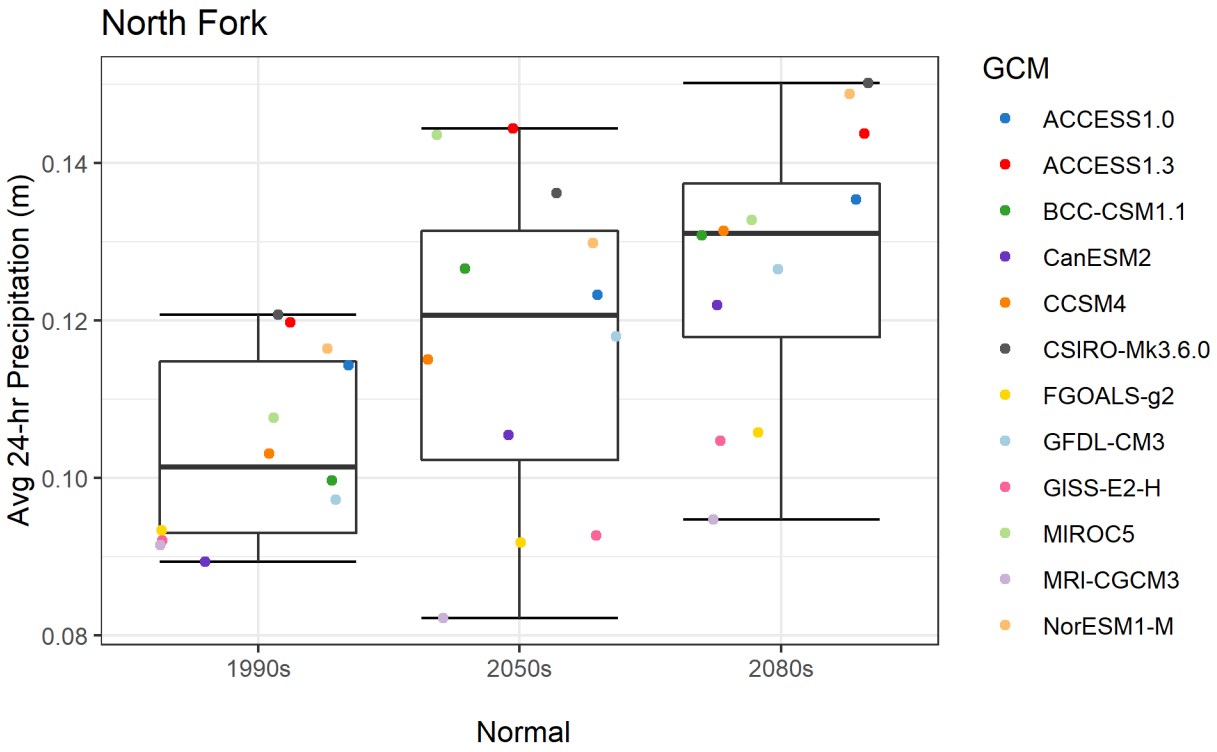

Figure 17: Simulated average annual maximum 24-hour precipitation magnitude in the North Fork subbasin for the 1990s, 2050s, and 2080s 30-year normals. Points represent the average annual maximum precipitation magnitude over a 30-year period for each GCM.

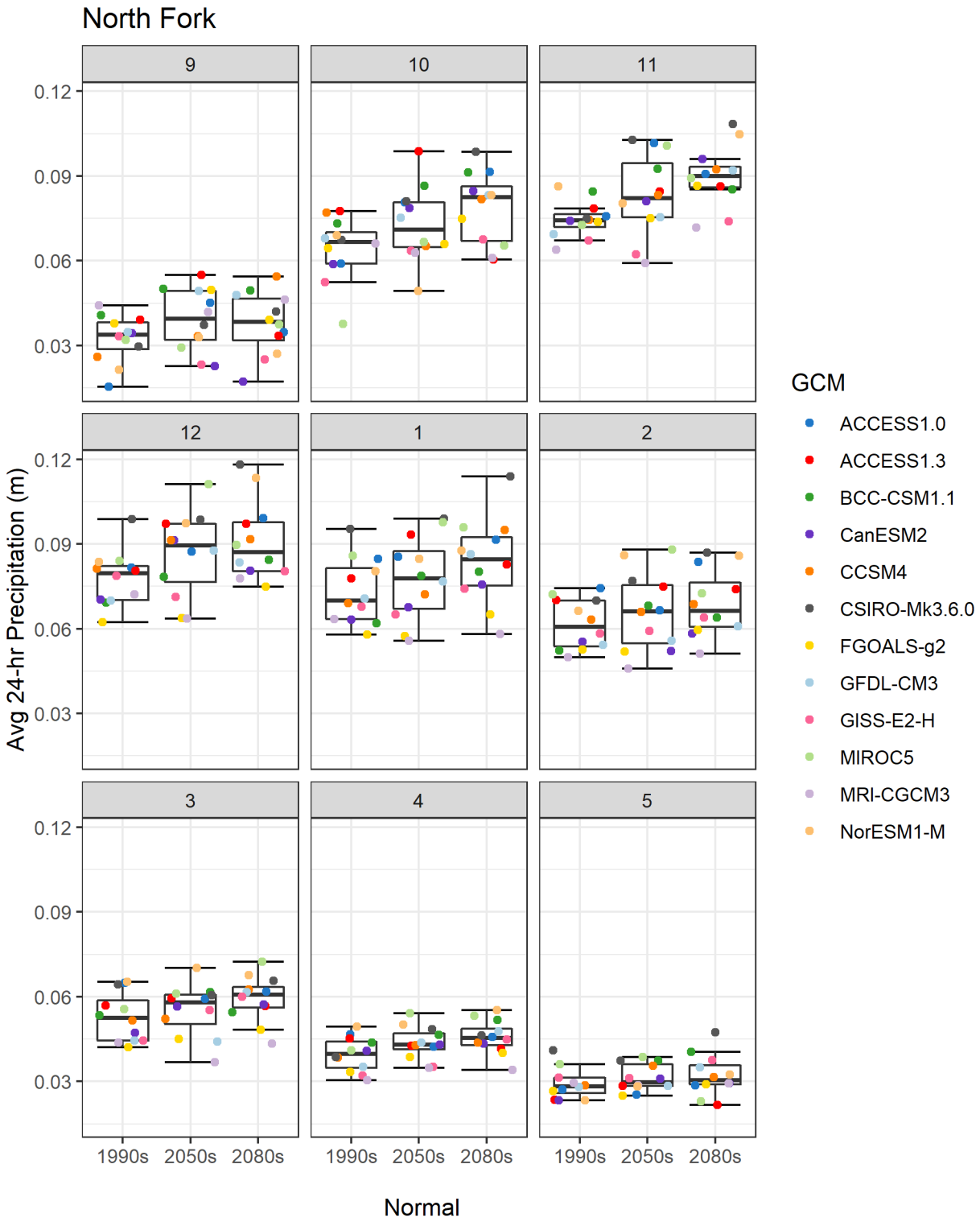

Figure 18: Simulated average monthly maximum 24-hour precipitation magnitude in the North Fork subbasin for the 1990s, 2050s, and 2080s 30-year normals. Points represent the average monthly maximum precipitation magnitude over a 30-year period for each GCM. June (6), July (7), and August (8) are excluded.

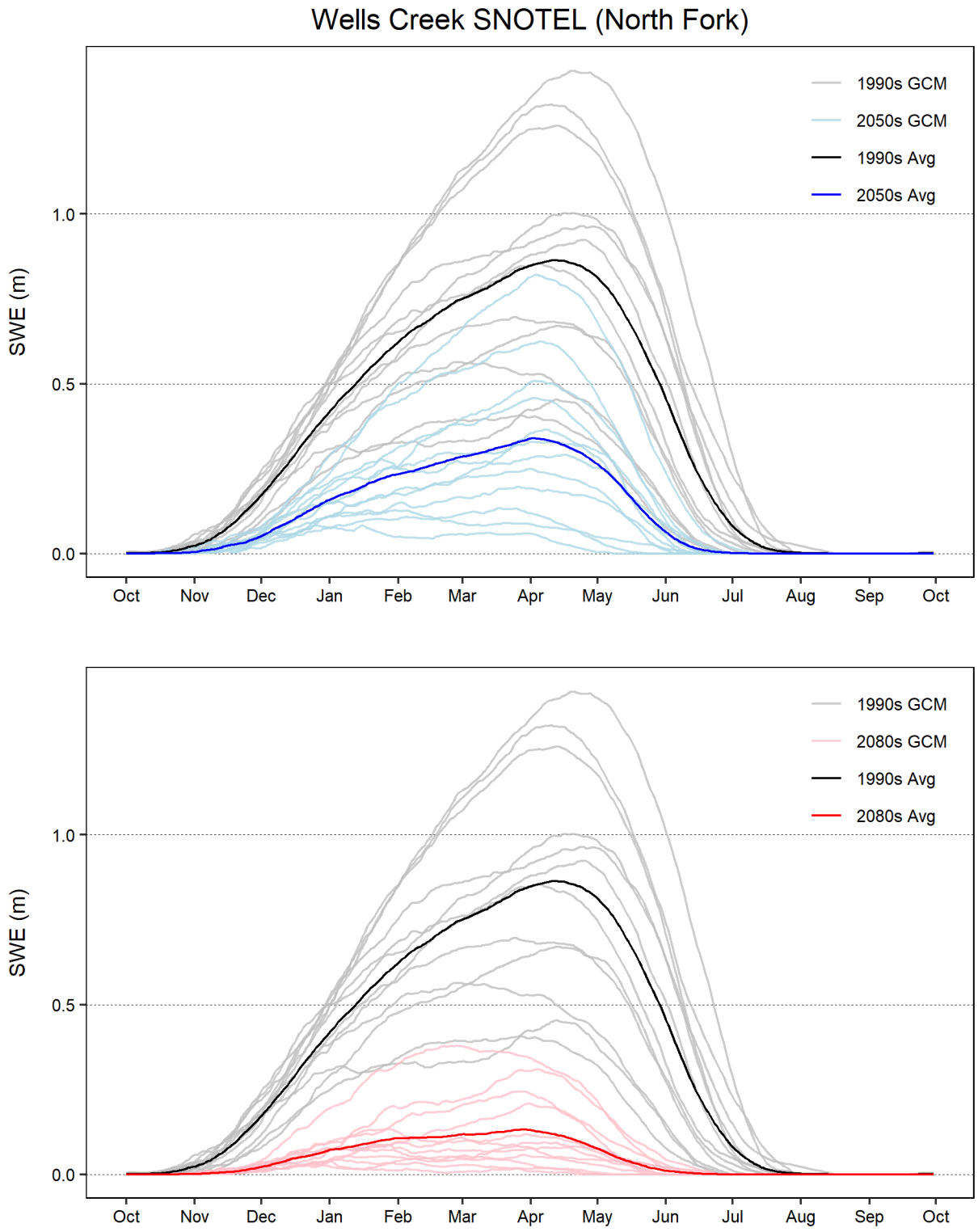

Figure 19: Simulated daily average snow-water equivalent (SWE) at the Wells Creek SNOTEL (1228 m/4030 ft) site in the North Fork for the 2050s (top) and 2080s (bottom) 30-year normals. Gray, light blue, and light red lines represent 30-year averages for individual GCMs. Black, blue, and red lines represent the ensemble average across all 12 GCMs.

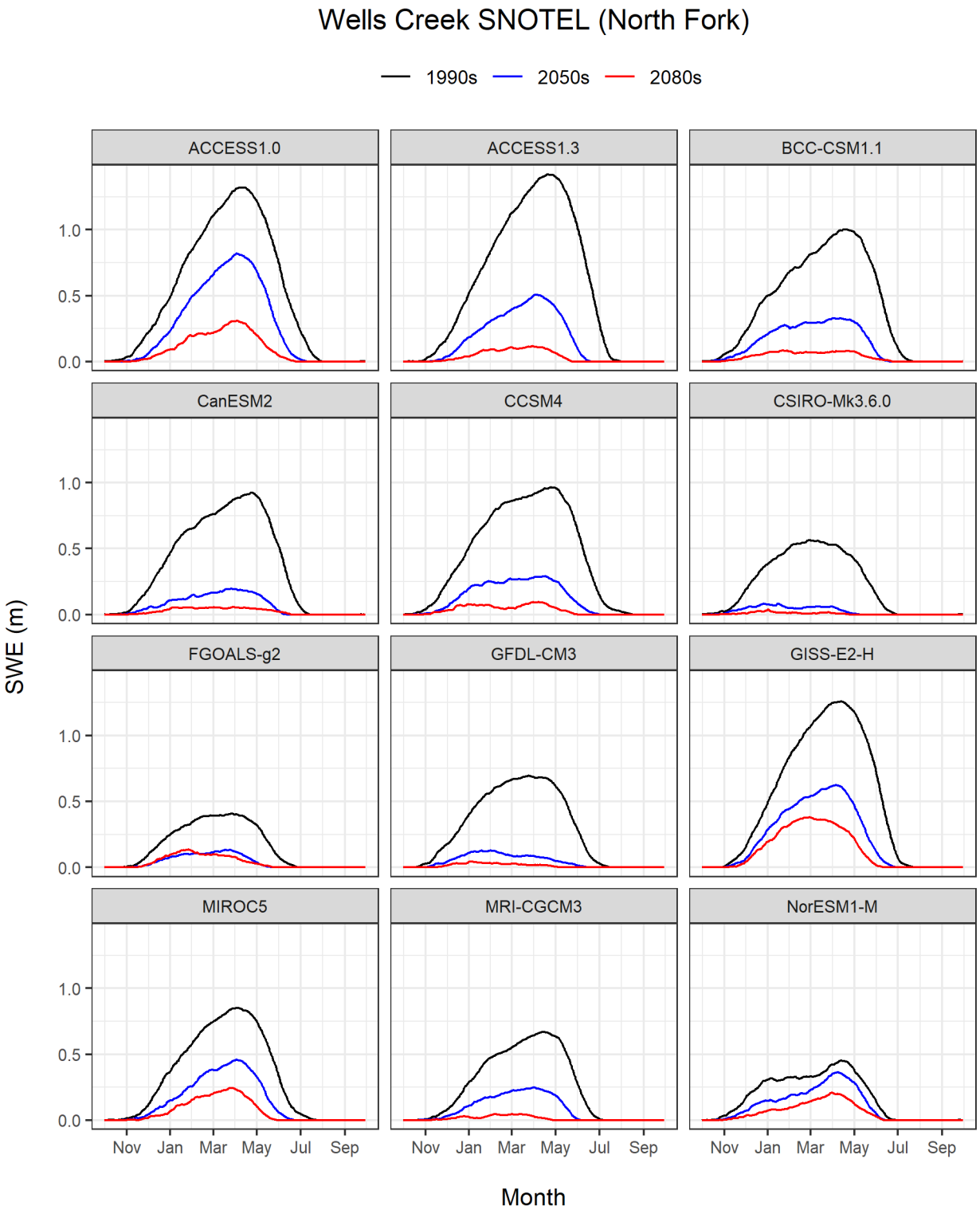

Figure 20: Simulated daily average snow-water equivalent (SWE) at the Wells Creek SNOTEL (1228 m/4030 ft) site in the North Fork for each GCM and 30-year climate normal.

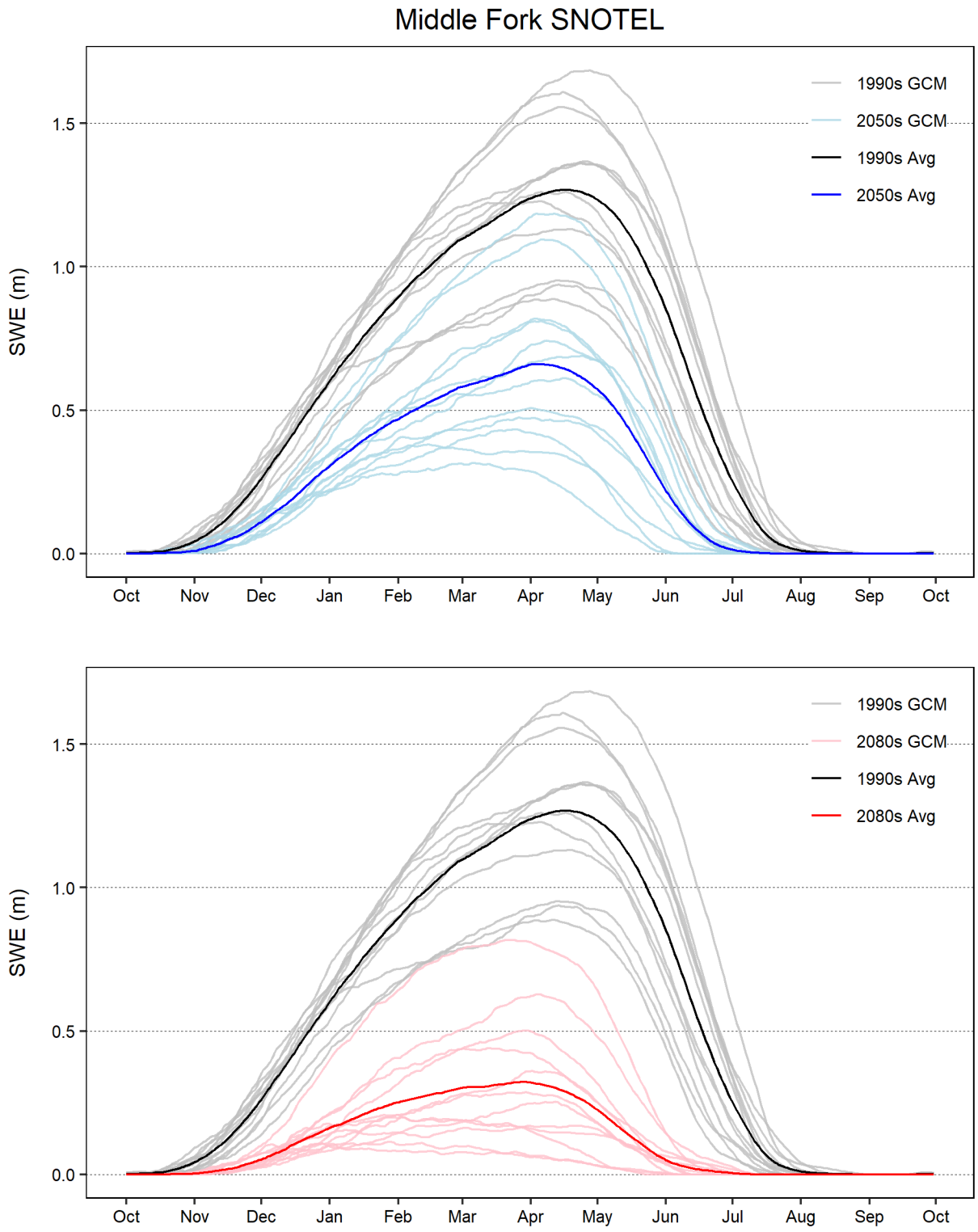

Figure 21: Simulated daily average snow-water equivalent (SWE) at the MF Nooksack SNOTEL (1515 m/4970 ft) site in the Middle Fork for the 2050s (top) and 2080s (bottom) 30-year normals. Gray, light blue, and light red lines represent 30-year averages for individual GCMs. Black, blue, and red lines represent the ensemble average across all 12 GCMs.

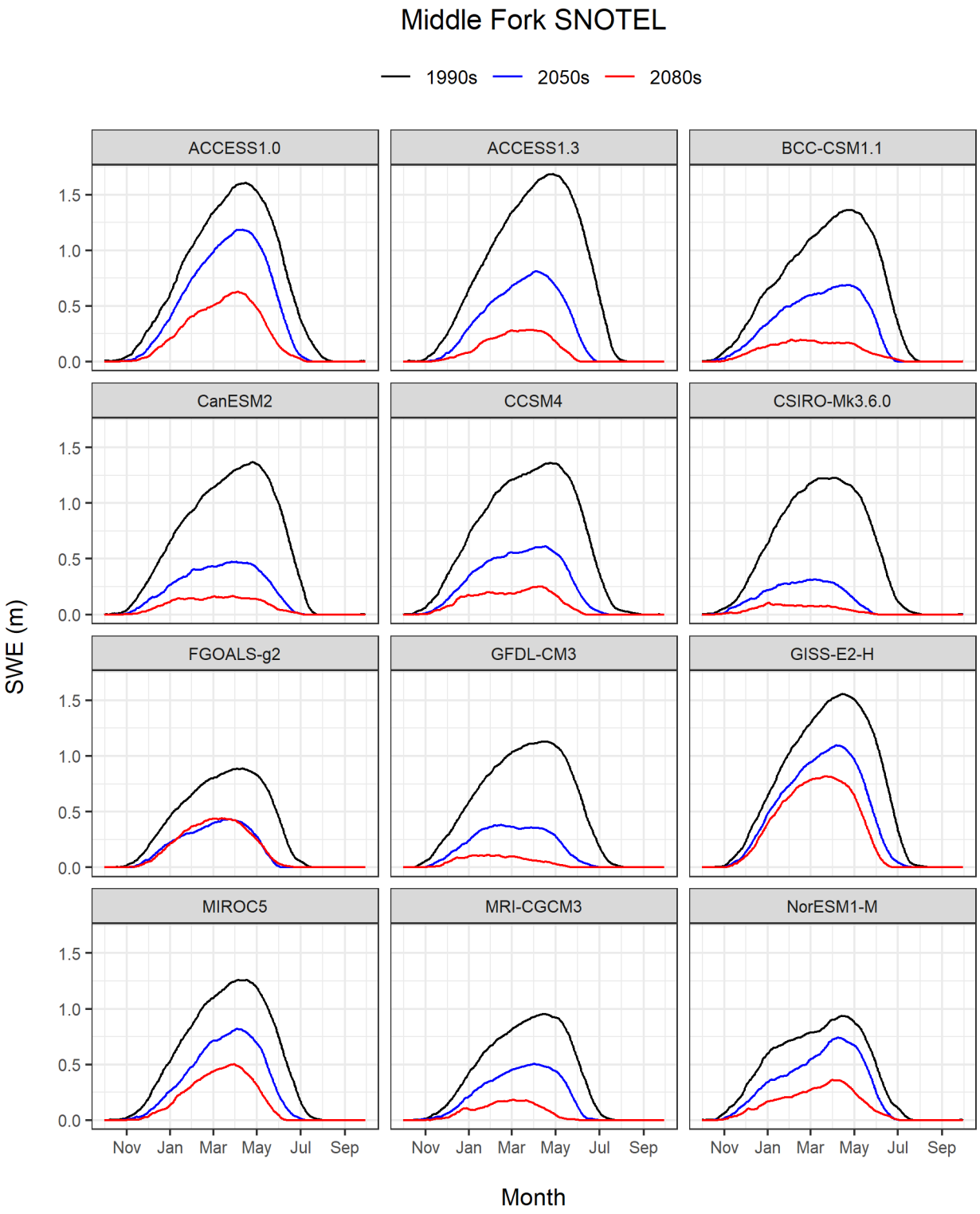

Figure 22: Simulated daily average snow-water equivalent (SWE) at the Middle Fork SNOTEL (1515 m/4970 ft) site for each GCM and 30-year climate normal.

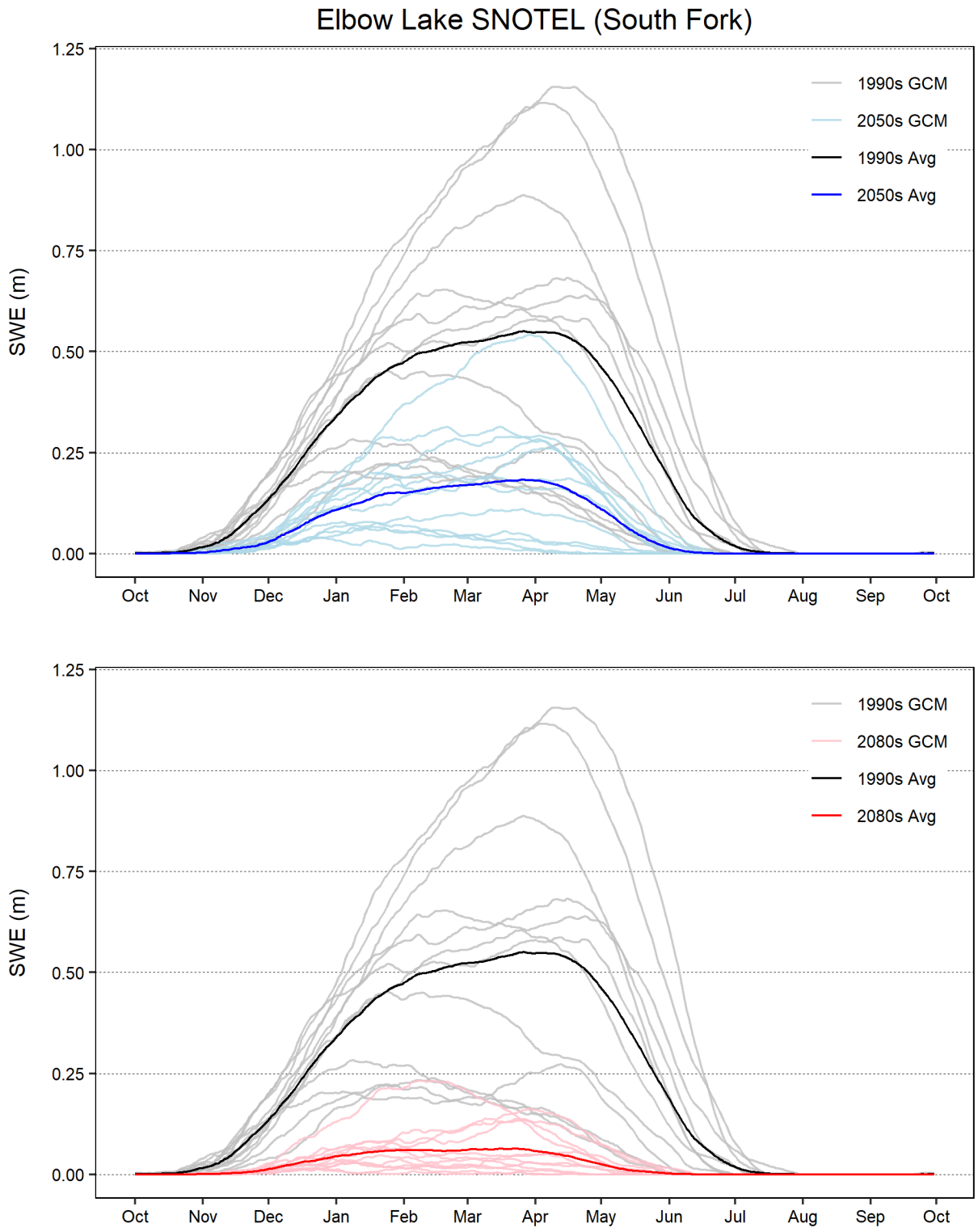

Figure 23: Simulated daily average snow-water equivalent (SWE) at the Elbow Lake SNOTEL (927 m/3040 ft) site in the South Fork for the 2050s (top) and 2080s (bottom) 30-year normals. Gray, light blue, and light red lines represent 30-year averages for individual GCMs. Black, blue, and red lines represent the ensemble average across all 12 GCMs.

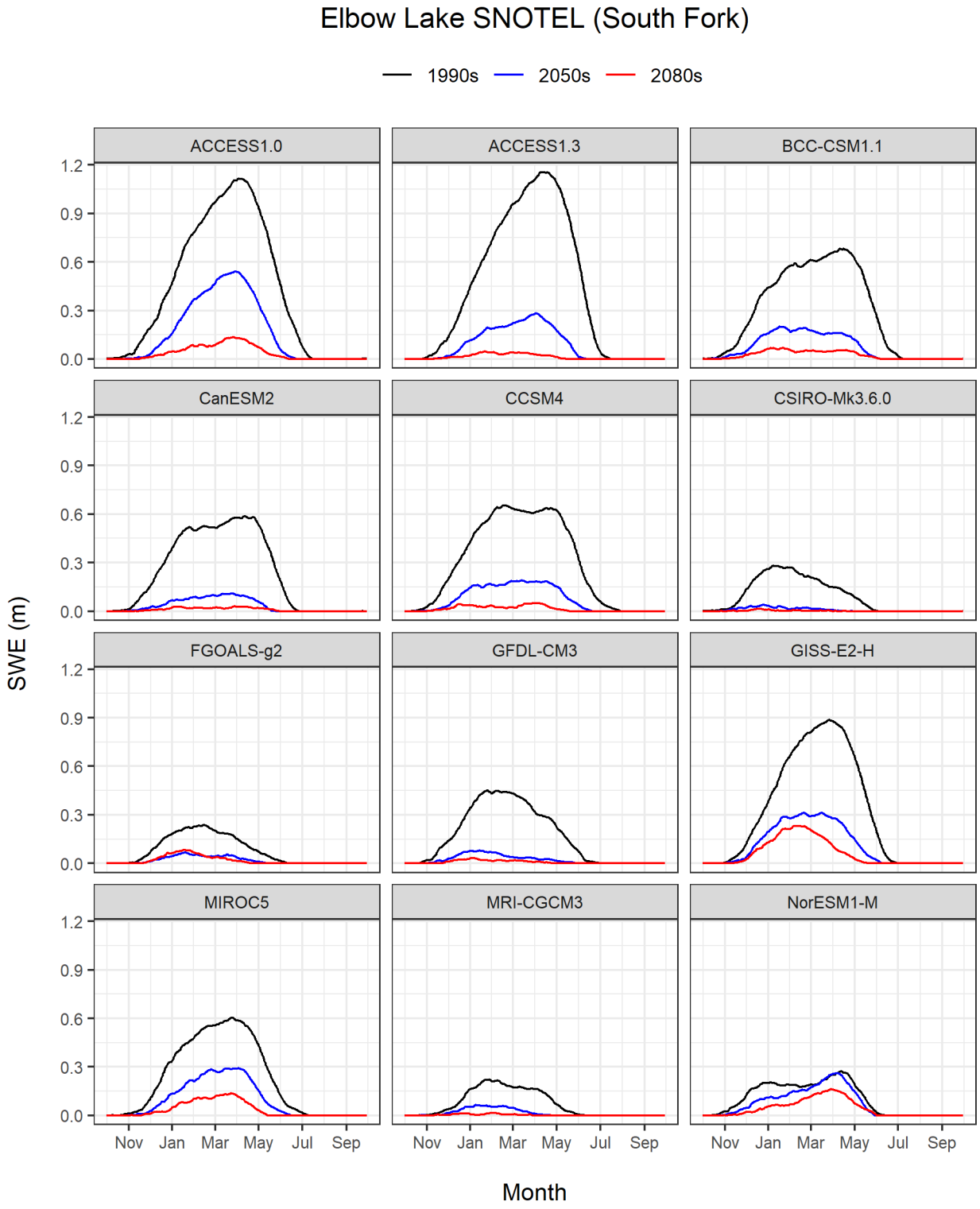

Figure 24: Simulated daily average snow-water equivalent (SWE) at the Elbow Lake SNOTEL (927 m/3040 ft) site in the South Fork for each GCM and 30-year climate normal.

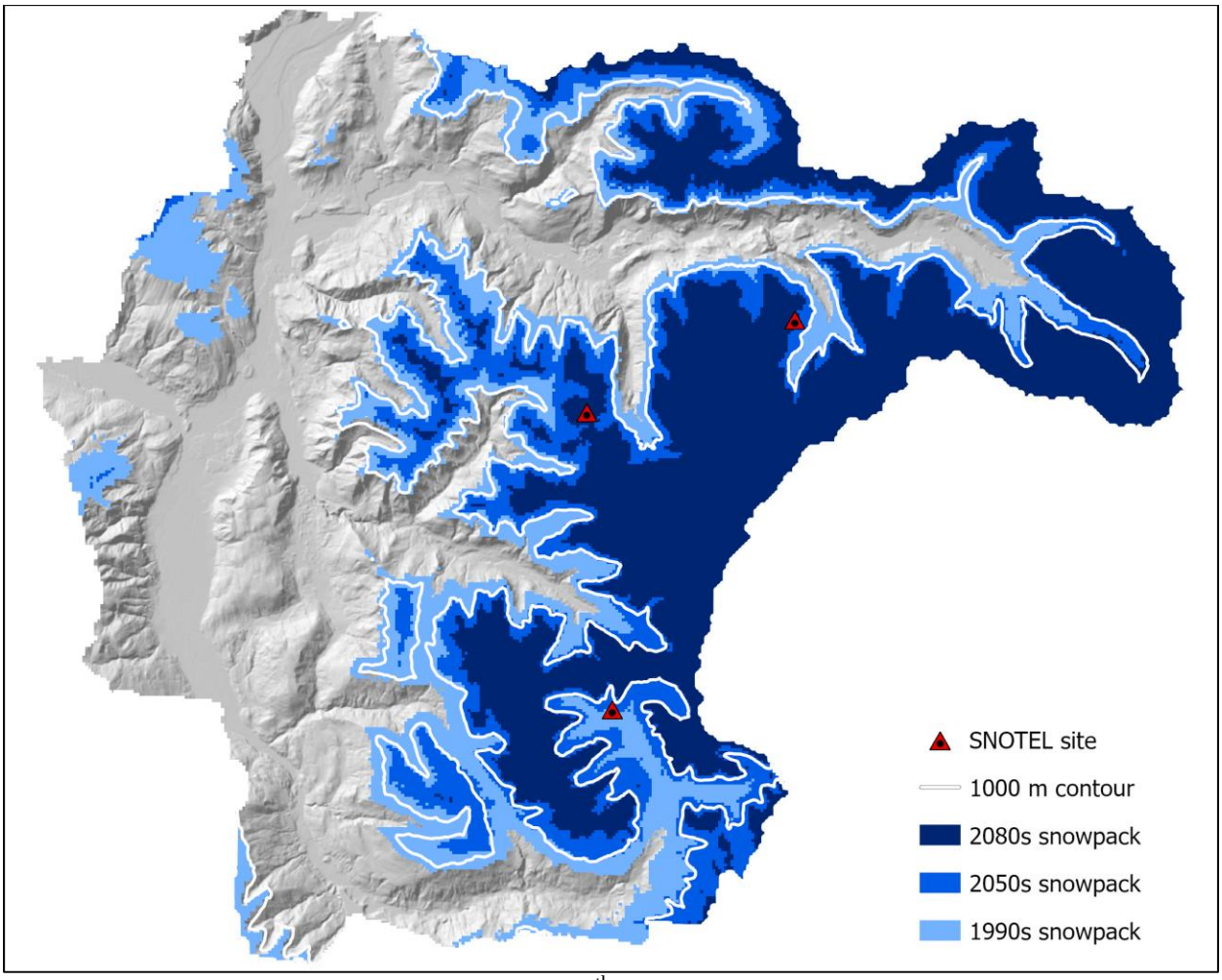

Figure 25: Simulated 30-year average April 15th snowpack extent across all 12 GCMs for each climate normal. Snowpack is characterized by pixels with a 30-year average SWE value of 0.1 m or greater.

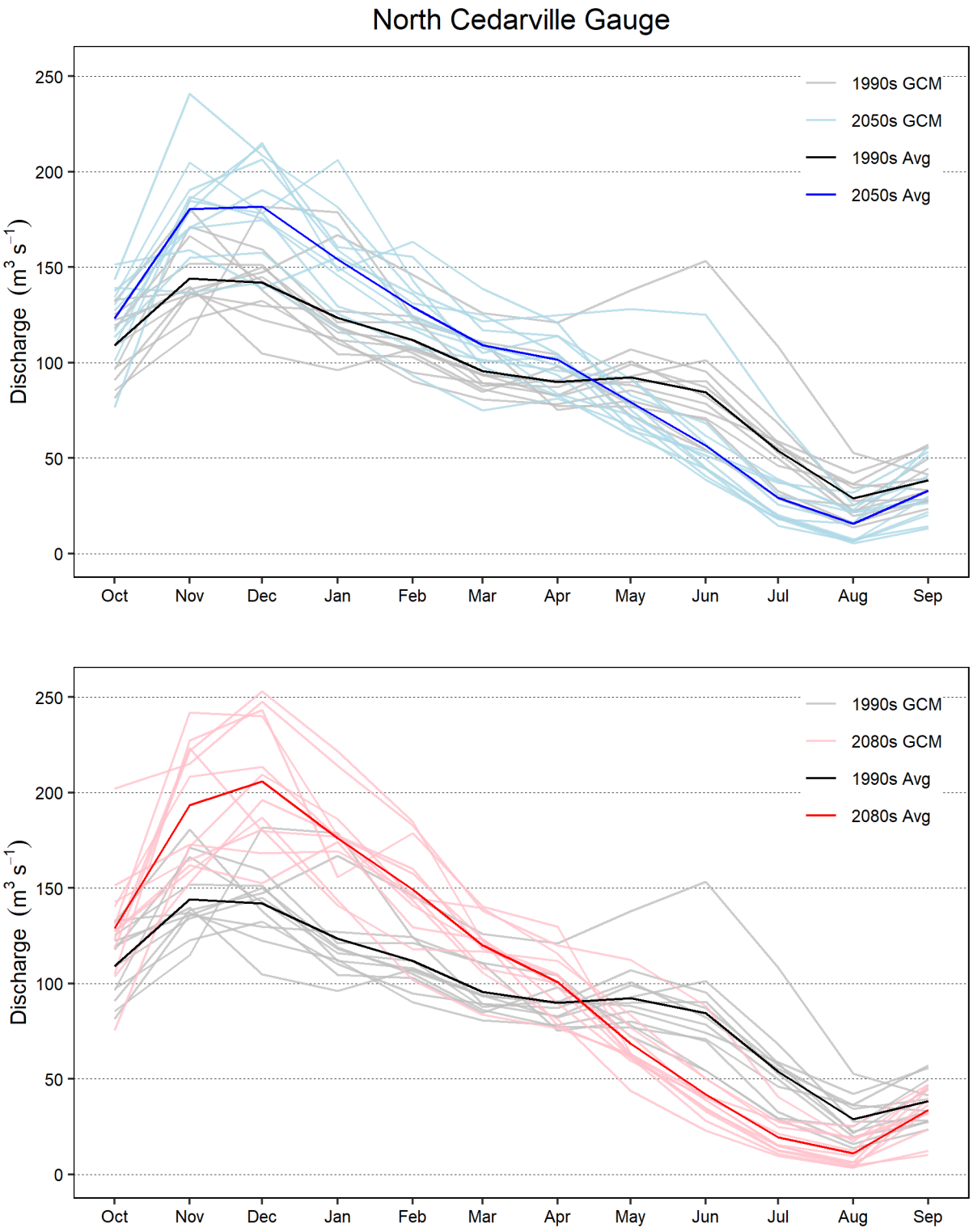

Figure 26: Simulated monthly average streamflow at the North Cedarville gauge of the Nooksack River for the 2050s (top) and 2080s (bottom) 30-year normals. Gray, light blue, and light red lines represent 30-year averages for individual GCMs. Black, blue, and red lines represent the ensemble average across all 12 GCMs.

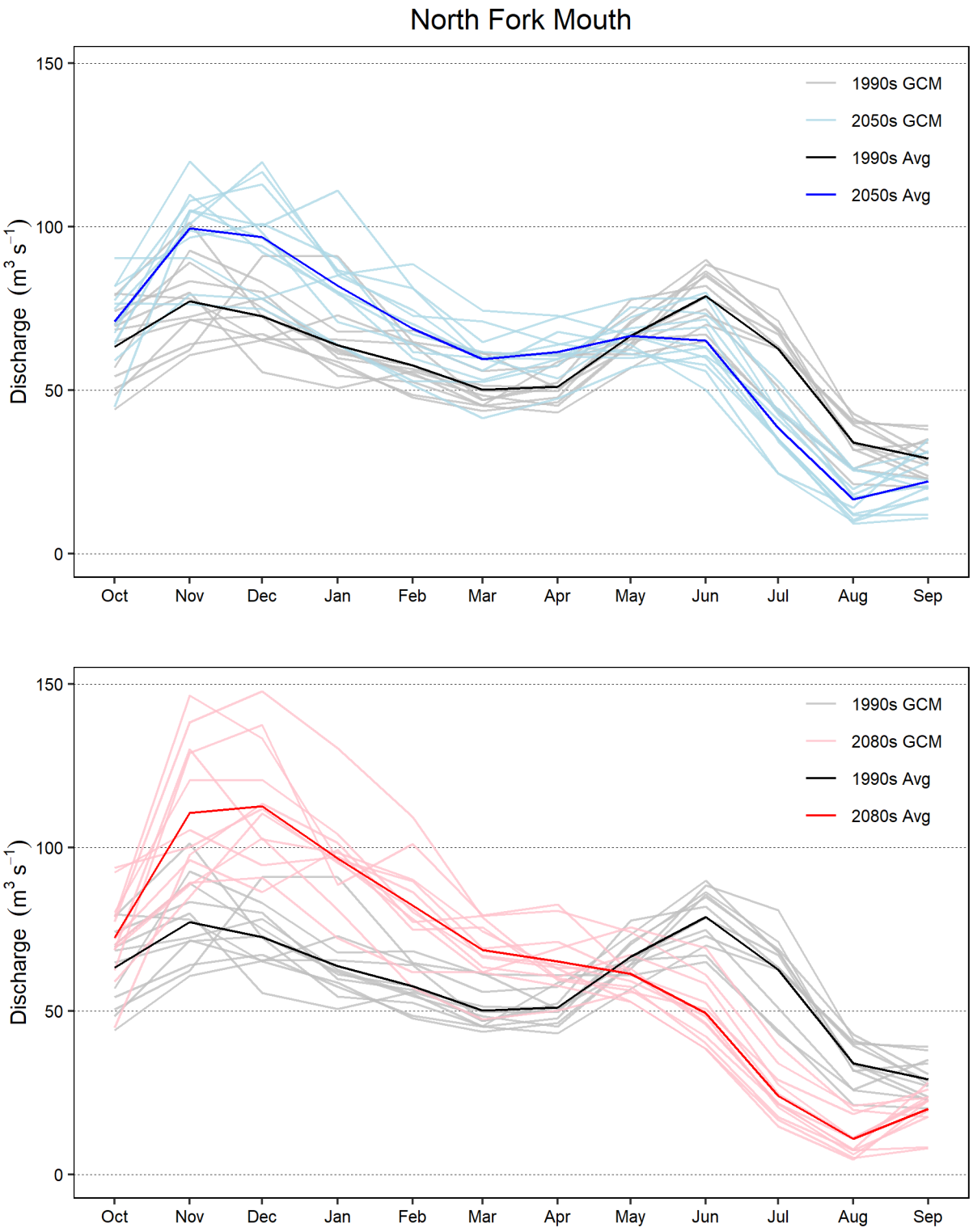

Figure 27: Simulated monthly average streamflow at the mouth of the North Fork Nooksack River for the 2050s (top) and 2080s (bottom) 30-year normals. Gray, light blue, and light red lines represent 30-year averages for individual GCMs. Black, blue, and red lines represent the ensemble average across all 12 GCMs.

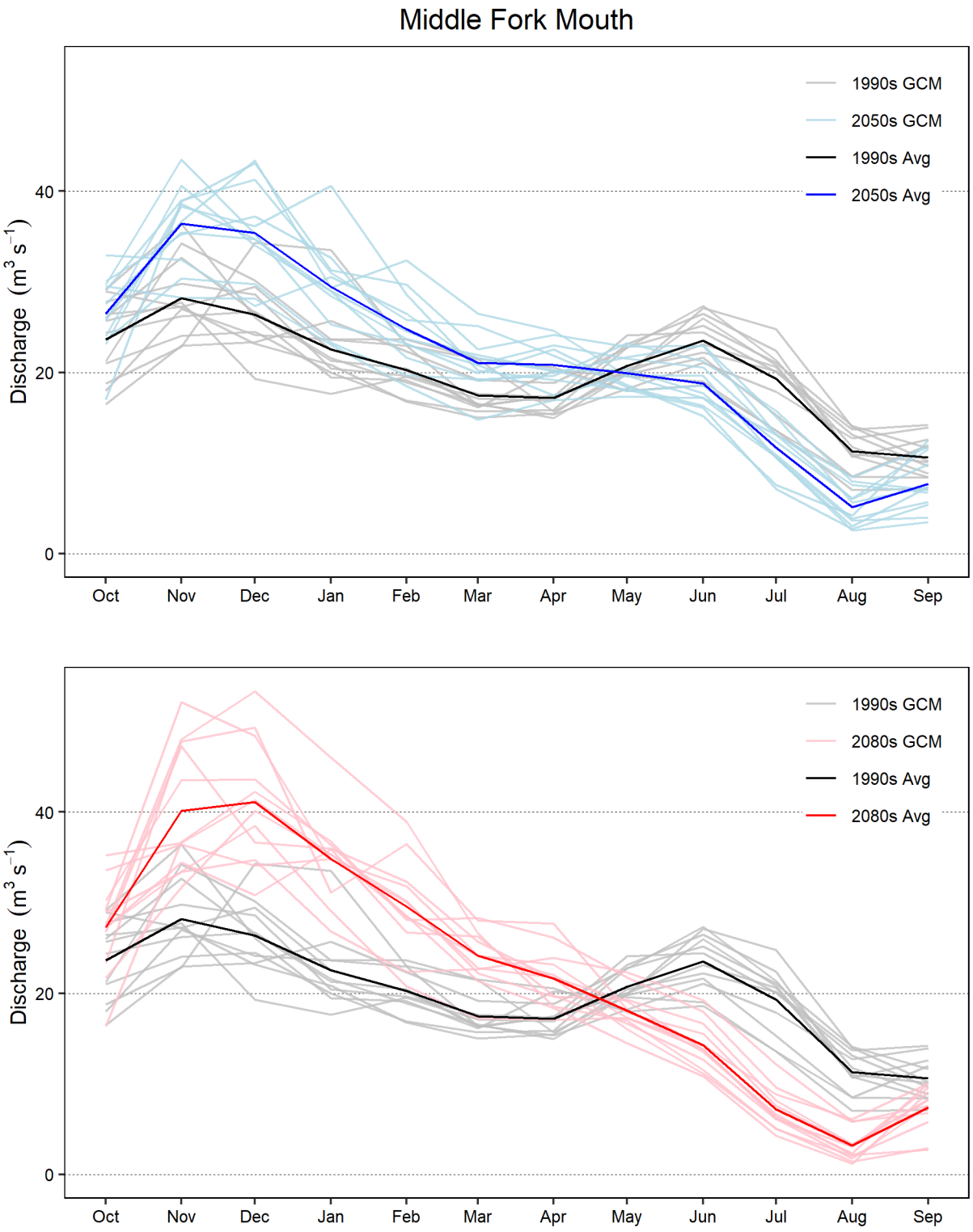

Figure 28: Simulated monthly average streamflow at the mouth of the Middle Fork Nooksack River for the 2050s (top) and 2080s (bottom) 30-year normals. Gray, light blue, and light red lines represent 30-year averages for individual GCMs. Black, blue, and red lines represent the ensemble average across all 12 GCMs.

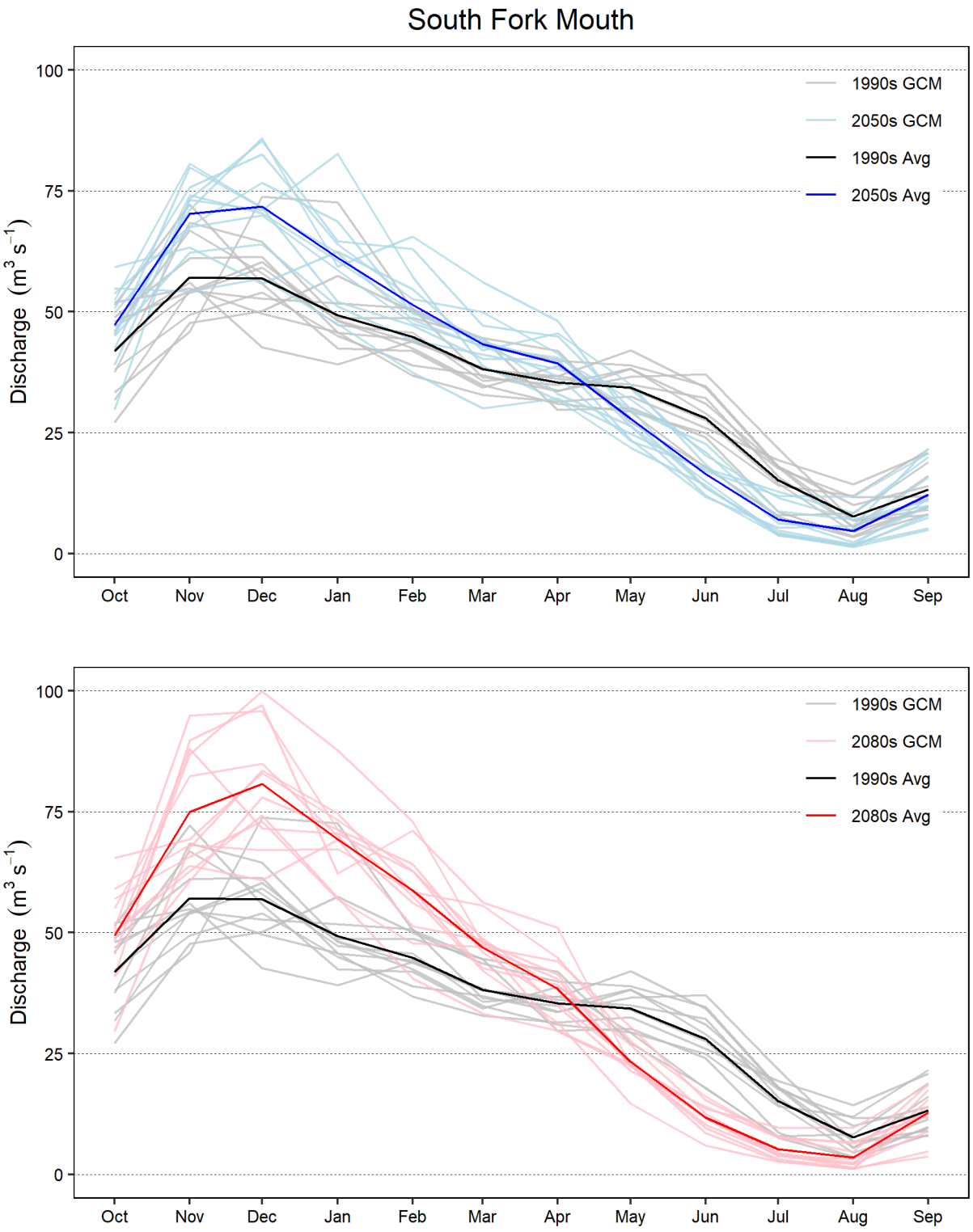

Figure 29: Simulated monthly average streamflow at the mouth of the South Fork Nooksack River for the 2050s (top) and 2080s (bottom) 30-year normals. Gray, light blue, and light red lines represent 30-year averages for individual GCMs. Black, blue, and red lines represent the ensemble average across all 12 GCMs.

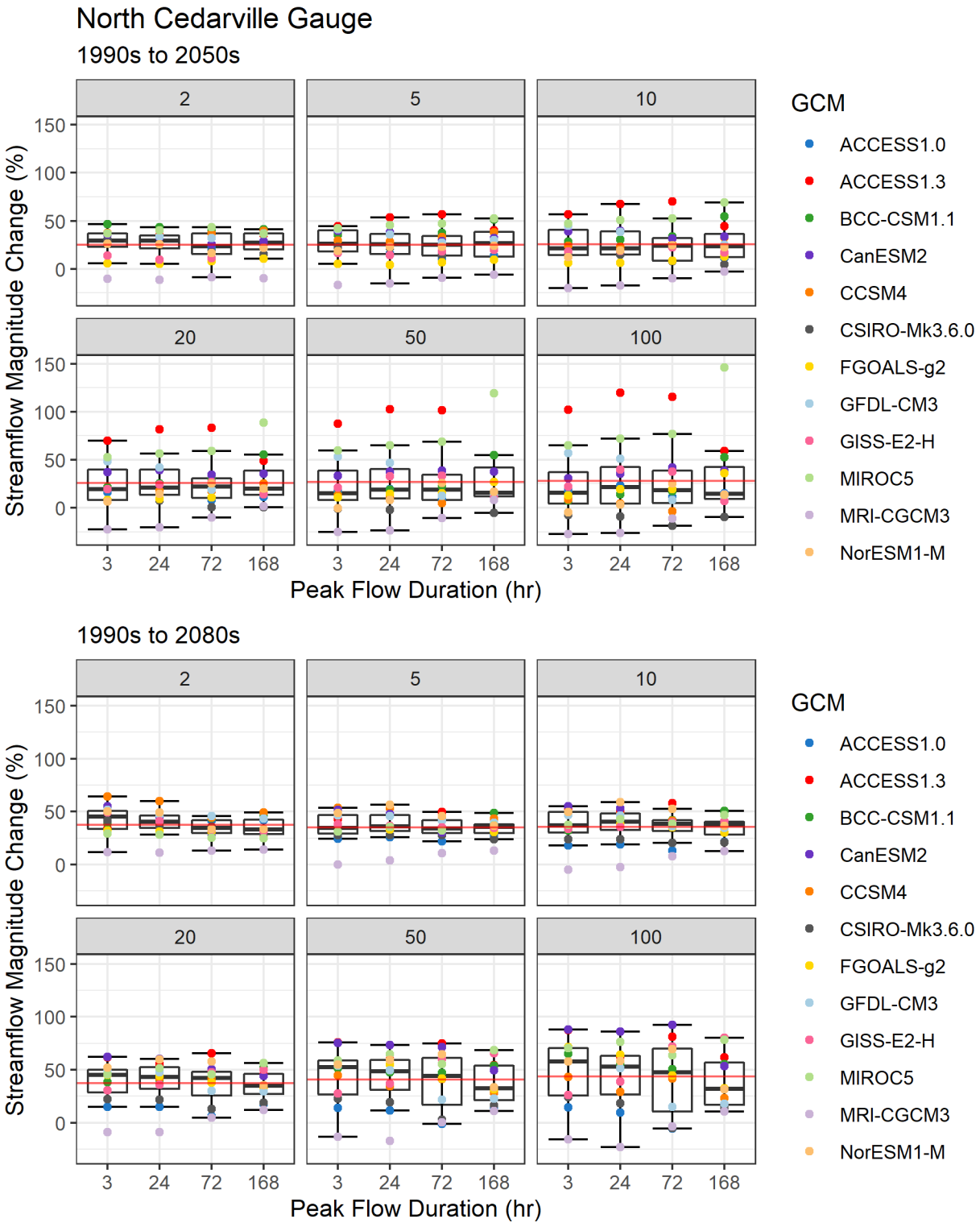

Figure 30: Peak flow magnitude change from the 1990s to 2050s (top) and 1990s to 2080s (bottom) for select return periods (2, 5, 10, 20, 50, and 100-year) at the North Cedarville gauge of the Nooksack River. The solid red line is the average magnitude change for each return period across all GCMs and flow durations.

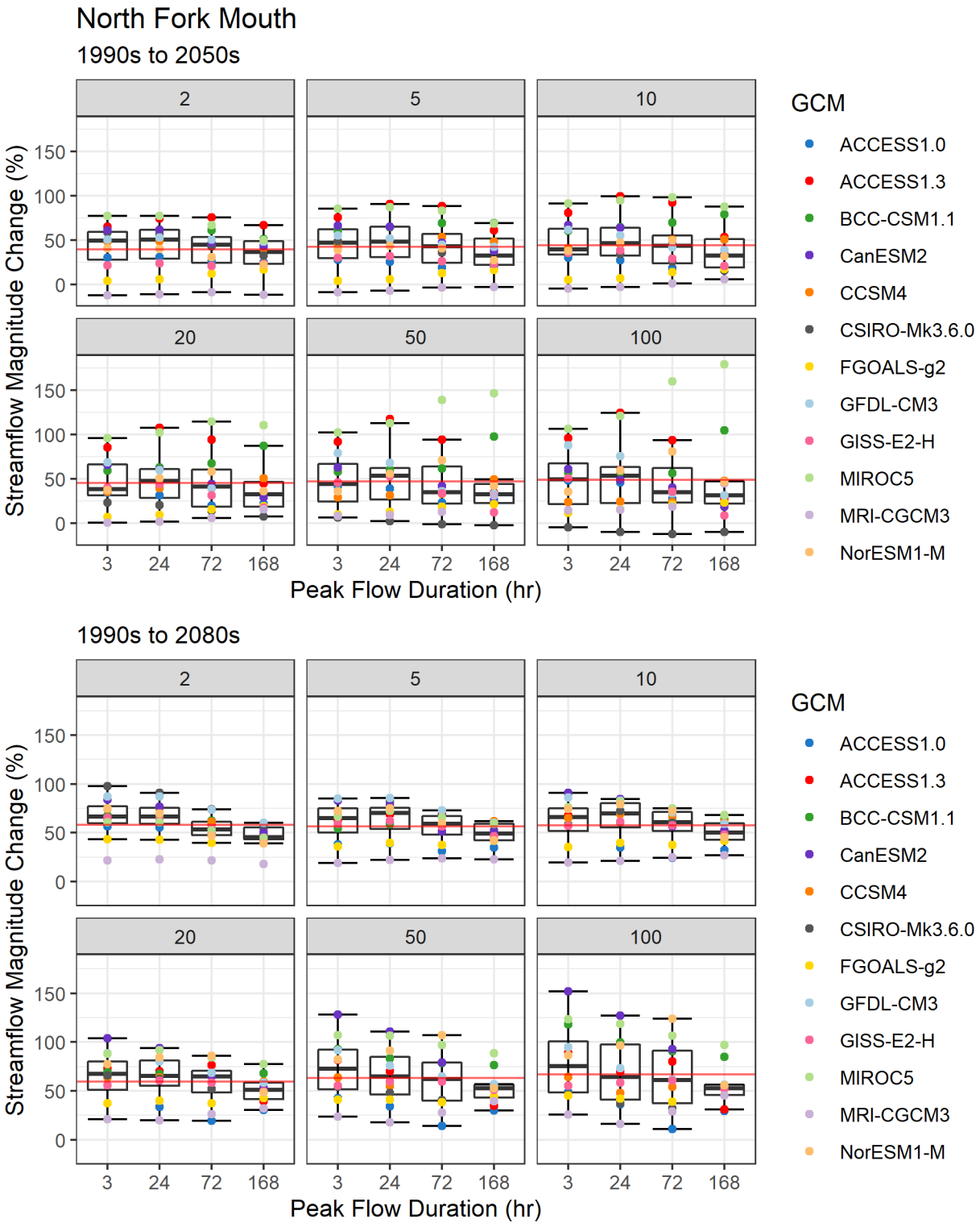

Figure 31: Peak flow magnitude change from the 1990s to 2050s (top) and 1990s to 2080s (bottom) for select return periods (2, 5, 10, 20, 50, and 100-year) at the mouth of the North Fork Nooksack River. The solid red line is the average magnitude change for each return period across all GCMs and flow durations.

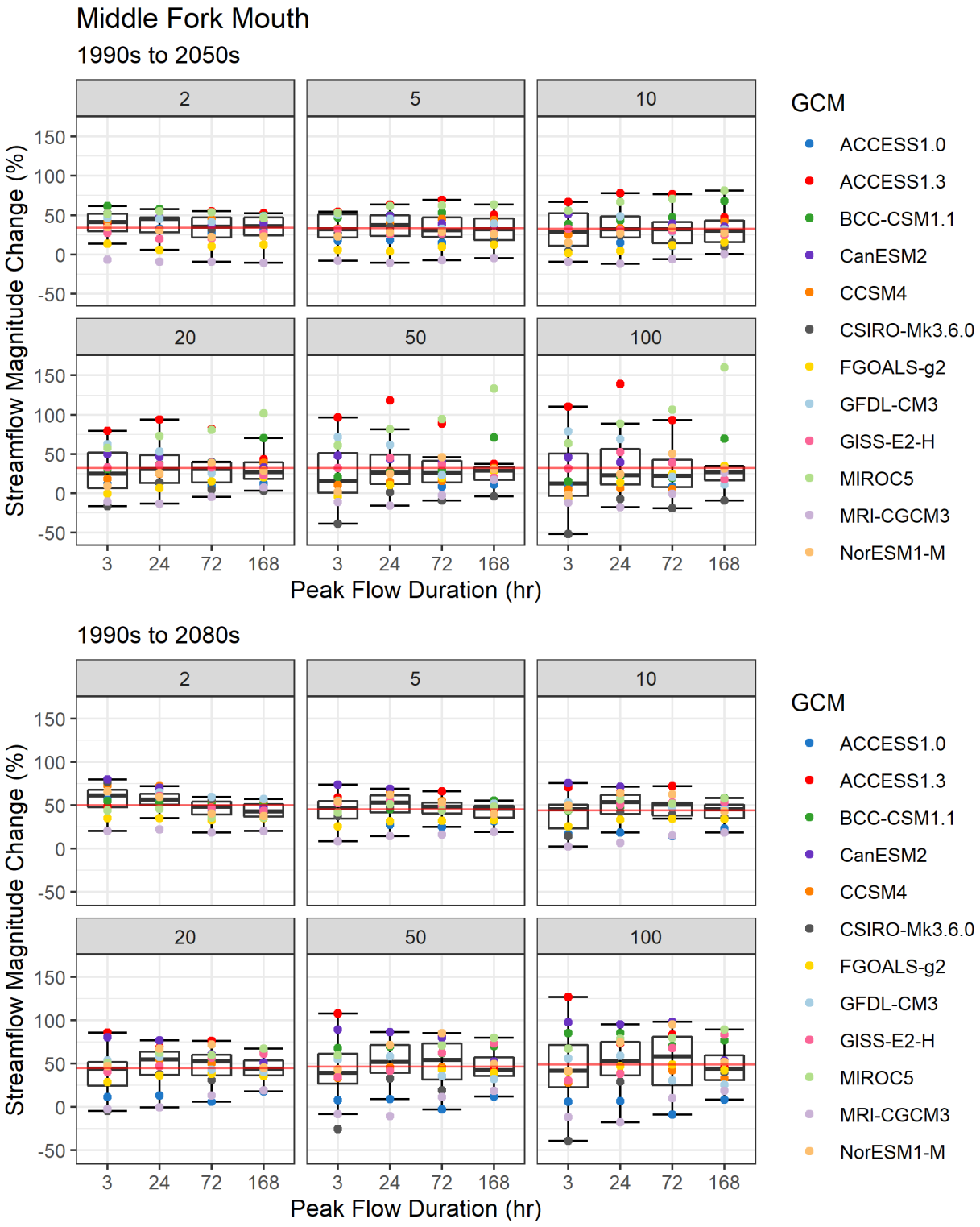

Figure 32: Peak flow magnitude change from the 1990s to 2050s (top) and 1990s to 2080s (bottom) for select return periods (2, 5, 10, 20, 50, and 100-year) at the mouth of the Middle Fork Nooksack River. The solid red line is the average magnitude change for each return period across all GCMs and flow durations.

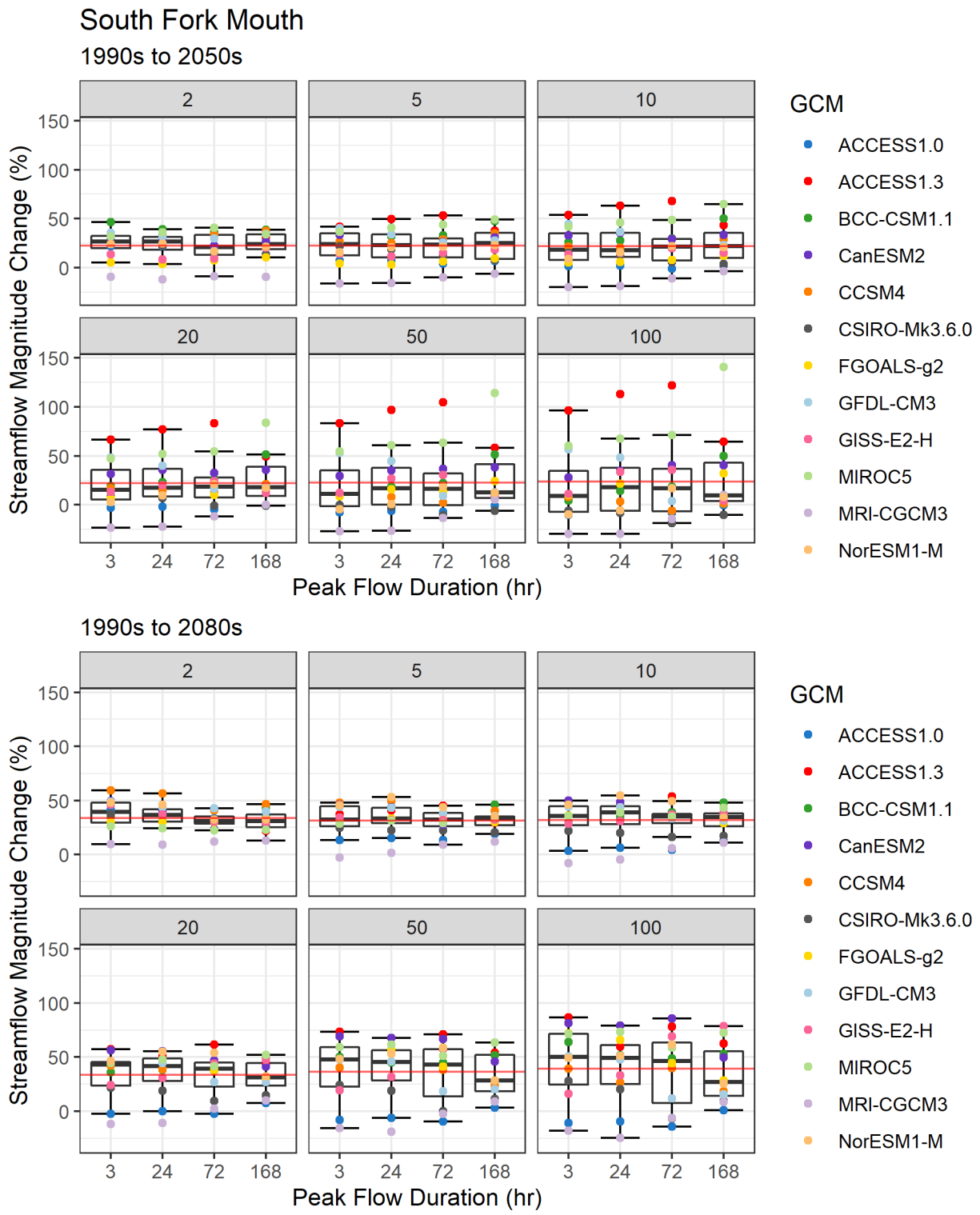

Figure 33: Peak flow magnitude change from the 1990s to 2050s (top) and 1990s to 2080s (bottom) for select return periods (2, 5, 10, 20, 50, and 100-year) at the mouth of the South Fork Nooksack River. The solid red line is the average magnitude change for each return period across all GCMs and flow durations.

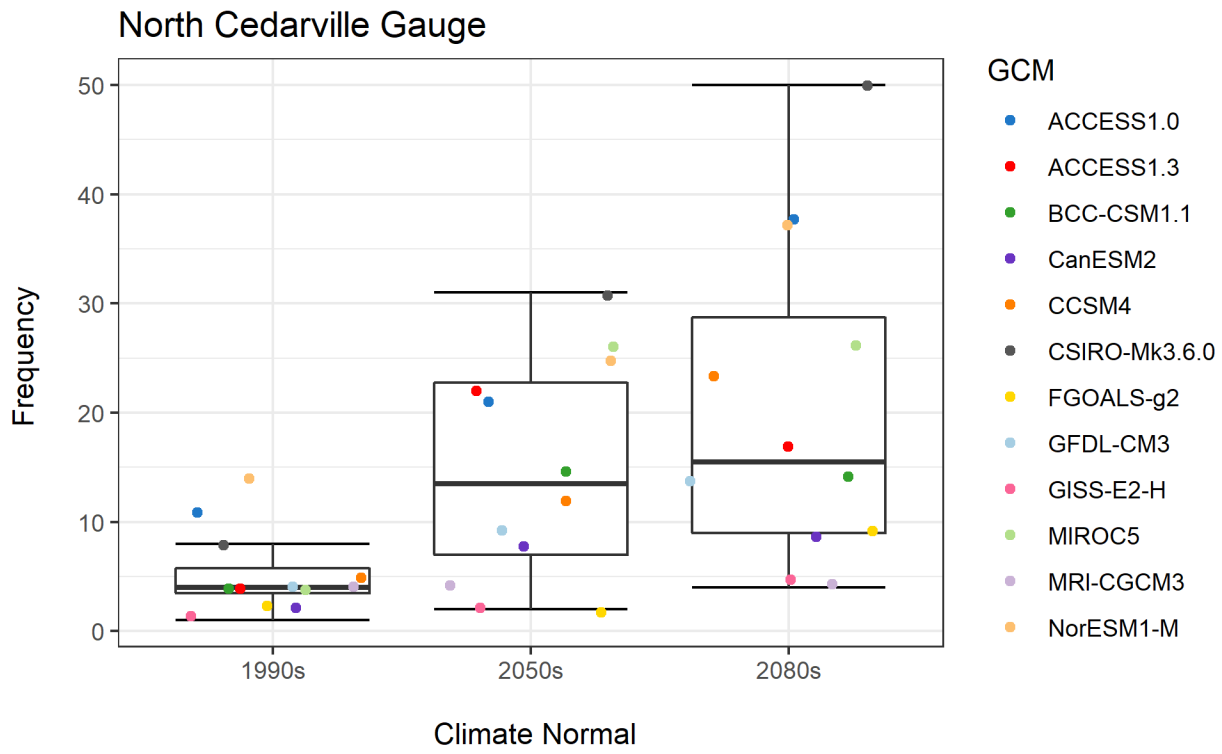

Figure 34: The number of exceedances in a 30-year time span of a historical 24-hour, 10-year peak flow event (discharge = 1,202 cms) at the North Cedarville gauge for the 1990s, 2050s, and 2080s normals.

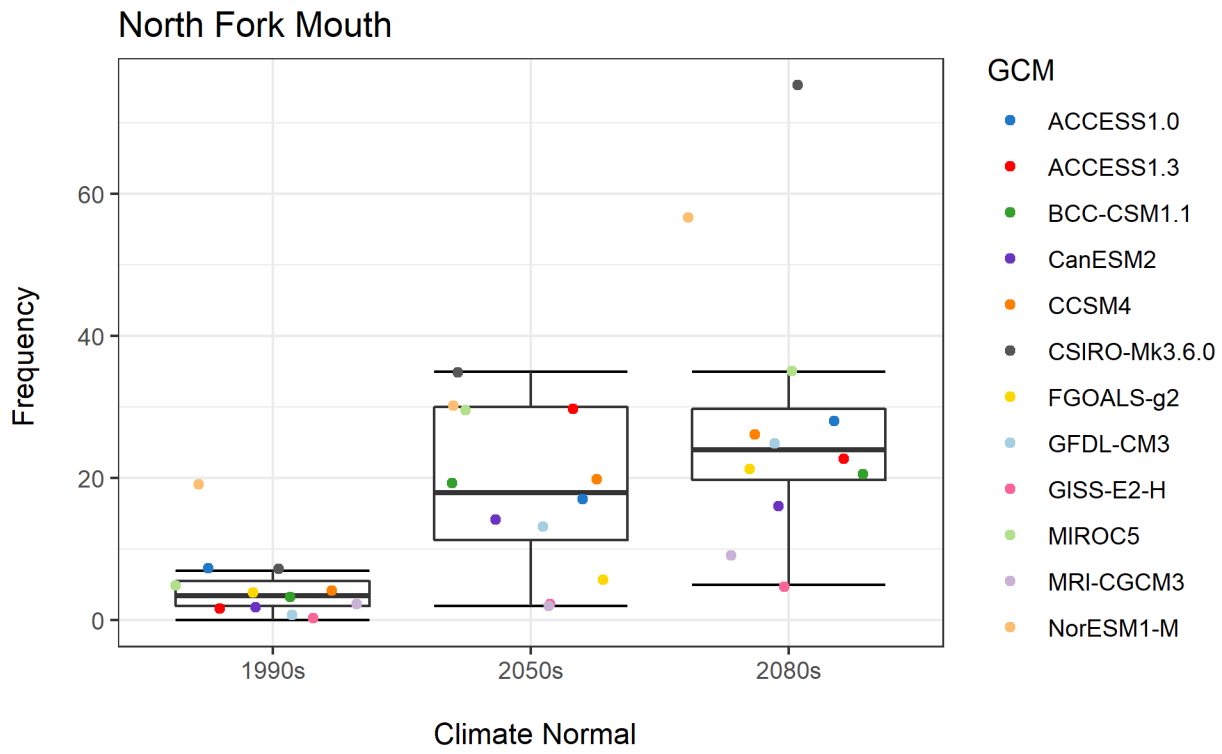

Figure 35: The number of exceedances in a 30-year time span of a historical 24-hour, 10-year peak flow event (discharge = 562 cms) at the North Fork mouth for the 1990s, 2050s, and 2080s normals.

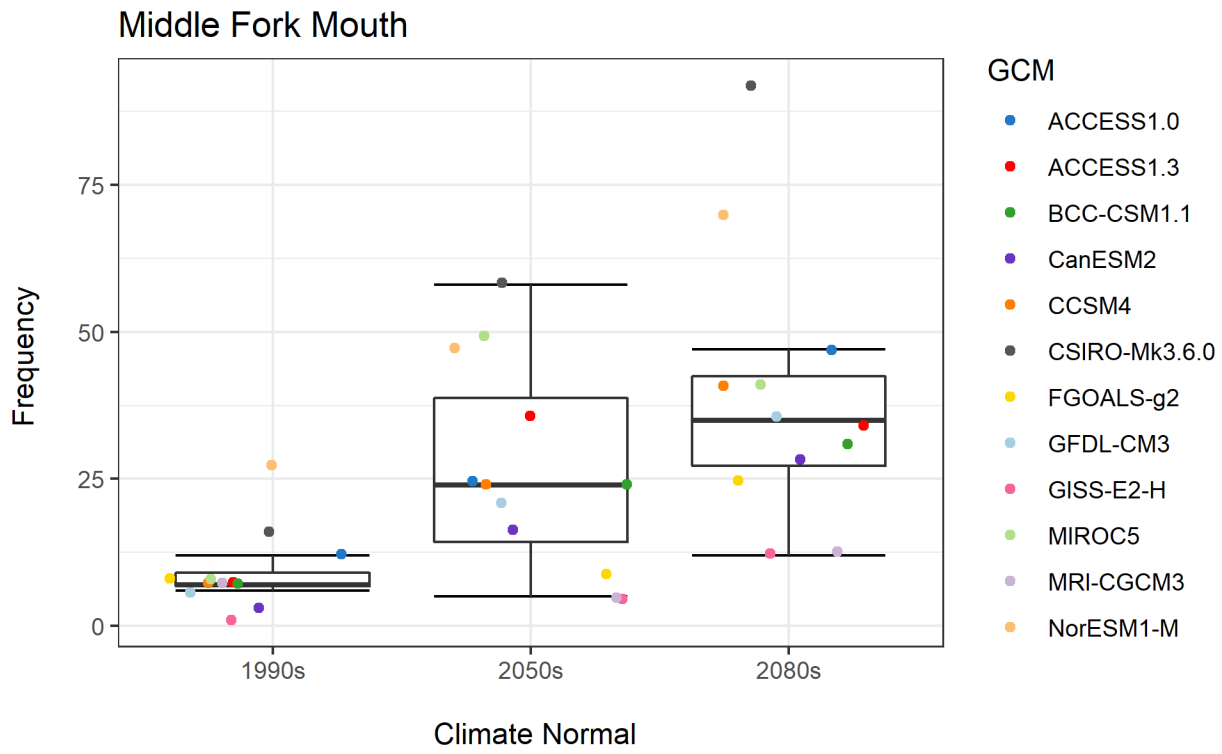

Figure 36: The number of exceedances in a 30-year time span of a historical 24-hour, 10-year peak flow event (discharge = 231 cms) at the Middle Fork mouth for the 1990s, 2050s, and 2080s normals.

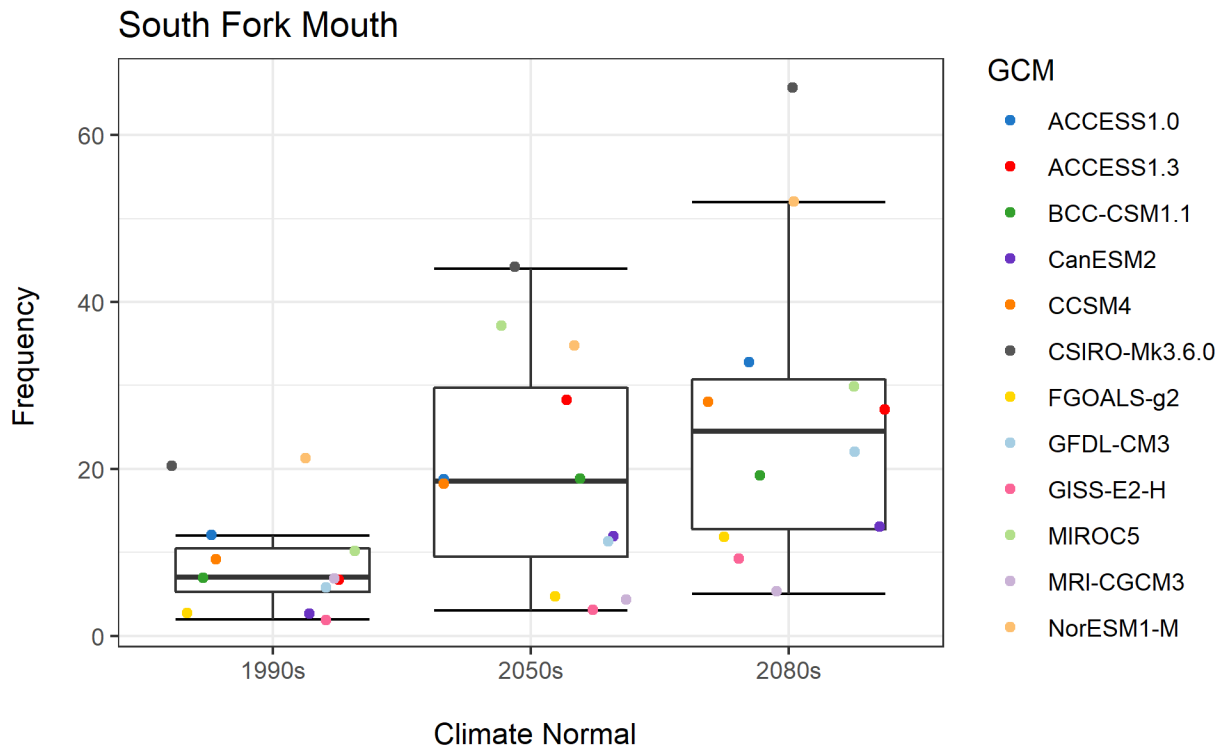

Figure 37: The number of exceedances in a 30-year time span of a historical 24-hour, 10-year peak flow event (discharge = 432 cms) at the South Fork mouth for the 1990s, 2050s, and 2080s normals.

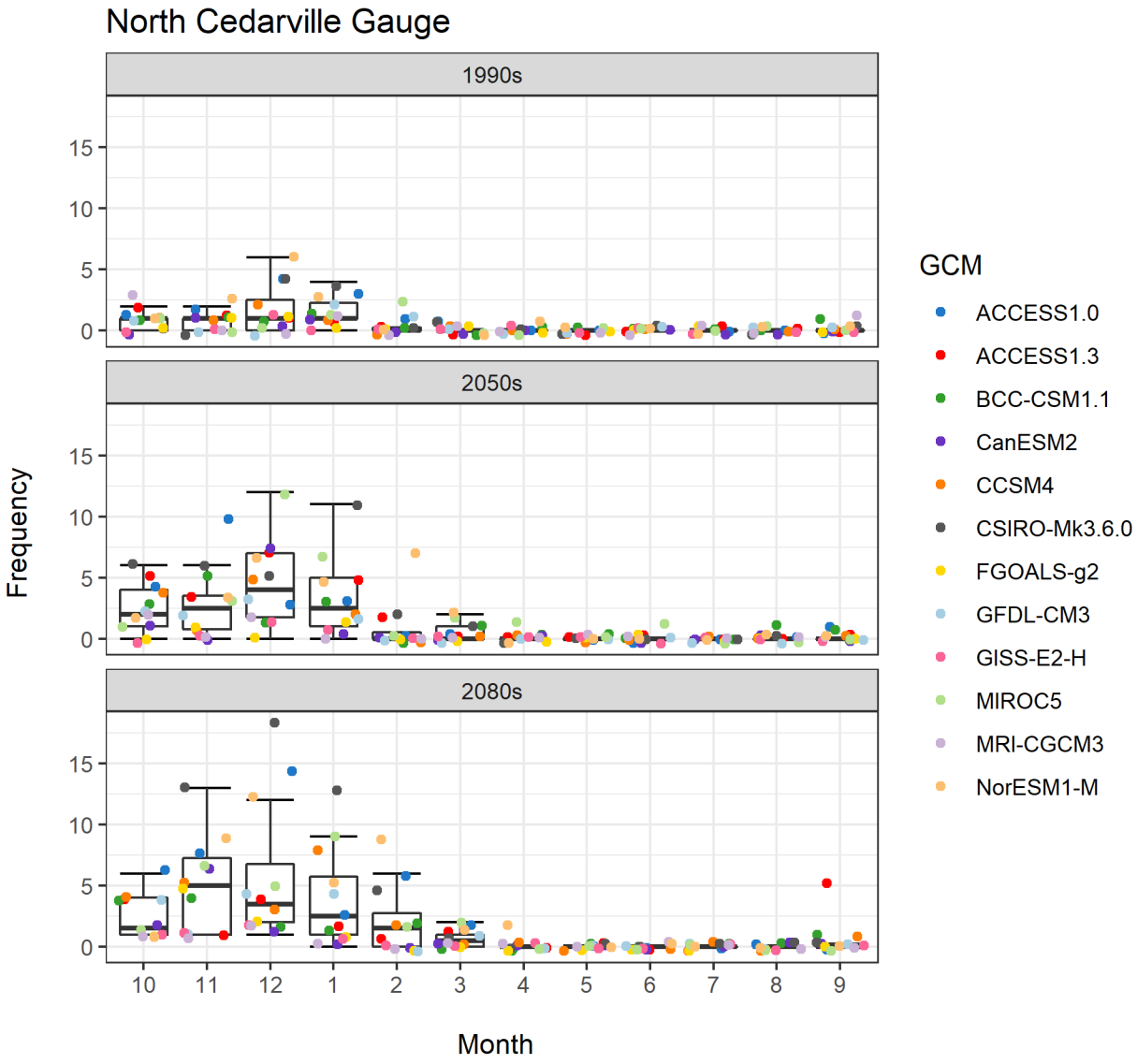

Figure 38: The number of exceedances per month in a 30-year time span of a historical 24-hour, 10-year peak flow event (discharge = 1,202 cms) at the North Cedarville gauge for the 1990s, 2050s, and 2080s normals.

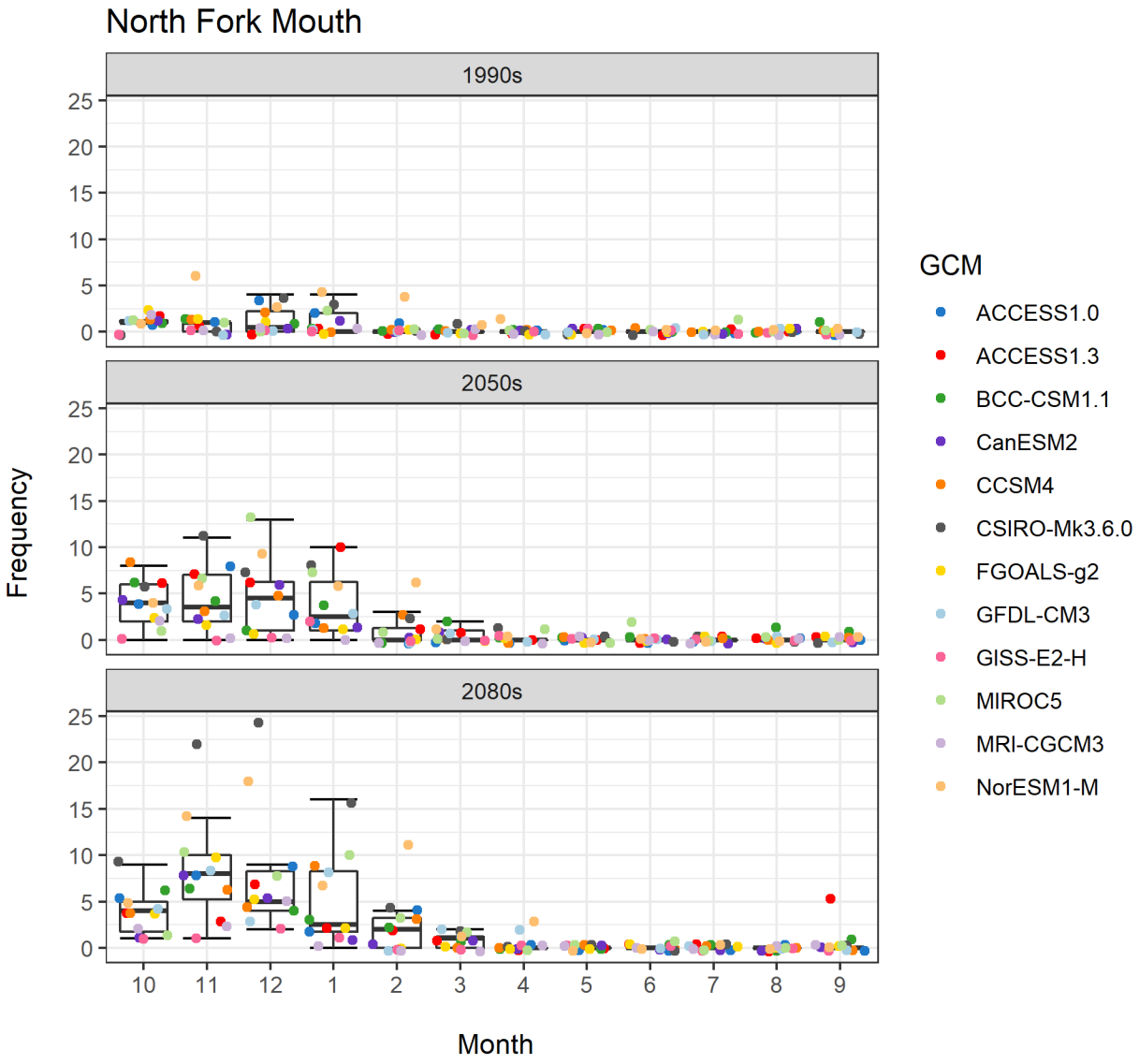

Figure 39: The number of exceedances per month in a 30-year time span of a historical 24-hour, 10-year peak flow event (discharge = 562 cms) at the North Fork mouth for the 1990s, 2050s, and 2080s normals.

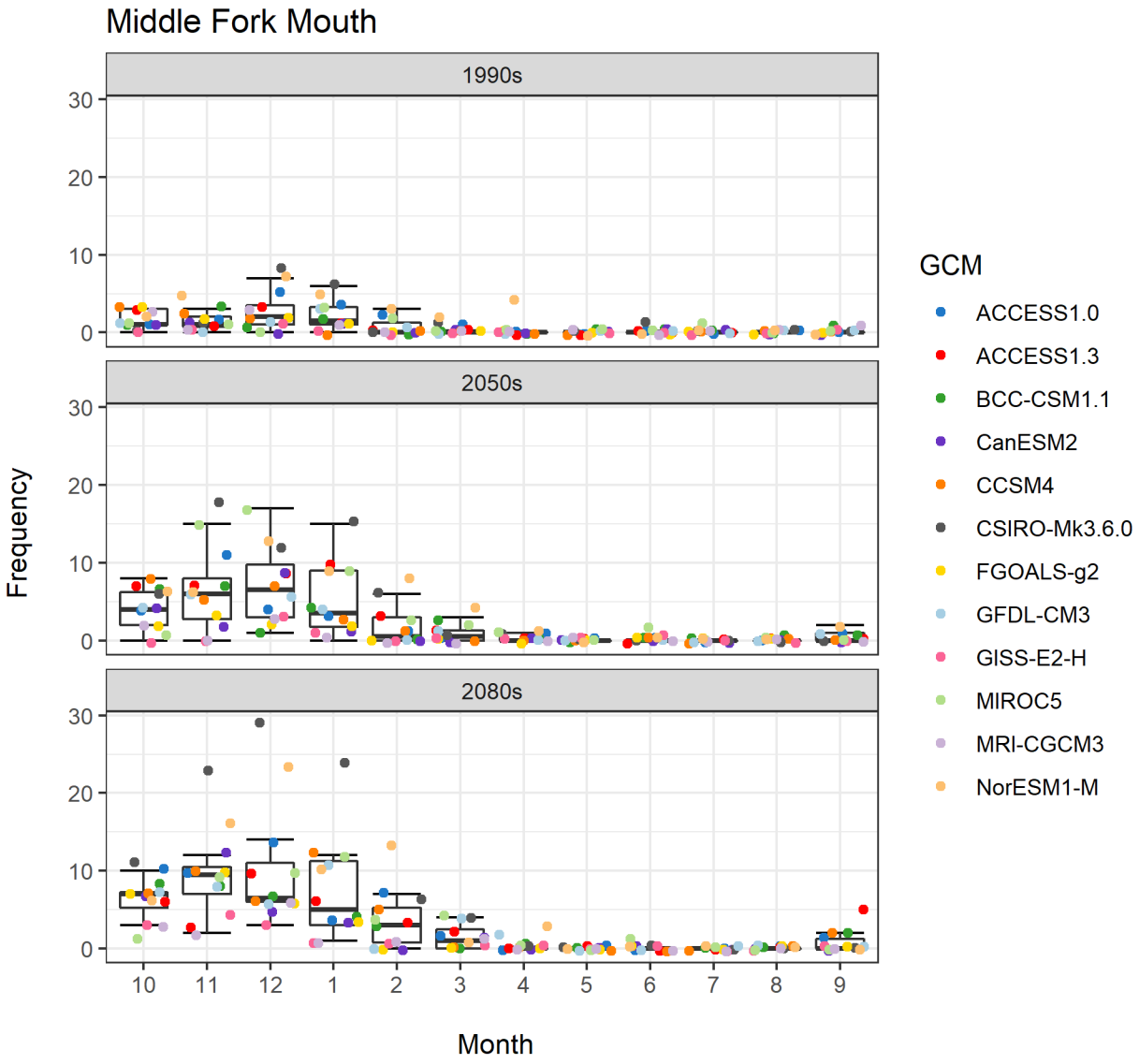

Figure 40: The number of exceedances per month in a 30-year time span of a historical 24-hour, 10-year peak flow event (discharge = 231 cms) at the Middle Fork mouth for the 1990s, 2050s, and 2080s normals.

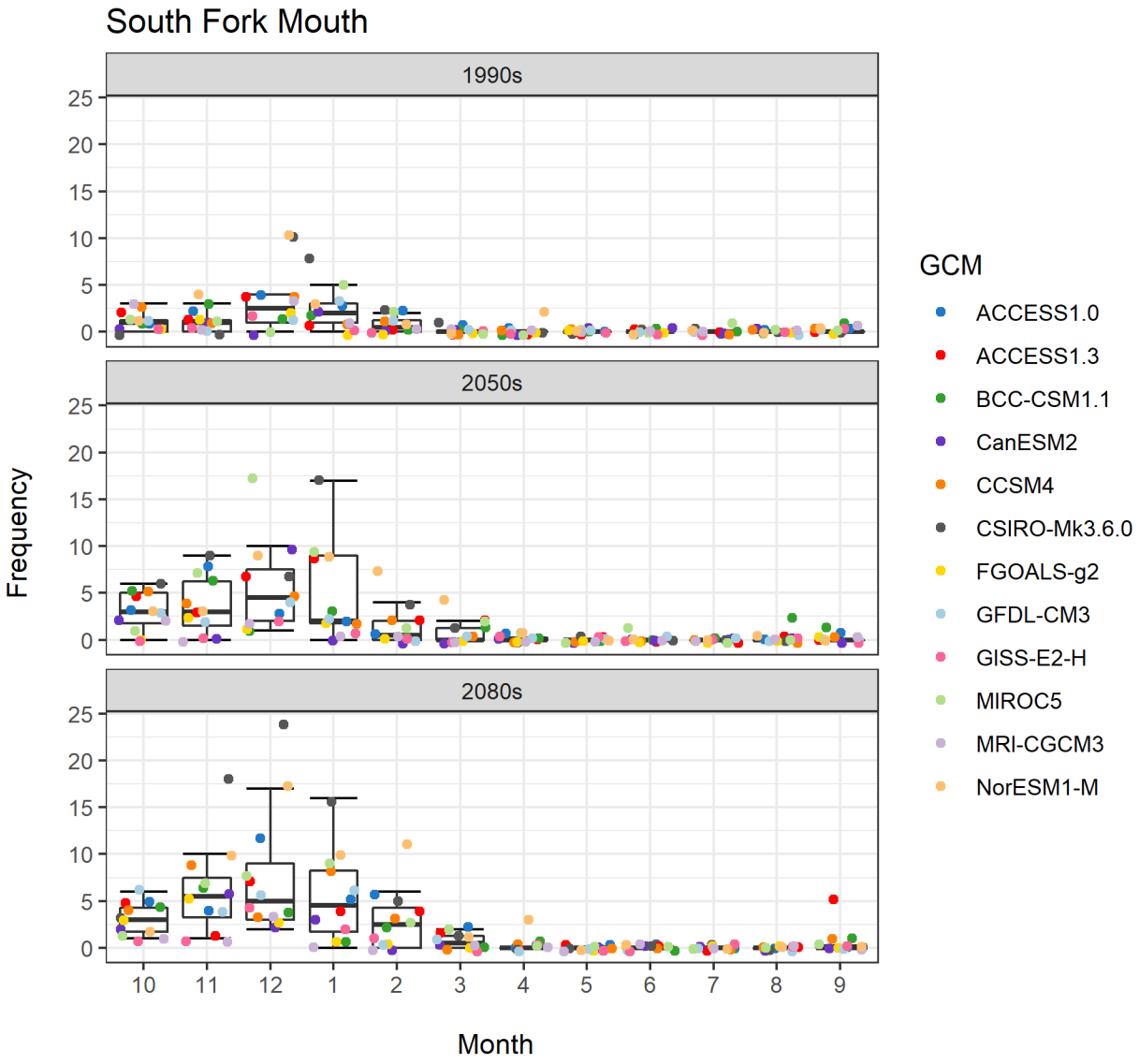

Figure 41: The number of exceedances per month in a 30-year time span of a historical 24-hour, 10-year peak flow event (discharge = 432 cms) at the South Fork mouth for the 1990s, 2050s, and 2080s normals.

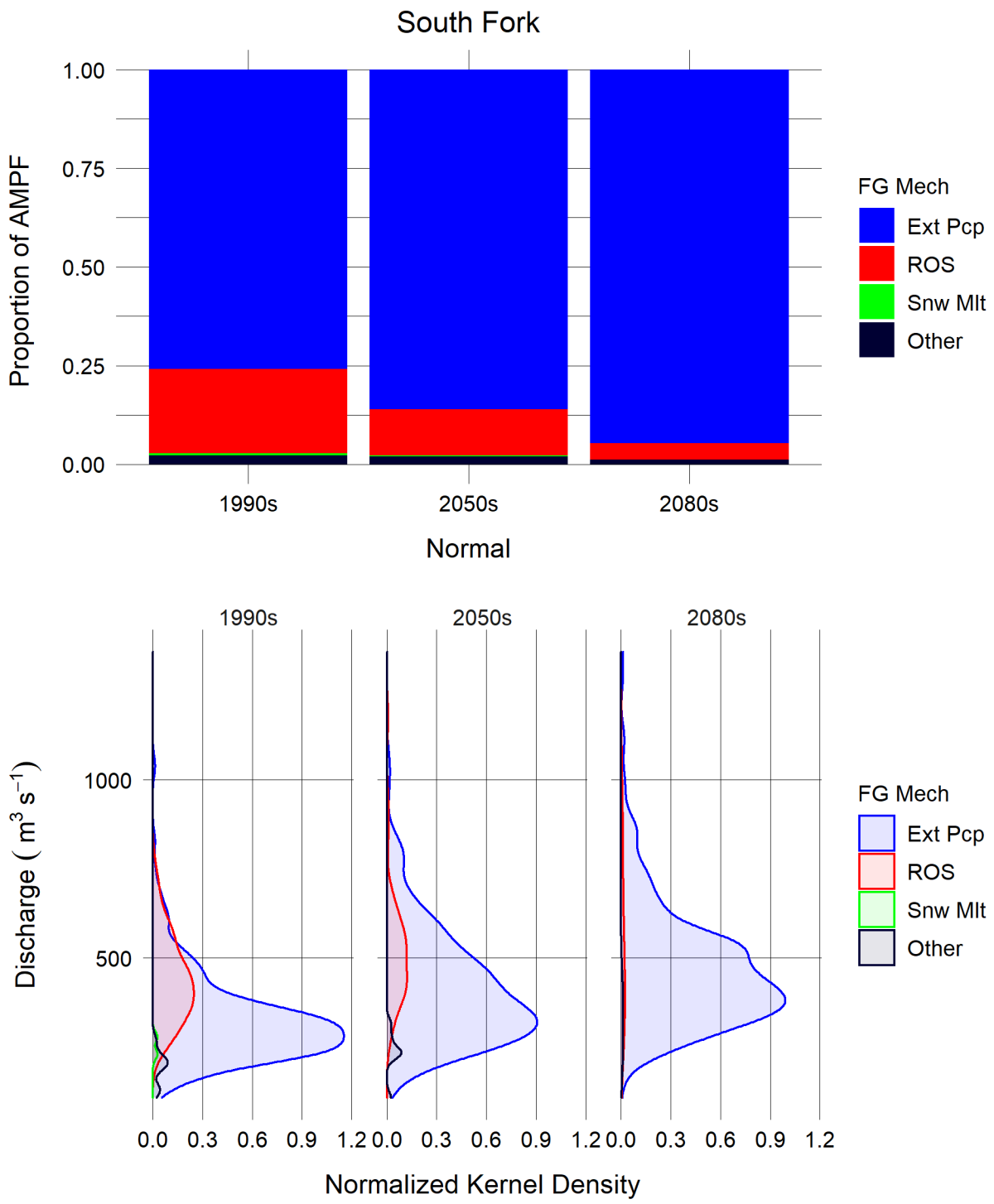

Figure 42: (Top) The proportion of 24-hour duration annual max peak flows (AMPF) in the South Fork for the 1990s, 2050s, 2080s normals generated by either extreme precipitation, rain-on-snow events, snowmelt, or other. (Bottom) The frequency of discharge magnitudes associated with each peak flow generating mechanism (FG Mech) for each normal.

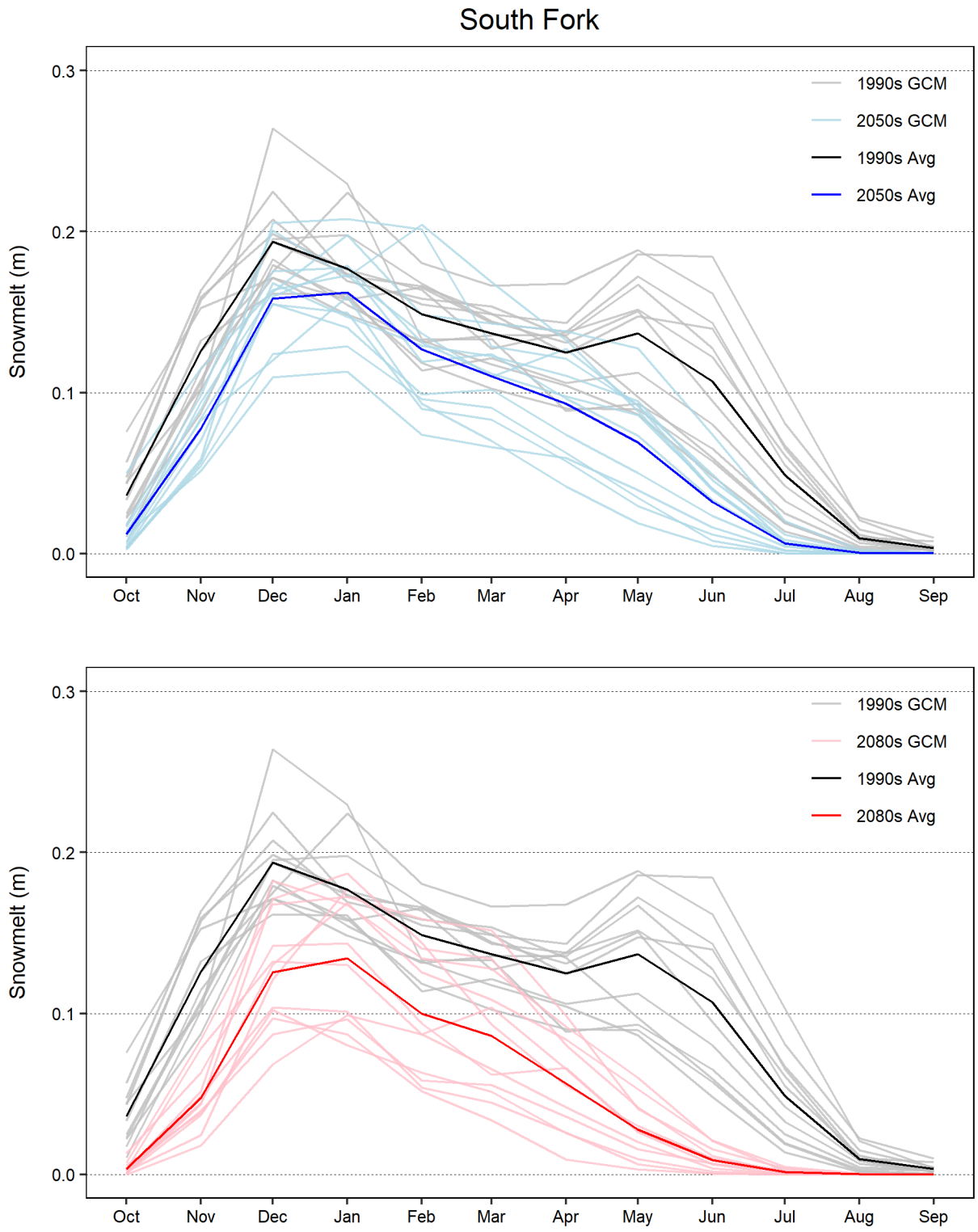

Figure 43: Simulated monthly snowmelt in the South Fork subbasin for the 2050s (top) and 2080s (bottom) 30-year normals. Gray, light blue, and light red lines represent 30-year averages for individual GCMs. Black, blue, and red lines represent the ensemble average across all 12 GCMs.

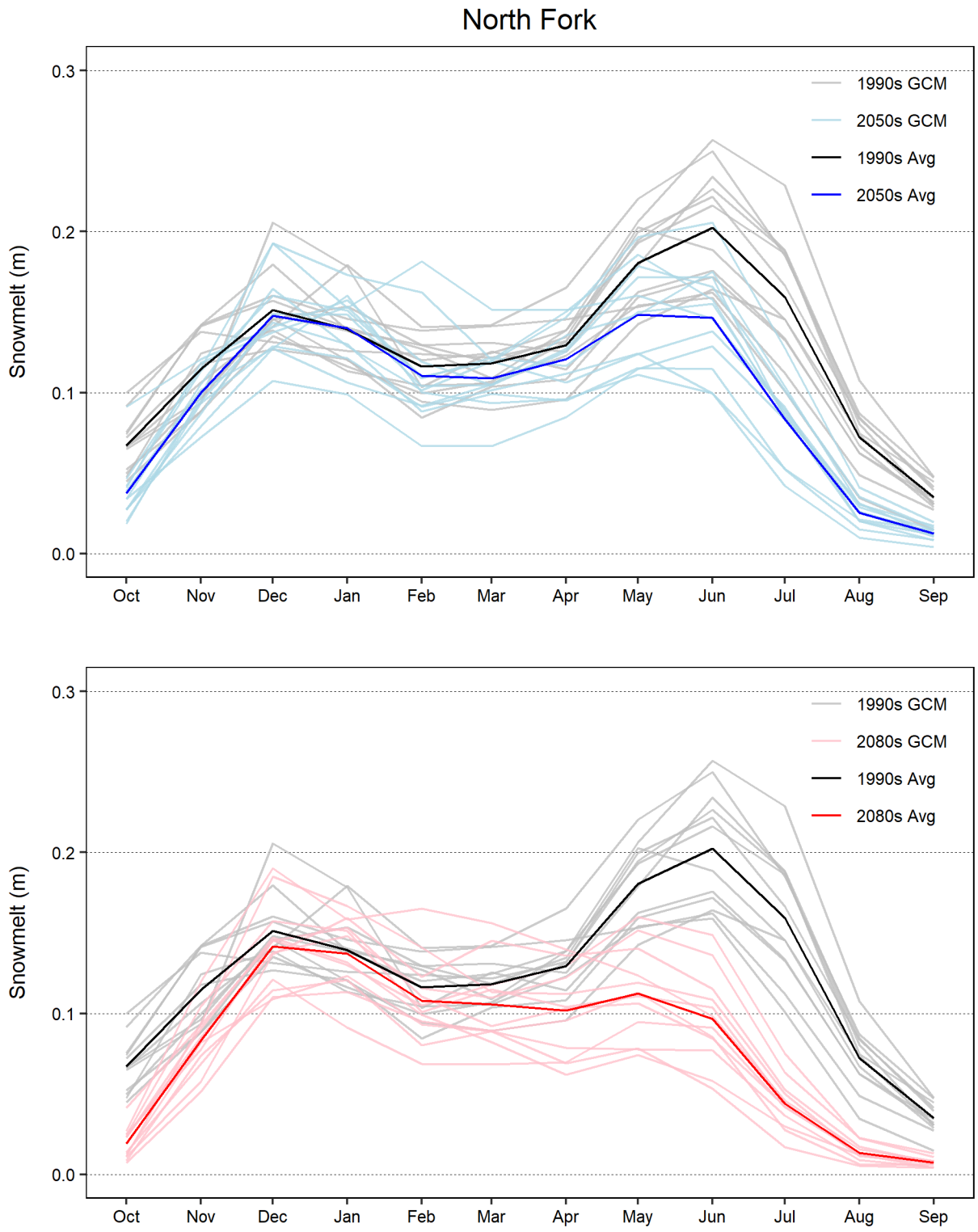

Figure 44: Simulated monthly snowmelt in the North Fork subbasin for the 2050s (top) and 2080s (bottom) 30-year normals. Gray, light blue, and light red lines represent 30-year averages for individual GCMs. Black, blue, and red lines represent the ensemble average across all 12 GCMs.

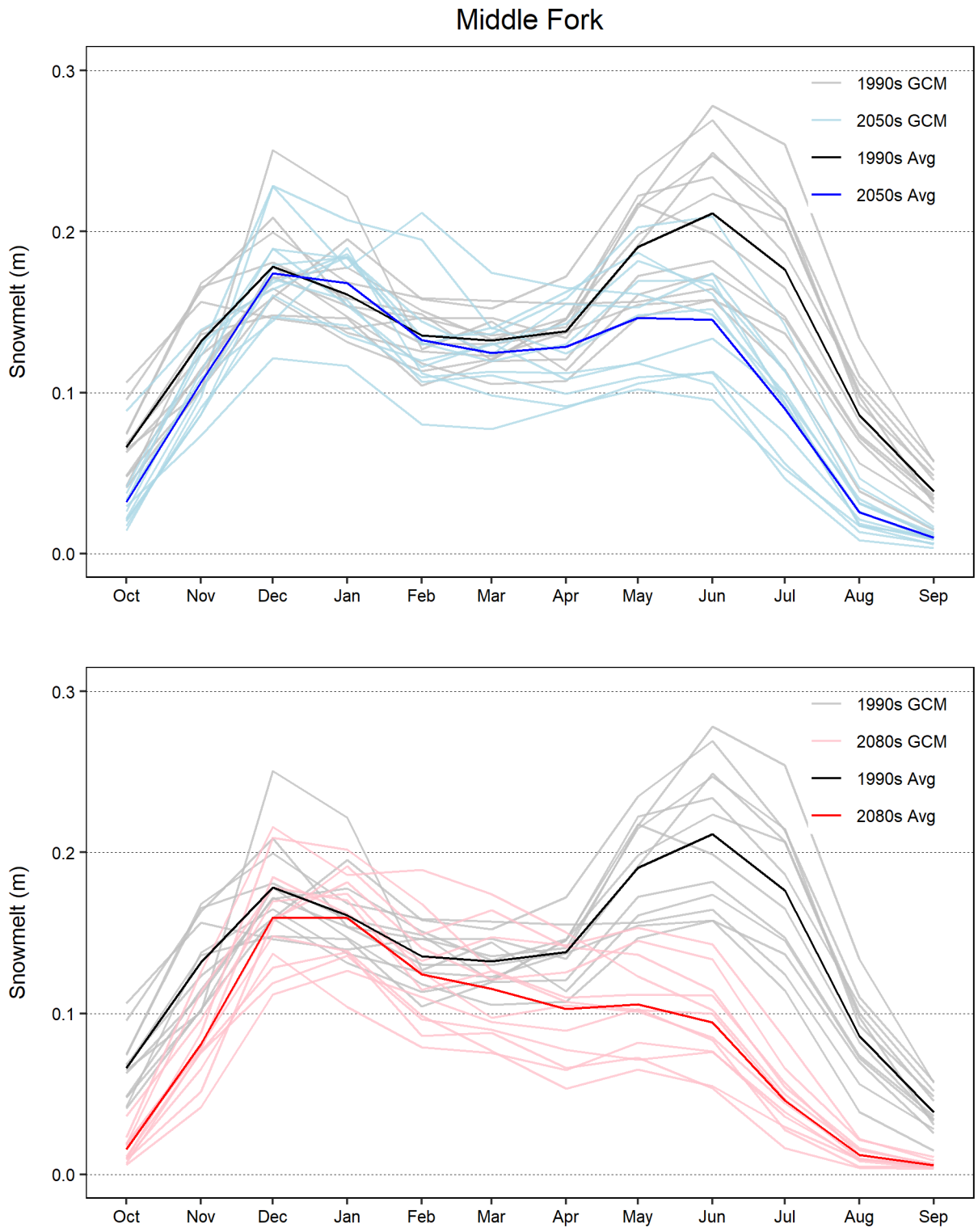

Figure 45: Simulated monthly snowmelt in the Middle Fork subbasin for the 2050s (top) and 2080s (bottom) 30-year normals. Gray, light blue, and light red lines represent 30-year averages for individual GCMs. Black, blue, and red lines represent the ensemble average across all 12 GCMs.